Journal of Alloys and Compounds

Extremely uniform nanosized oxide particles dispersion strengthened tungsten alloy with high tensile and compressive strengths fabricated involving liquid-liquid method

--Manuscript Draft--

Manuscript Number:	JALCOM-D-20-14911R2
Article Type:	Full Length Article
Keywords:	Tungsten heavy alloys; oxide particle strengthening; Zirconia; liquid-liquid doping; compressive strength; Hot isostatic pressing
Corresponding Author:	fangnao xiao Univ. Bourgogne Franche-Comté, FEMTO-ST Institute Besançon, FRANCE
First Author:	fangnao xiao
Order of Authors:	fangnao xiao
	Thierry Barriere
	Gang Cheng
	Qiang Miao
	Shiwei Zuo
	Shizhong Wei
	Liujie Xu
Abstract:	In this study, tungsten heavy alloys reinforced with highly uniform and dispersed nanosized Zr(Y)O2 particles were investigated. These alloys exhibited a high compressive strength and enhanced plasticity. To fabricate these alloys, we used a novel process involving molecular level liquid-liquid doping combined with hot isostatic pressing. The Zr(Y)O2 particles thus produced were smaller than 200 nm in size and bonded well with tungsten grains. The size of Zr(Y)O2 particles and tungsten grains are much smaller than those of the state-of-the-art review and the details of the grain refinement mechanisms were discussed. The effect of Zr(Y)O2 particles and strain rate on the compressive properties of the alloys was investigated in detail and the corresponding compressive deformation mechanisms were elucidated. The highest ultimate tensile and compressive strengths of the fabricated alloys at room temperature (27°C) were 906 and 1445 MPa, respectively, which are higher than most of reported values in the literature. The ultimate tensile strength and fracture strain of WHAs decrease with the mass fraction of Zr(Y)O2 (from 0 to 0.75%). The alloys exhibit the brittle material behaviour in tension, compared to the pure tungsten with ductile material behaviour. The tensile fracture surface consists of W - W cleavage patterns and ductile failure of the matrix. The results obtained in this research will act as basic guidelines for the fabrication of ODS-W alloys by liquid-liquid doping process.
Order of Authors (with Contributor Roles):	fangnao xiao
	Thierry Barriere
	Gang Cheng
	Qiang Miao
	Shiwei Zuo
	Shizhong Wei
	Liujie Xu

Apr. 27, 2021

To

Prof. Ludwig Schultz

Editor: Journal of Alloys and Compounds

Cover letter

Dear Sir,

I am pleased to submit the revised version of our research article entitled "Extremely uniform nanosized oxide particles dispersion strengthened tungsten alloy with high tensile and compressive strengths fabricated involving liquid-liquid method" for publication in Journal of Alloys and Compounds. The reviewers' comments are addressed in the present draft and the responses to these comments are appended herewith for your reference.

We believe that the improved version of the manuscript is now appropriate for publication.

This manuscript has not been published nor under consideration for publication elsewhere. We have no conflicts of interest to disclose.

Thank you for your consideration.

Response to Editor and Reviewer Comments:

No.: JALCOM-D-20-14911R1

Title: Extremely uniform nanosized oxide particles dispersion strengthened tungsten alloy with high tensile and compressive strengths fabricated involving liquid-liquid method

We sincerely thank you and the reviewer for your insightful comments; they have proven very useful in enhancing the quality of our manuscript. We have addressed the issue indicated in the review reports. The changes made to the manuscript are highlighted in red.

Reviewer #2: The authors have tried to address all questions raised by the two reviewers in their response, and the manuscript has been improved. My comments have been addressed mostly, but I still think it is necessary for the authors to present the tensile engineering stress-strain curves. We do not know how the authors obtain the ultimate tensile strength of the alloys in Fig. 11a. And I think the authors' reason that "the paper is already too long" is insufficient. Furthermore, if the ductility is not mentioned, the significance of the article is questionable.

Response: Thank you for your suggestions. The tensile engineering stress-strain curves of the WHA alloys with different mass fraction of $Zr(Y)O_2$ were added in revised paper (Fig. 11a). The UTS of the associated alloy and pure tungsten were modified and compared with the state of art.

The mechanical behaviour in tension (ductile and brittle) of the materials was discussed in the manuscript. The mechanical behaviour for different alloys under various solicitations was underlined in abstract and conclusion.

Extremely uniform nanosized oxide particles dispersion strengthened tungsten alloy with high tensile and compressive strengths fabricated involving liquid-liquid method

Fangnao Xiao [a]*, Thierry Barriere [a], Gang Cheng [b], Qiang Miao [c], Shiwei Zuo [c]

[a] Université Bourgogne Franche-Comté, FEMTO-ST Institute, CNRS/UFC/ENSMM/UTBM, Department of Applied Mechanics, 25000 Besançon, France

[b] INSA CVL, Université Tours, Université Orléans, LaMé, 3 rue de la Chocolaterie, CS 23410, 41034 Blois Cedex, France

[c] College of Material Science and Technology, Nanjing University of Aeronautics and Astronautics, 29 Yudao Street, Nanjing 210000, China

*Corresponding author

E-mail: fangnao.xiao@femto-st.fr

Full postal address:

FEMTO-ST Institute, Department of Applied Mechanics, 24 chemin de l'épitaphe, 25000, Besançon, France

Tel.: +33381666000

Abstract

In this study, tungsten heavy alloys reinforced with highly uniform and dispersed nanosized $Zr(Y)O_2$ particles were investigated. These alloys exhibited a high compressive strength and enhanced plasticity. To fabricate these alloys, we used a novel process involving molecular level liquid-liquid doping combined with hot isostatic pressing. The $Zr(Y)O_2$ particles thus produced were smaller than 200 nm in size and bonded well with tungsten grains. The size of $Zr(Y)O_2$ particles and tungsten grains are much smaller than those of the state-of-the-art review and the details of the grain refinement mechanisms were discussed. The highest ultimate tensile and compressive strengths of the fabricated alloys at room temperature (27°C) were 895 and 1445 MPa, respectively, which are much higher than the values reported in the literature. The tensile fracture surface consists of W - W cleavage patterns and ductile failure of the matrix. The effect of $Zr(Y)O_2$ particles and strain rate on the compressive properties of the alloys was investigated in detail and the corresponding compressive deformation mechanisms were elucidated.

Keywords: Tungsten heavy alloys; oxide particle strengthening; zirconia; liquid-liquid doping; compressive strength; hot isostatic pressing

Nomenclature

α-HATB	Hexagonal ammonium tungsten bronze $(NH_4)_{0.33}\cdot WO_3$
β-HATB	Hexagonal ammonium tungsten bronze $(NH_4)_{0.42}\cdot WO_3$
AMT	Ammonium metatungstate
APT	Ammonium paratungstate
DUAs	Depleted uranium alloys
EDS	Energy dispersive X-ray spectroscopy
HATB	Hexagonal ammonium tungsten bronze, $(NH_4)_x\cdot WO_3$
HIP	Hot isostatic pressing
HR-TEM	High-resolution transmission electron microscopy
HV	Vickers hardness

L-L	Liquid-liquid
L-S	Liquid-solid
MA	Mechanical alloying
ODS-W	Oxide particle dispersion-strengthened tungsten
ODS-WHAs	Oxide particle dispersion-strengthened tungsten heavy alloys
PSZ	Partially stabilised zirconia
RD	Relative densities
SAED	Selected area electron diffraction
SEM	Scanning electron microscopy
SPS	Spark plasma sintering
S-S	Solid-solid
UTS	Ultimate tensile strength
VD	Sintering process in the vertical direction
WHAs	Tungsten heavy alloys
WHA-Zr(Y)O_2	Zr(Y)O_2 particle dispersion-strengthened 93W-4.9Ni-2.1Fe alloy
W-M	Tungsten-matrix
W-W	Tungsten-tungsten
XRD	X-ray diffraction

1. Introduction

Tungsten heavy alloys (WHAs) are promising materials for kinetic energy penetrators, radiation shields, and rocket nozzles, owing to their moderate ductility, high density, and quasi-static strength [1-4]. In particular, WHAs are more suitable for use in kinetic energy penetrators than depleted uranium alloys (DUAs) as they pose no risk of radioactive contamination [5]. Furthermore, they exhibit a lower penetration performance (by ~20%) than DUAs at high strain rates [6,7].

Generally, the penetration capability of WHAs depends on their strength and toughness [8]. The existing WHAs obtained using conventional powder metallurgy are limited to anti-armour penetrators owing to the weak mechanical properties of coarse tungsten grains [9]. In recent years, a large number of researchers have focused on improving the mechanical performance of WHA penetrators by inducing microstructural changes [10-12] via changing the WHA composition by adding alloying elements or rare earth oxides (Y_2O_3, La_2O_3, ZrO_2, ThO_2, and CeO_2) [13-16] or by microstructural refinement [17-20].

Grain refinement in tungsten is known to significantly enhance its mechanical properties. However, the grain size of WHAs depends partially on the particle size of the initial powders. In the past few years, liquid-liquid (L-L) doping techniques have been developed for oxide particle-doped tungsten powders. Xu et al. fabricated La_2O_3-doped ultra-fine tungsten powders using $Na_2WO_4{\cdot}2H_2O$ and $La(NO_3)_3{\cdot}6H_2O$ as the raw materials [21]. Nanosized La_2O_3-doped tungsten powders with a particle size of ~700 nm were realised by hydrogen reduction. Dong et al. synthesised Y_2O_3-doped nanosized tungsten powders with an average particle size of 40–50 nm via a wet-chemical process [22]. Xiao et al. used the hydrothermal method coupled with hydrogen reduction to develop nanocrystal powders of W-Zr(Y)O_2 with an average particle size of 30 nm [23]; these oxides were used as nucleation cores in tungsten for particle refinement. Rare earth elements (such as Y, Zr and La) decrease the number of O and P impurities aggregating at the interface and thus improve the performance of WHA penetrators [24]. In addition, nanosized oxide particles can lead to dispersion strengthening and grain refinement, thus increasing the strength and

ductility of the alloys fabricated by L-L doping [25,26]. Therefore, L-L doping with nanosized oxide particles is considered to be an effective approach for improving the mechanical performance of WHAs.

In this study, a novel material based on dispersion-strengthened 93W-4.9Ni-2.1Fe alloys [WHA-Zr(Y)O_2] using nanosized Zr(Y)O_2 is proposed. WHA-Zr(Y)O_2 was prepared by a hydrothermal method combined with mechanical alloying. Nanosized Zr(Y)O_2 dispersion-strengthened WHAs were fabricated by conventional solid-phase sintering and hot isostatic pressing (HIP). The uniaxial tensile and compressive properties of WHA-Zr(Y)O_2 were estimated and the effect of Zr(Y)O_2 on the microstructure and mechanical properties of the WHAs were investigated. These microstructural characteristics and mechanical properties of the present WHA-Zr(Y)O_2 alloys were compared with those of the state-of-the-art WHA materials to demonstrate the effectiveness of the proposed method. It indicates that the fabricated alloys exhibit more smaller size of tungsten grains and oxide particles, and higher ultimate tensile and compressive strengths.

This article is structured as follows. In Section 2, the sample preparation and characterisation processes are described in detail. In Section 3, our observations on powder morphology, WHA microstructure, and the mechanical properties of WHA-Zr(Y)O_2 alloys are described with reference to the relevant literature. Finally, our major conclusions are presented in Section 4.

2. Experimental procedure

2.1 Sample preparation

In the present work, four W-Zr(Y)O_2 powders were prepared using the process shown in Fig. 1. The composition of the alloy powders contained varying amounts of Zr(Y)O_2 (0, 0.25, 0.5, and 0.75 wt.% denoted as WHA_0, $WHA_{0.25}$, $WHA_{0.50}$ and $WHA_{0.75}$, respectively, as listed in Table 1). The commercial raw materials included zirconium oxychloride octahydrate ($ZrOCl_2 \cdot 8H_2O$; grade AR), yttrium nitrate [$Y(NO_3)_3 \cdot 6H_2O$; grade AR] and ammonium metatungstate [$(NH_4)_6H_2W_{12}O_{40} \cdot 5H_2O$; grade AR; AMT]. The supplier of $ZrOCl_2 \cdot 8H_2O$ and $Y(NO_3)_3 \cdot 6H_2O$ powders was

Shanghai Diyang Industrial Co., LTD. The AMT powder was provided by Wuhan Kabuda Chemical Co., LTD. The synthesis and reduction of W-Zr(Y)O_2 powders were carried out according to previously described protocols [27]. After hydrothermal treatment, the precursor consisted of hexagonal $(NH_4)_{0.33}\cdot WO_3\cdot$(α-hexagonal ammonium tungsten bronze, α-HATB, PDF# 42-0452), as shown in Fig. 2a). The reduction process included the following stages – a first reduction step at 500 °C for 1.5 h resulting in hexagonal $(NH_4)_{0.42}WO_3$ (β-HATB, PDF#42-0451), which is expected to produce high-quality doped tungsten powders and alloys [27], and a second reduction reaction at 800 °C for 2 h to yield W-Zr(Y)O_2 powder.

W-Zr(Y)O_2 alloys were fabricated by spark plasma sintering (SPS) at 2000 °C for 5 min at 30 MPa. Mechanical alloying (MA) was conducted to blend elemental Ni, Fe, and W-Zr(Y)O_2 powders at the appropriate proportions. A planetary ball mill was used at a milling speed of 250 rpm for 6 h. The milling media consisted of 3 mm diameter tungsten carbide balls with ball-to-powder ratio of 10:1. The milled powders were compacted into cylindrical rods by cold isostatic pressing at 250 MPa. Subsequently, the green compacts were sintered at 1250 °C for 1 h in a hydrogen atmosphere. These samples were later sintered by hot isostatic pressing at 1400 °C for 2 h at 180 MPa. Fig. 2b) shows the X-ray diffraction (XRD) pattern of $WHA_{0.75}$, which suggests the presence of W and γ(Fe, Ni) phases.

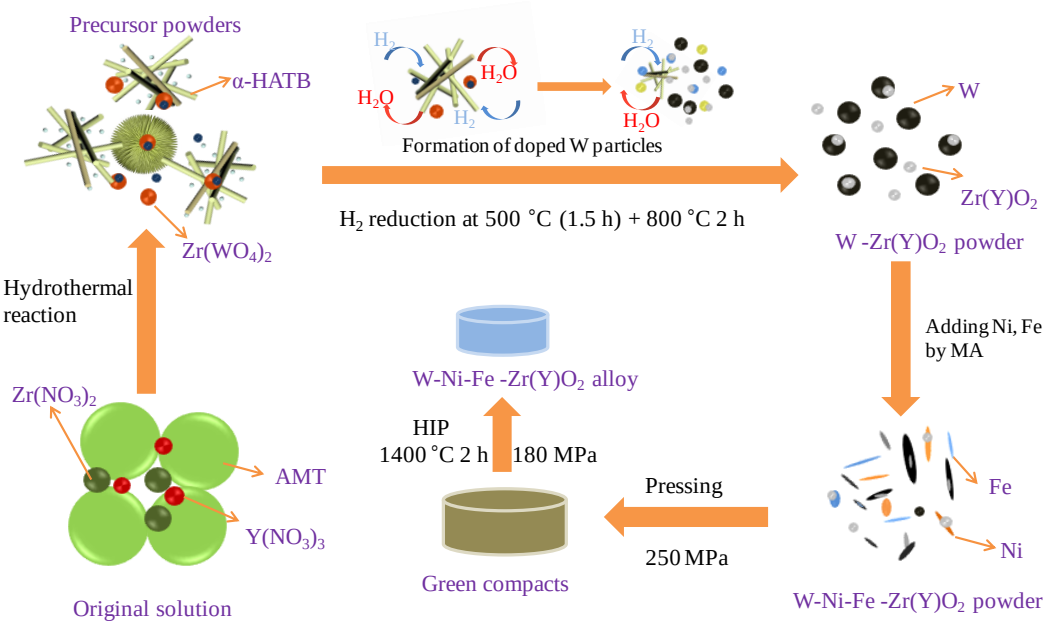

Fig. 1 Schematic diagram of the synthesis of WHAs

Table 1 Chemical composition of WHA-$Zr(Y)O_2$ alloys (wt.%)

Samples	W	Fe	Ni	ZrO_2	Y_2O_3
WHA_0	93.000	2.1	4.9	0.00	0.00
$WHA_{0.25}$	92.720	2.1	4.9	0.25	0.03
$WHA_{0.50}$	92.440	2.1	4.9	0.50	0.06
$WHA_{0.75}$	92.156	2.1	4.9	0.75	0.09

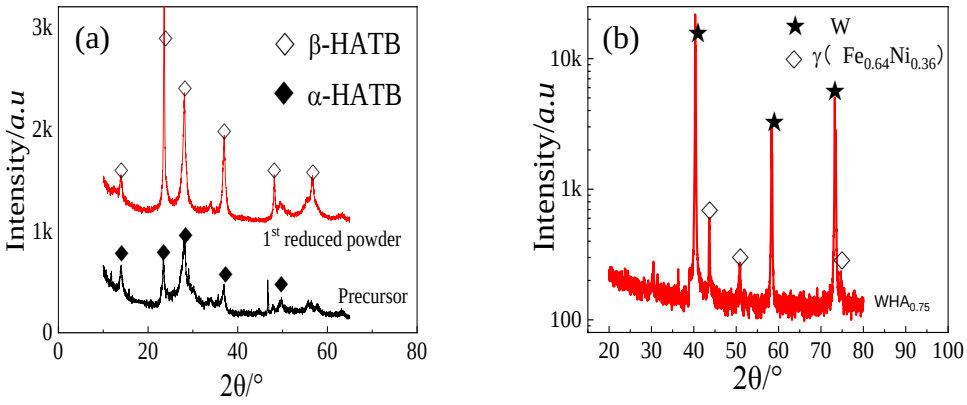

Fig. 2 XRD patterns of a) powder precursor and doped reduced powder and b) $WHA_{0.75}$

2.2 Measurement, experimental procedures, and analysis

The microstructure of the fabricated powders and alloys was evaluated by scanning electron microscopy (SEM), energy dispersive X-ray spectroscopy (EDS), and high-resolution transmission electron microscopy (HR-TEM). XRD analysis was conducted on the produced powders and alloys to identify their crystalline phases. The absolute densities of the alloys were determined using Archimedes' principle and theoretical densities were calculated based on the theoretical mass and volume. Relative density (RD) was calculated as the ratio of absolute and theoretical densities.

Vickers hardness (HV) testing was conducted with a 200 g indenting load and a dwell time of 20 s using the HVS-1000 digital micro Vickers hardness tester. The obtained value represented the average of values sourced from ten random positions on the alloy cross-section. Grain-size data was acquired using a line intercept method and at least 100 identifiable grains were considered for this measurement. Tungsten-tungsten (W-W) contiguity (C_{WW}), which is defined as the relative fraction of the W-W interfacial area, was estimated according to Eq. (1) [28],

$$C_{WW} = 2N_{WW}/(N_{WW} + N_{WM}) \quad (1)$$

where N_{WW} and N_{WM} indicate the number of W-W grain boundaries and tungsten-matrix (W-M) interfaces intercepted by an arbitrary straight line per unit length in the SEM images, respectively.

Tensile properties were measured on a universal testing machine (Instron-5967) at a constant loading rate of 0.3 mm/min at room temperature (27 °C). The average of three measured values is reported as the tensile strength of a given sample; specimen dimension is shown in Fig. 3.

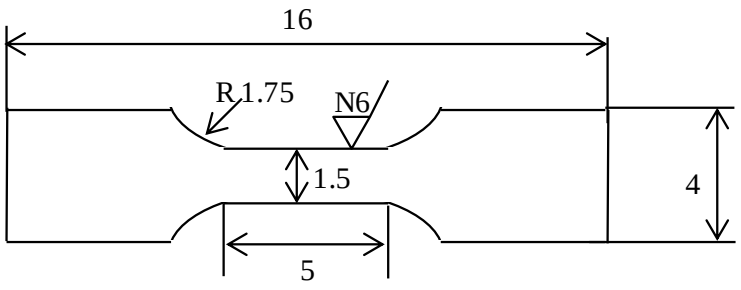

Fig. 3 Dimension of tensile testing specimens (all units are in mm)

The compressive properties of the samples were measured on a universal material machine (Shimadzu AG-I250kN) at strain rates of 10^{-3}, 10^{-2}, 10^{-1}, and 1 s^{-1}. Cylindrical samples with a diameter and length of 6 and 10 mm, respectively, were used for this purpose.

3. Results and discussions

3.1 Precursor morphology and $Zr(Y)O_2$ particle size and distribution

The morphology of the precursors synthesised using the hydrothermal method is illustrated in Fig. 4. The precursor consisted of nanoplates, with a diameter of less than 20 nm and length of ~100 nm, as shown in Fig. 4a). The lattice fringe image indicated a spacing of 0.384 nm, corresponding to the (002) plane of hexagonal $(NH_4)_{0.33}WO_3 \cdot H_2O$ and this indicates the growth of nanoplates along the *c* axis [29].

Primary crystals ($WO_3 \cdot nH_2O$) precipitated from the crystal cell were initially formed by the hydrothermal reaction (Eq. (2)) between $(H_2W_{12}O_{40})^{6-}$ and H^+ [20]. Tungsten atoms in $WO_3 \cdot nH_2O$ are bound to six oxygen atoms in a regular octahedral coordination pattern, as shown in Fig. 4d). Each oxygen atom is shared by two octahedrons, which are arranged in layers to form six-membered rings and then form numerous hexagonal and trigonal tunnels by sharing equatorial oxygen in the ab plane (001) [30-32]. These rings are usually stacked by sharing oxygen along the *c* axis [001] and form hexagonal prisms. At the same time, due to their high concentration, NH_4^+ ions in the hydrothermal system occupied the hexagonal tunnels [33,34], thus accelerating the growth of hexagonal-prism-like WO_3 in the [001] direction and the formation of hierarchical $(NH_4)_{0.33}WO_3 \cdot H_2O$ nanoplates. The presence of NH_4^+ and H^+ can contribute to the formation of urchin-like h-WO_3 microspheres, as shown in Fig. 4b). During the hydrothermal reaction, numerous tiny WO_3 crystals nucleate and grow into WO_3 nanoplates due to the orientation effect of NH_4^+; these crystals self-assemble to form microspheres to reduce surface energy. The high concentration of NH_4^+ around WO_3 microspheres accelerates the oriented growth of WO_3. Thus, numerous nanoplates grow epitaxially from the surface of a microsphere. This may be due to the addition of ions (Zr^{4+}, Y^{3+}, and Cl^-) to the hydrothermal system and

breakage of order between the positive and negative charges destroying the self-assembly process, which leads to the transformation of agglomerated microspheres into relatively disperse cotton-like precursors.

$$(NH_4)_6H_2W_{12}O_{40}\cdot xH_2O + 6HNO_3 = 6NH_4NO_3 + 12WO_3\cdot nH_2O + (8-x)H_2O \quad (2)$$

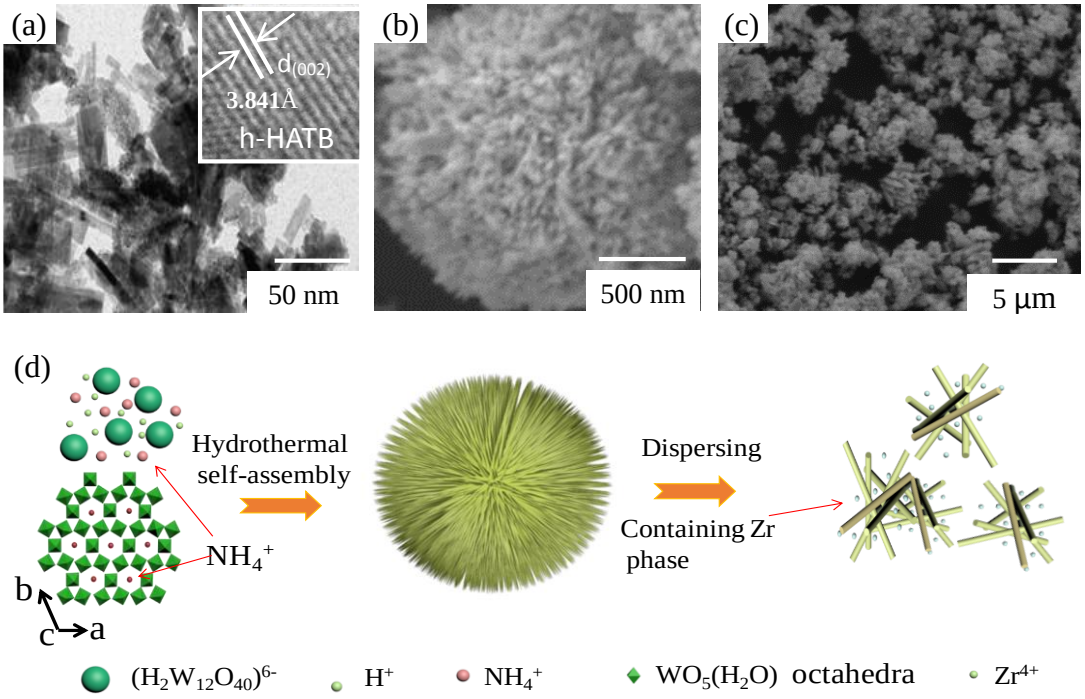

Fig. 4 Experimental observations and a schematic of α-HATB synthesis. a) TEM image of the undoped precursor, b) SEM image of the undoped precursor, c) SEM image of the doped precursor containing the (Zr, Y) phase, and d) illustration of morphology evolution in the $(NH_4)_{0.33}WO_3\cdot H_2O$ precursor

The size of oxide particles and their distribution in tungsten powders and alloys were studied (Fig. 5). A SEM image of the powder reduced at the optimised processing parameters is shown in Fig 5a). The powder particles exhibited small diameter and excellent dispersion, which is beneficial for increasing the uniformity and density of the microstructure during sintering. Further, nanoscale white particles, composed of $Zr(Y)O_2$, were scattered on the surfaces of tungsten particles, as shown

in Fig. 5a$_1$).

SPS was conducted to produce W-Zr(Y)O_2 alloys and investigate the effect of Zr(Y)O_2 particle size and distribution on the alloy microstructure, as shown in Fig. 5b). Oxde particle size was found to be uneven in the range of 100–500 nm. According to the magnified image of the selected area in Fig. 5b$_1$), a large number of white particles were found to be distributed within the grains, which helped in enhancing material properties. Moreover, a large number of nanoparticles (50 nm) were found to be distributed within the microstructure, as observed by TEM. A strong bonding was thus formed between the particles and tungsten phase even though there was no phase coherence between tungsten and the oxide, as shown in Fig. 5c$_1$).

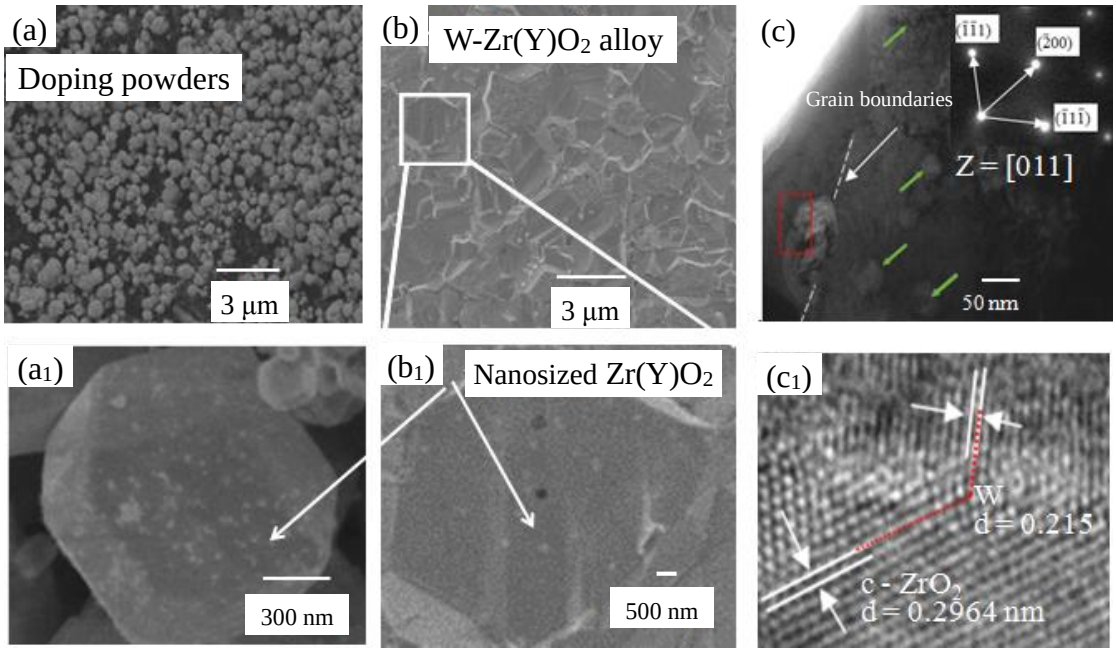

Fig. 5 Morphology and microstructure of W-Zr(Y)O_2 powders and alloys obtained using the proposed approach. a and a$_1$) SEM images of the morphology of the W-Zr(Y)O_2 powder. b and b$_1$) SEM images of the microstructure of the W-Zr(Y)O_2 alloy. c and c$_1$) TEM and HR-TEM images of the W-Zr(Y)O_2 alloy

The microstructure and mechanical properties of oxide particle dispersion-strengthened tungsten alloys (ODS-W) fabricated in this study were

compared with those reported earlier (alloys with the same or similar composition obtained by different processes as shown in Table 2). Fast sintering techniques, such as HIP, SPS, and sintering in vertical direction (VD), eliminate oxide particle growth. From Table 2, it may be inferred that L-L methods are better at yielding fine oxide particles in ODS-W alloys than L-S and S-S methods [35-37]. However, the size of these particles varied widely at 3.6, 1.5, and 2.5 μm. They were still much coarser than the oxide particles synthesised in tungsten alloys using the approach proposed in the current study. A similar observation could be made for ODS-W alloys fabricated by L-S methods. Yar et al. [40] prepared nanosized W-Y_2O_3 alloy by L-S doping. However, these Y_2O_3 particles were non-uniformly distributed in the tungsten matrix as the reaction occurred at the surfaces of the raw material alone (ammonium paratungstate, APT). Nanosized oxide particles were used as raw materials in S-S doping (mechanical alloying), but a large adsorption effect led to particle aggregation even after 30 h of ball milling [43]. In current research, the oxide particles obtained in tungsten alloys using the current approach were 0.8–10 times smaller when compared to those described in previous reports. This difference indicates that the proposed L-L doping process is appropriate to reduce particle size in tungsten alloys.

Table 2 Comparison of the microstructure and mechanical properties of ODS-W alloys

Doping process	**Sintering process**	**Alloy**	**W grain size (μm)**	**Oxide particle size (μm)**	**Density (g/cm^3)/Relative density (%)**	**Microhardness (HV)**	**Ref.**
L-L	SPS	W-6vol% Al_2O_3	3.64	>1.0	-/94.96	347.39	[35]
	SPS	W-2.5%ZrO_2	4.65	2.5	-/99.6	480	[36]
	VD	W-2.5%ZrO_2	40-80	1.5	-/98.7	-	[37]
L-S[a*]	VD	W-La_2O_3	50	3	-	-	[38]
	SPS	W-0.9wt.%La_2O_3	-	2	17.8/94	406	[39]
	SPS	W-1.0%Y_2O_3	2.3	Nanosize	17.5/92	423	[40]

				(Uneven)			
S-S	HIP	W-1%La_2O_3	-	>5	18.9/90.6	-	[41]
	HIP	W-Ti-0.5%Y_2O_3	2-5	>1.5	-	-	[42]
	SPS	W-5%HfO_2	11.6	>5	-/94.5	440	[43]
Current process	**SPS**	**W-0.5%Zr(Y)O_2**	**4.67 ± 0.5**	**0.25 ± 0.05**	**18.44/96.7 ± 0.2**	**472 ± 10**	**Present**

a* using APT as the tungsten source.

3.2 Microstructure of WHAs

The morphology of $WHA_{0.75}$ powder produced by the mechanical alloying of W-Zr(Y)O_2 powder with Ni and Fe powders is shown in Fig. 6a). It can be observed that the structure of the $WHA_{0.75}$ powder is much looser than that of W-Zr(Y)O_2 (Fig. 5a)). The microstructures of WHAs with different weight ratios of Zr(Y)O_2 are shown in Fig. 6(b–d). According to Fig. 6b), spherical tungsten grains are embedded in the matrix phase due to liquid-phase formation during sintering at 1400 °C [44]. It could be confirmed that the grain size of $WHA_{0.75}$ is smaller than that of WHA_0 after comparing the average size of 100 grains. W grains in alloys with and without Zr(Y)O_2 particles were uneven in size; the growth of W grains during liquid-phase sintering may be explained by Ostwald ripening [45]. In the current experimental conditions, smaller particles reprecipitated on larger tungsten grains during their dissolution in the matrix [46]. The uneven growth in tungsten grain size may be attributed to the low sintering temperatures and short durations, which decrease the mobility and effective diffusion of W atoms.

Moreover, grain contiguity reduced slightly as the grain size decreased, similar to previously reported results [47]. The reason for the decrease in W-W contiguity is that Zr(Y)O_2 particles induce the liquid phase $\gamma(Fe_{0.64}N_{0.36})$ to infiltrate W grain boundaries during sintering [48]. Thus, tungsten grains are gradually covered by the $\gamma(Fe_{0.64}N_{0.36})$ phase to enhance the mechanical properties of oxide particle dispersion-strengthened WHAs (ODS-WHAs).

A magnified image of the area enclosed in red in Fig. 6c) is presented in Fig. 6d) to understand the microstructure of $WHA_{0.75}$ in further detail. A large number of white particles with similar particle size of less than 200 nm could be observed. These $Zr(Y)O_2$ particles were dispersed in W grains. Generally, large oxide particles induce stress/strain concentration for crack initiation and reduce the fracture toughness of an alloy [49]. Therefore, nanosized $Zr(Y)O_2$ particles (such as those in the present alloy) obtained by the proposed process are expected to enhance the mechanical properties of WHAs.

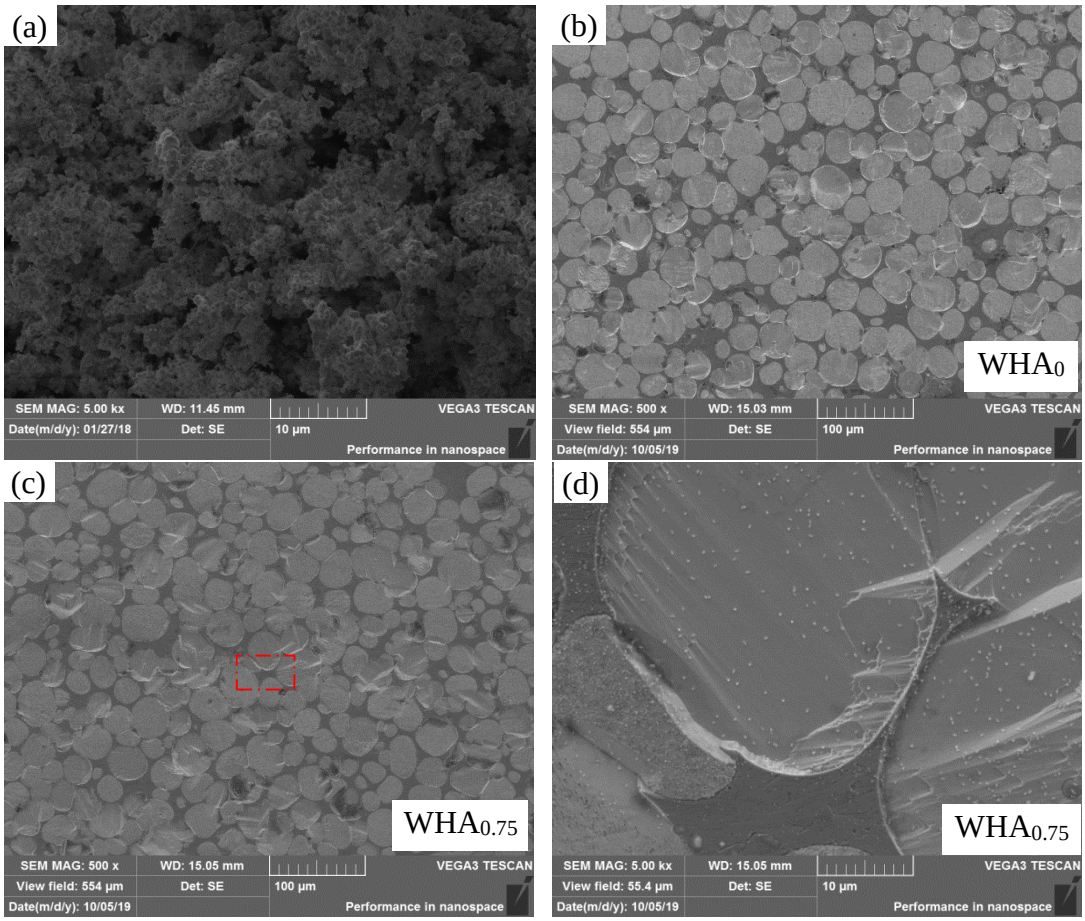

Fig. 6 SEM images of the microstructure of a) $WHA_{0.75}$, b) WHA_0, and c) and d) $WHA_{0.75}$ at 500x and 5000x, respectively

The microstructure of $WHA_{0.75}$ after quasi-static compressive loading at room temperature (27 °C) was characterized by TEM. As shown in Fig. 7a)–c), oxide nanoparticles with prismatic and subspherical structure exhibited different particle sizes. In Fig. 7a), it may be observed that the prismatic particles surrounded by a

black phase were ~200 nm in size. In Fig. 7b) and c), it can be seen that subspherical particles smaller than 50 nm were embedded in shallow phases consisting of Ni, Fe, and W, as described by EDS. White cubic nanocrystalline $Zr(Y)O_2$ particles were detected in the selected area electron diffraction (SAED) pattern in the inset of Fig. 7a). Dislocation substructures are marked by white arrows in the matrix phase, as shown in Fig. 7c). Meanwhile, Fig. 7d) illustrates a well-bonded interface between the tungsten phase and $Zr(Y)O_2$ even though there was no coherent relationship.

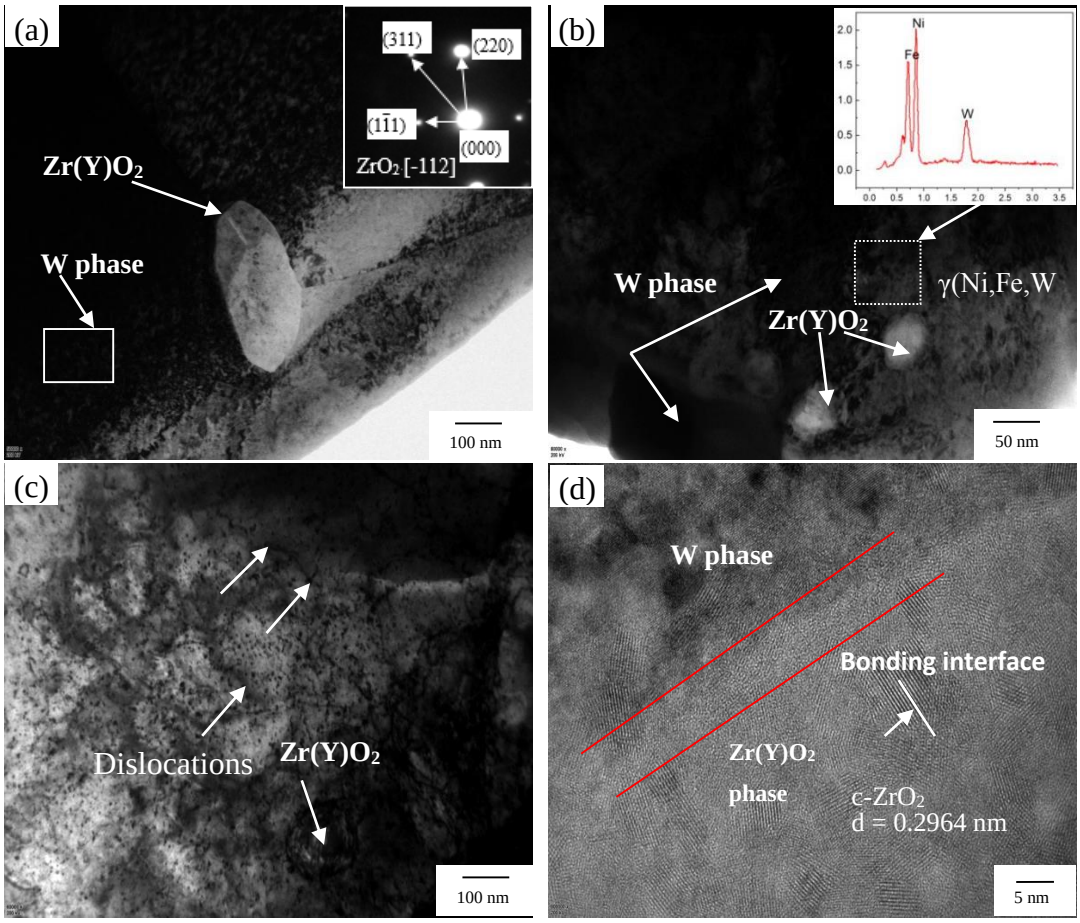

Fig. 7 a) and b) TEM images of $WHA_{0.75}$, c) TEM image of the matrix phase, and d) HRTEM image of the $Zr(Y)O_2$/W interface

The microstructures of several heavy tungsten alloys reinforced by ZrO_2 particles are shown in Fig. 8. Daoush et al. [49] fabricated W-Ni-ZrO_2 alloys by conventional sintering at 1500 °C for 1 h. The ZrO_2 particles in these alloys ranged from 0.5 to 3 μm in size, as shown in Fig. 8a), and they were almost at or close to the grain

boundaries. Lee et al. [51] fabricated partially stabilised zirconia (PSZ) dispersion-strengthened WHAs by two-step mechanical alloying to control the location of oxide particles. However, the PSZ particles in the alloys still grew to be as large as 1.5 μm, as shown in Fig. 8b), and some adhesive oxide particles marked by red arrows could be observed. Xu et al. [47] studied $Zr(Y)O_2$ dispersion-strengthened 92.5W-4.9Ni-2.1Fe alloys using azeotropic distillation process. In these alloys, the $Zr(Y)O_2$ particles were 200–1000 nm large, as shown in Fig. 8c). Wang et al. [36] synthesised W-ZrO_2 alloys using a combination of the hydrothermal method and SPS. In this case, agglomerated precursors could be detected and the adhesive ZrO_2 particles grew to 3 μm, as shown in Fig. 8d). In addition, other large oxide particles (La_2O_3, Y_2O_3, and Al_2O_3) were also used to strengthen tungsten alloys (Table 2 and 3). Non-uniformly distributed coarse particles induce uneven stress and strain distribution around these reinforced particles, thus weakening the alloys.

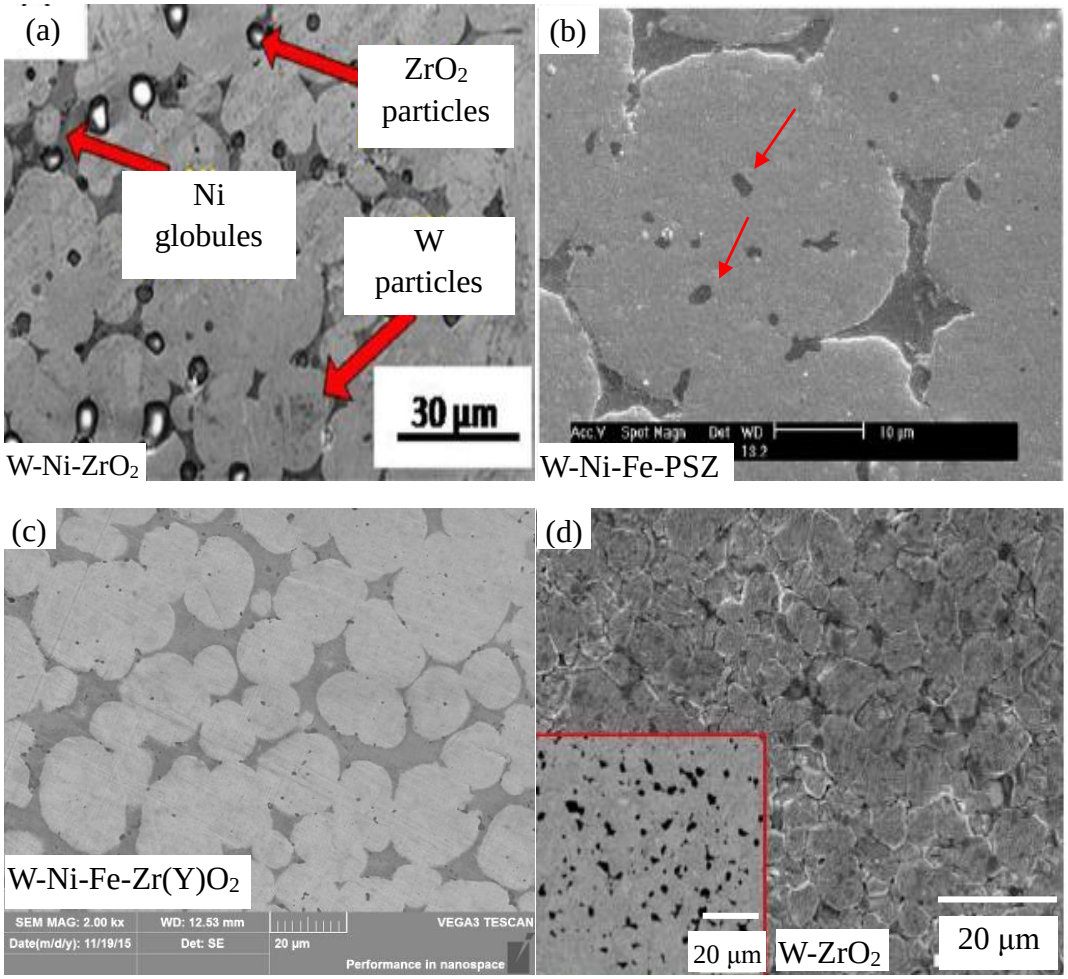

Fig. 8 Microstructures of WHAs reinforced by ZrO_2 particles. a) W-Ni-ZrO_2 [49], b) W-Ni-Fe-PSZ [51], c) W-Ni-Fe-ZrO_2 [47], and d) W-ZrO_2 [36]

Table 3 Microstructure and mechanical properties of ODS-WHA reported in the literature and in the current study

Heavy tungsten alloy	**Sintering process**	**RD (%)**	**Grain size (μm)**	**Particle size (μm)**	**Hardness (HV)**	**Ref.**
W-Ni-Fe-0.3PSZ	1480 °C (1 h)	-	18	0.8	-	[49]
W-Ni-Fe-1Al_2O_3	1480 °C (2 h)	98.3	36.8	7	-	[52]
W-Ni-Fe-xY2O3	1850 °C (1 h)	99.1	19.5	0.6-1.3	-	[10]
W-Ni-Fe-Co-Y_2O_3	1450 °C (1 h)	94.1	12	>0.6	425	[44]
94W-4.56Ni-1.14Fe-Y_2O_3	1485 °C (1 h)	99.0	15	0.65	-	[53]
Previous W-ODS	SPS/HIP	<99.9	<10	1-5	406-480	[27]
93W-4.9Ni-2.1Fe-Zr(Y)O_2	1520 °C (2.5 h)	99.2	28	0.5-1	402	[47]
$WHA_{0.75}$	**1400 °C (2.5 h)**	**99.5 ± 0.1**	**25 ± 2**	**0.2-1**	**407 ± 10**	**Present**

Intracrystalline heavy tungsten alloys reinforced with nanosized c-Zr(Y)O_2 particles were fabricated in this study; the consequent formation and distribution of c-Zr(Y)O_2 particles during L-L doping at the ionic level are shown in Fig. 9. The formation of nanosized yttria-stabilised cubic zirconia is attributed to the L-L incorporation of Zr^{4+} and Y^{3+} ions; $Y(NO_3)_3$ solution was added slowly to a $ZrOCl_2{\cdot}8H_2O$ solution while stirring to obtain a cluster solution [47]. Though $ZrOCl_2 \cdot 8H_2O$ dissolves in strong acid solutions, it undergoes hydrolysis in aqueous solutions and Cl^- ions in the outer sphere of the ionic complex are replaced by OH^- groups (Eq. (3)) [27]. Subsequently, $[Zr_4(OH)_8\ 16H_2O]^{8+}$ units react with the hydroxyl ions to form $Zr(OH)_4$ sols [27].

$$\{[Zr_4(OH)_8{\cdot}16H_2O]^{8+}8Cl^-\} + 4H_2O = \{[Zr_4(OH)_8{\cdot}16H_2O]^{8+}\ 8OH^-\} + 8HCl\uparrow \quad (3)$$

However, the generated $Zr(OH)_4$ easily decomposes in acidic conditions to yield Zr^{4+}. During the hydrothermal reaction, $W_{12}O_{40}^{8-}$ ions are introduced from the hydrolysis of AMT (Eq. (4)) [23] after which Zr^{4+} and Y^{3+} ions reacts with $W_{12}O_{40}^{8-}$

ions to produce $Zr(WO_4)_2$ and $Y_2(WO_4)_3$ (Eqs. (5) and (6)) [47,54]. Y_2O_3 penetrates oxygen vacancies in the zirconia lattice to form stabilized $Zr(Y)O_2$ during sintering [55].

$$(NH_4)_6H_2W_{12}O_{40} = 6NH_4^+ + 2H^+ + W_{12}O_{40}^{8-} \quad (4)$$

$$2Zr(OH)_4 + 8H^+ + W_{12}O_{40}^{8-} = 8WO_3 \downarrow + 2Zr(WO_4)_2 \downarrow + 8H_2O \quad (5)$$

$$2Y^{3+} + 2H^+ + W_{12}O_{40}^{8-} = 9WO_3 \downarrow + Y_2(WO_4)_3 \downarrow + H_2O \quad (6)$$

The refining effect of oxide particle size is limited to doping with nanosized particles due to the high adsorption capacity [44,56]. In the present investigation, WHA-$Zr(Y)O_2$ powders were prepared by the mechanically alloying of ultrafine W-$Zr(Y)O_2$ powders with Ni and Fe powders. In the alloys, nanosized $Zr(Y)O_2$ particles with size less than 200 nm were distributed on the surface of tungsten particles. Moreover, WHA-$Zr(Y)O_2$ exhibited a highly uniform nanoparticle distribution when compared to alloys produced by other powder processing methods. This indicates that L-L doping and mechanical alloying, when combined together, are highly effective at reducing the particle size in strengthened tungsten alloys.

Conventionally, ODS-WHA powders are prepared by doping WHA powders with oxide particles, which often leads to oxide particle agglomeration and growth at the grain boundaries. In current research, during liquid sintering, Ni and Fe powder particles are transformed into a liquid phase, which allows the diffusion of only a small amount of tungsten. Meanwhile, some of the $Zr(Y)O_2$ particles at the grain boundaries of W powders are drawn into liquid phase and they are retained in the γ(Fe, Ni, and W) matrix. Eventually, most of the c-$Zr(Y)O_2$ particles are distributed in W grains and only a small number of c-$Zr(Y)O_2$ particles are distributed in the γ(Fe, Ni, and W) matrix.

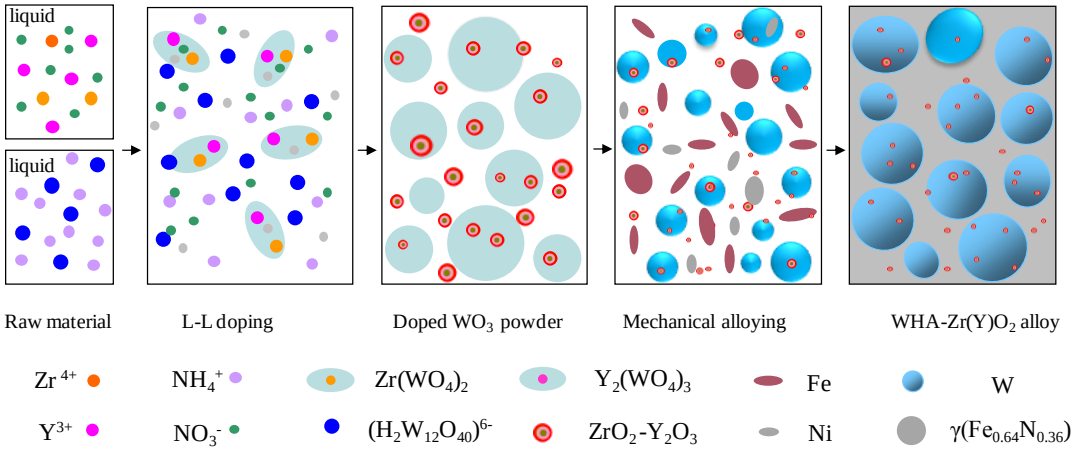

Fig. 9 Schematic of microstructural development during alloy fabrication

3.3 Mechanism of grain refinement in WHAs

Tungsten grain growth in ODS-WHAs is mainly dependent on oxide particle refinement during sintering [10,50]. However, grain refinement is complicated due to the retardation of grain growth and coarsening under different sintering conditions. Bock et al. [57] suggested that oxide particles inhibited grain growth to prevent grain coarsening. Kang et al. [58] indicated that secondary phase particles led to an increase in grain curvature. Annavarapu et al. [59] proposed that the diffusion distance of tungsten atoms increased in the presence of large secondary phase particles. Oxide particles at the tungsten-matrix (W-M) interface can block diffusion between tungsten and the matrix, which delays grain growth during WHA liquid phase sintering [52]. The doped secondary phase particles at grain boundaries affected tungsten grain size by preventing migration along the grain boundaries and reducing the growth rate [60]. This relationship can be expressed as follows (7):

$$R = 4r/3\varphi \tag{7}$$

where R is the grain size of the tungsten phase, r is the radius of secondary phase particles, and φ is the volume fraction of the secondary phase particles.

According to Eq. (7), the grain size of tungsten particles depends on the size of oxide particles; in other words, tungsten grain size can be reduced if the size of the oxide particles located at the grain boundaries decreases.

The relationship between tungsten grain size and size of the oxide particles in

ODS-WHAs observed in this study as well as in previous investigations is illustrated in Fig. 10. In general, W grain size was proportional to oxide particle size, except in the WHAs described in this study and those in Ref. [47]. These two WHAs with a large number of $Zr(Y)O_2$ particles uniformly dispersed in tungsten grains are shown in the same plot; in this case, the relationship between grain size and oxide particle size was not linear. This is because of the dispersion of $Zr(Y)O_2$ particles within tungsten grains, leading to a not very obvious refinement of W grains. This observation further confirms the advantages of the L-L doping for preparing intragranular particle-strengthened tungsten alloys.

Table 4 Comparison of the microstructural parameters and sintering conditions of WHAs reported in the literature and current study

Heavy tungsten alloy	Sintering processing parameters [a]*	RD (%)	Grain size (μm)	Contiguity	Matrix volume fraction	Ref.
90W-7Ni-2Fe-1Co	1460 °C (2 h)	-	36	0.42	0.34	[62]
93W-4.9Ni-1.4Fe-0.7Co	1460 °C (2 h)	-	47	0.55	0.22	
95W-3.5Ni-1Fe-0.5Co	1460 °C (2 h)	-	59	0.73	0.16	
90W-7Ni-3Fe	1460 °C (2 h)	-	32	0.51 ± 0.2	14.3 ± 3.3	[46]
90W-6Ni-2Fe-Co	1470 °C (2 h)	-	47	0.62 ± 0.2	15.2 ± 2.1	
W-5.6Ni-1.4Fe	1485 °C (1 h)	99.9	34.5	-	-	[10]
W-Ni-Fe	1480 °C (2 h)		56	0.53 ± 0.05	0.14	[63]
W-Ni-Fe-Co		-	54	0.43 ± 0.01	0.17	
W-Ni-Fe-Re		-	49	0.48 ± 0.06	0.16	
93W-4.9Ni-2.1Fe	1520 °C (1.5h)	99.1	45.5	0.32 ± 0.04	-	[52]
95W-2.8Ni-1.2Fe-Al_2O_3		98.2	36.8	0.60 ± 0.06	-	
INERMET® IT180[b]*	-	-	100	-	-	[64]
95W-3.5Ni-1.5Cu	1510 °C (1.5 h)	98.4	60	0.60	-	[65]
96W-3Ni- 1Cu	1510 °C (1.5 h)	98.4	70	0.70	-	
90W-4xNi-xCo	1600 °C (1 h)	99.2	34	-	-	[45]
Conventional WHA[c]*	-	-	40-60	-	-	[9]
94W-4.56Ni-1.14Fe-Y_2O_3	1485 °C (1 h)	99%	15	0.75	0.112	[53]
WHA_0	**1400 °C (2 h)**	**99.5% ± 0.1**	**41 ± 2**	**0.53 ± 0.03**	**0.37 ± 0.015**	**Current study**
$WHA_{0.75}$	**1400 °C (2 h)**	**99.3% ± 0.1**	**37 ± 2**	**0.47 ± 0.03**	**0.42 ± 0.023**	

a* Maximal sintering temperature and duration time

b* Heavy tungsten alloy reported in [64]

c* Microstructure and properties of the heavy tungsten alloy are not known.

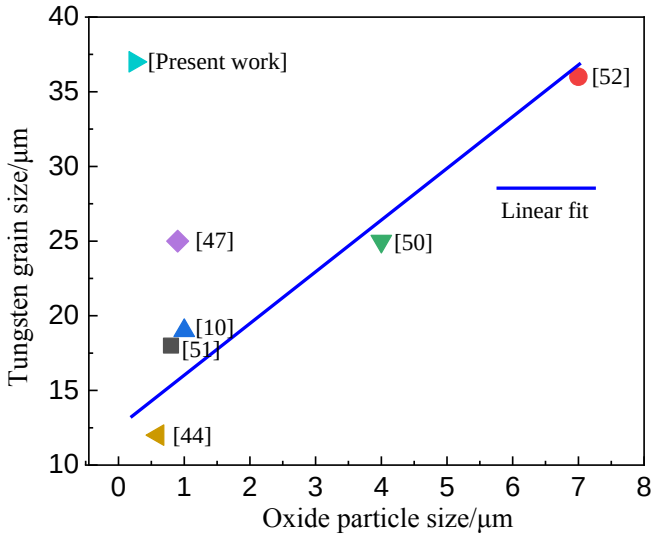

Fig. 10 Relationship between tungsten grain size and oxide particle size in ODS-WHAs reported in the current and past studies

The grain size of $Zr(Y)O_2$ particle-dispersion-strengthened WHAs described in this study was also compared with that in WHAs sintered using different methods (Table 4). The factors responsible for a fine original tungsten grain size (G_0) also contributed to grain refinement; the relationship between G_0 and refined grain size is as follows [61],

$$G^3 = G_0^3 + Kt \quad (8)$$

where G is the mean W grain size at time t, G_0 is the original average W grain size at the onset of coarsening, and K is the rate constant.

In this study, mechanical alloying was conducted to produce small W particles. Internal defects caused by the significant strain on these particles due to the high impact forces generated during ball milling serve as additional nucleation sites for strain-free grains and homogenise the grain size [66]. Fan et al. [67] indicated that mechanical alloying powders affected the mechanism of sintering and contributed to fine tungsten grains in heavy alloys.

The alloys listed in Table 4 exhibited large and coarse grains as the sintering temperature increased (>1400 °C). As sintering is a diffusion-controlled process, alloys sintered at higher temperatures exhibit higher sintering and coarsening rates [68]. Moreover, high-temperature sintering results in a constant flow of the binder

phase through pores between W grains [48] and increases the final relative sintering density. The alloys described in this study exhibit a high RD comparable with the RD of alloys reported in the literature (Table 4). This is because the high pressure applied during sintering accelerates W atom diffusion [69,70]. In addition, the oxide particles also enhance the densifications process and decrease the porosity by capturing the oxygen in the matrix.

3.4 Mechanical properties of WHA-Zr(Y)O_2 alloys

Uniaxial tensile tests were conducted to measure the ultimate tensile strength (UTS) of WHA-Zr(Y)O_2 at room temperature (27 °C). The strengths of WHA_0 and $WHA_{0.5}$ were compared with those reported in literature, as shown in Fig. 11a). The ultimate tensile strengths of WHA_0 and $WHA_{0.50}$ were 937 and 895 MPa, respectively, which exhibit higher strengths compared to state of the art.

Fig. 11b)–d) show the fracture surfaces of the failed tensile samples of 90W-7Ni-3Fe (90WHA) [9], 90W-7Ni-3Fe-0.04Y_2O_3 (90WHA-0.04Y_2O_3) [9], and $WHA_{0.50}$, respectively. As shown in Fig. 11b) and c), W-W intergranular rupture is the dominant mode of fracture in 90WHA. However, a few W grain transgranular fractures and pore surfaces are still observed in 90WHA-0.04Y_2O_3. Although the strength of present $WHA_{0.50}$ alloy is lower than that of the 90WHA-0.04Y_2O_3 alloy, $WHA_{0.50}$ shows visual evidence of W-W cleavage patterns and the ductile failure behaviour of the matrix. This contradictory situation would be researched in follow-up studies.

From these results, it may be inferred that oxide particles have a significant effect on the mechanical properties of the tested alloys. Too low or too high content of rare earth oxide additions would result in its different strengthening effect on tensile properties. Fan et al. [9] reported that WHAs with 0.4 wt.% oxide particles exhibited a tensile strength of 1124 MPa. In contrast, the additions of 0.1 wt.%, 0.8 wt.%Y_2O_3 into alloy decreased the maximal strength value of the alloy compared to WHA without Y_2O_3 (923 MPa). Lee et al. fabricated PSZ (0–0.3wt.%) dispersion-strengthened WHAs [51]; the ultimate tensile strengths of these alloys

decreased with the addition of PSZ particles (as indicated by the red symbols in Fig. 11a)). A similar phenomenon occurred with the addition of 1% Al_2O_3 and 0.1% Y_2O_3 [10,52]. In these two alloys, the additions of oxide particles both decrease the strength values of WHAs. This indicates that a non-optimal oxide content deteriorates the tensile properties of alloys.

In addition to the oxide content, the mechanical properties of alloys depend on oxide particle distribution. In case oxide particles are agglomerated, fracture initiation might occur from these areas during tensile tests. Cracks are generated at these spots and later propagate, leading to fracture [78,79]. Moreover, rare earth oxide aggregates in the matrix or at the W-M interface restrain matrix deformation, which decreases the strength and elongation of WHAs.

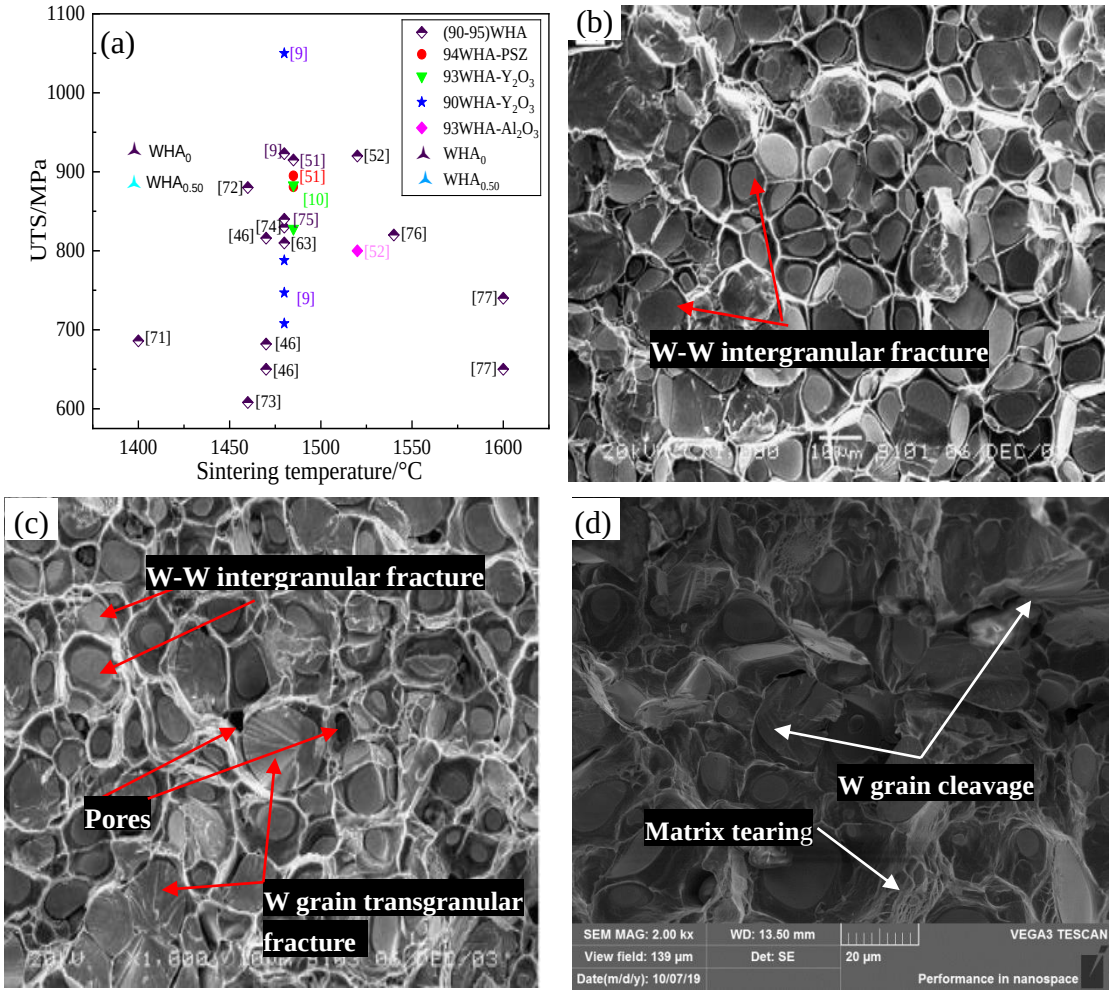

Fig. 11 Tensile properties and fracture surfaces of WHAs and ODS-WHAs described in the present work and literature. a) ultimate tensile strengths of WHAs and

ODS-WHAs vs. their sintering temperature, b) fracture surfaces of 90WHA [9], c) 90WHA-0.04Y_2O_3 [9], and d) $WHA_{0.50}$

The compressive properties of WHAs reinforced with different amounts of $Zr(Y)O_2$ particles were investigated and compared as shown in Fig. 12. The engineering stress-strain curves and the corresponding true stress-strain curves of WHA-$Zr(Y)O_2$ were plotted at room temperature (27 °C) (Fig. 12a) and b), respectively). During compressive testing, elastic deformation occurs initially with a linear relationship between stress and strain, followed by plastic deformation in the alloy. Beyond an engineering strain of 0.813, stress increased while the strain remained constant, as shown in Fig. 12a). This indicates the high plasticity of WHAs.

The matrix phase of WHAs is softer than the tungsten phase, which determines the plastic deformation capacity of the alloys during quasi-static compression. In the alloys described in the present study, the matrix phase containing a solid $Zr(Y)O_2$ phase exhibited good plasticity. This is due to the fact that some nanosized $Zr(Y)O_2$ particles were uniformly distributed in the matrix with a good interface. These ultrafine oxide particles reduced stress and strain concentration during compressive deformation [80].

Based on the true stress-strain curves in Fig. 12b), the WHA containing 0.5% $Zr(Y)O_2$ exhibited the best strengthening behaviour among all the tested alloys. The ultimate compressive strength of $WHA_{0.50}$ was 1445 MPa, which was higher than that of the other three alloys. Furthermore, we observed that the ultimate compressive strength obtained during plastic deformation is affected by the strain rate; to illustrate this phenomenon, we tested the alloy samples at strain rates of 10^{-3}, 10^{-2}, 10^{-1}, and 1 s^{-1}, as shown in Fig. 13.

Fig. 13a) indicates that WHA-$Zr(Y)O_2$ exhibited excellent plasticity at different strain rates. The ultimate stress increased with an increase in the strain rate, as shown in Fig. 13b). An ultimate stress of 1445 MPa was achieved at 10^{-3} s^{-1}. The compressive strength of $WHA_{0.50}$ was higher than that of several previously reported alloys, as shown in Fig. 13c). This higher value of strength may be due to the proper amount of $Zr(Y)O_2$ particles and higher dispersed nanoparticles distribution. When the

strain rate increases to 1 s^{-1}, the peak stress increases to 1560 MPa. On the one hand, a high strain rate enhances dislocation density and work hardening. On the other hand, the change of phase' deformation behaviors may be another main reason. The deformed microstructures produced at different strain rates are shown to illustrate the plastic deformation behaviour of WHA-Zr(Y)O_2 (Fig. 14a)–d)).

During compression, the matrix phase is the first to deform. When tests are conducted at low strain rates, the matrix phase has sufficient time to deform and flow between tungsten particles, as confirmed by the slightly elongated microstructure of tungsten grains in Fig. 14a). With the further increasing of plastic deformation, the matrix phase causes work hardening by plastic deformation, which induces a simultaneous deformation in some tungsten particles. The deformation resistance of the matrix phase depends on the oxide particles used to reinforce it. When the strain rate during compression increases, there is not enough time for the matrix phase to flow between W particles, owing to which it gradually transmits stress to W grains, leading to their deformation. Beyond a critical strain rate, the deformation resistance of the alloy mainly depends on the tungsten phase. Therefore, W particles were seriously elongated at 1 s^{-1}, as shown in Fig. 14d).

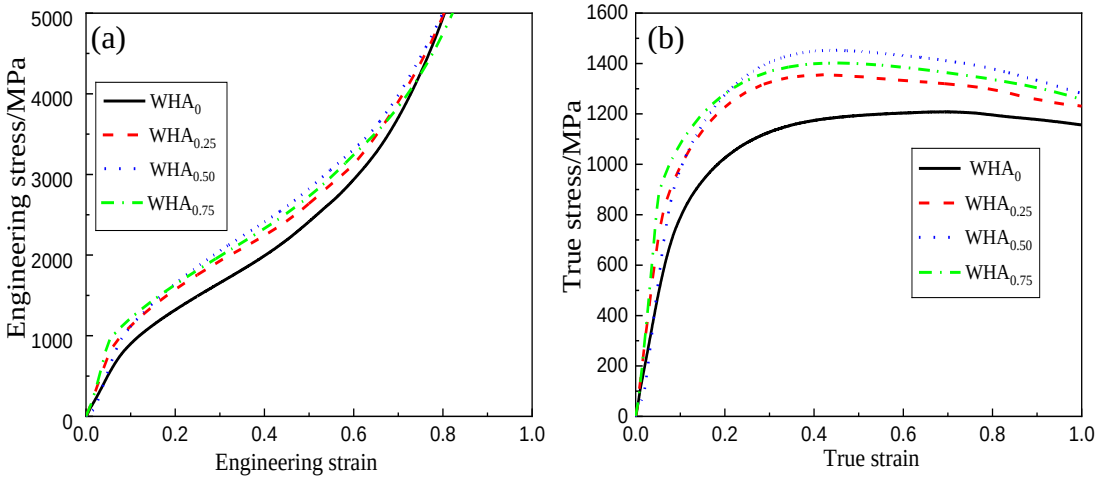

Fig. 12 a) Room temperature (27 °C) engineering stress-strain curves and b) true stress-strain curves of WHAs with different mass fractions of Zr(Y)O_2. Compression tests were conducted at a constant strain rate of 10^{-3} s^{-1}.

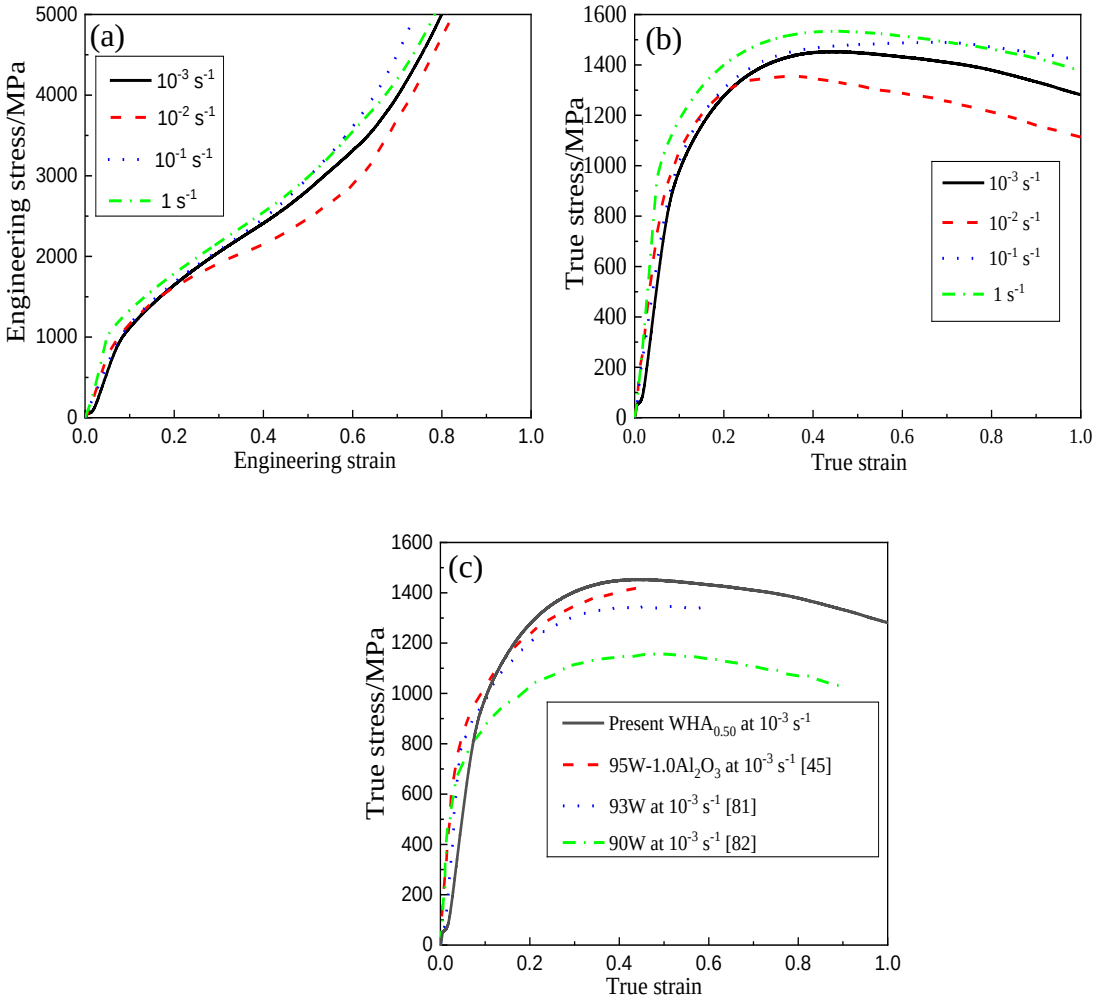

Fig. 13 a) Room temperature (27 °C) engineering stress-strain curves and b) true stress-strain curves of $WHA_{0.50}$generated during compression tests at different strain rates. c) Comparison of the compressive true stress-strain curve of $WHA_{0.50}$ with those of previously reported alloys

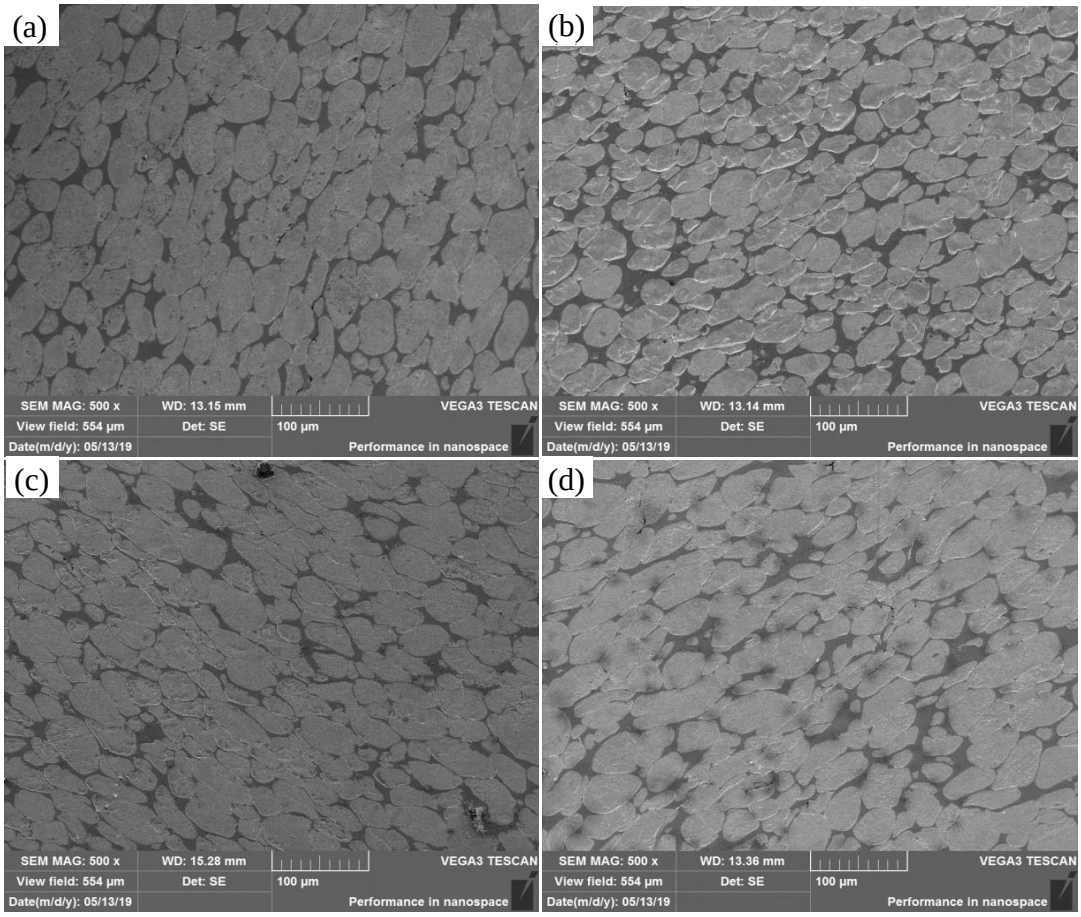

Fig. 14 Microstructure of $WHA_{0.75}$ after compression tests at room temperature (27 °C) at strain rates of a) 10^{-3}, b) 10^{-2}, c) 10^{-1}, and d) 1 s^{-1}

4. Conclusion

(1) WHAs strengthened by highly uniform nanosized $Zr(Y)O_2$ particles were fabricated by hydrothermal processing followed by mechanical alloying and hot isostatic pressing.

(2) $Zr(Y)O_2$ particles bonded well with the tungsten phase; they were smaller than 200 nm in size and were distributed uniformly in tungsten grains and the matrix. TEM analysis indicated the presence of a large number of nanosized oxide particles smaller than 50 nm in the alloy microstructure.

(3) The size of $Zr(Y)O_2$ particles synthesised using combined hydrothermal and mechanical alloying methods is much smaller than that in alloys previously reported; this small size also helped in tungsten grain refinement.

(4) The ultimate tensile and maximal compressive strengths of the fabricated alloys under quasi-static deformation at room temperature (27 °C) were 895 and 1420 MPa, respectively, which are much higher than the values reported in literature. The effect of $Zr(Y)O_2$ particles and strain rate on the compressive properties of the alloys were investigated in detail and the corresponding compressive deformation mechanisms were discussed.

Declaration of interest

There are no conflicts to declare.

Acknowledgments

National Natural Science Foundation of China [No. U2004180, No. 51874185], Henan Province Science and Technology Innovation Talent Plan [No. 2017JQ0012] and Graduate Research and Innovation & Practice Projects in Jiangsu Province [No. KYCX19_0182]. The EIPHI Graduate School (contract ANR-17-EURE-0002) also has supported this work.

References

[1] R. Cury, F. Issartel, J. M. Joubert, H. Couque, Evolution of cobalt-free tungsten heavy alloys for kinetic energy penetrators, Powder Metall. 56 (2013) 347-350. https://doi.org/10.1179/0032589913Z.000000000137.

[2] D. W. Guo, T. K. Chi, A corrosion study on W-Cu alloys in sodium chloride solution at different pH, J. Mater. Process. Technol. (2020) In Press. https://doi.org/10.1016/j.jmst.2020.03.031.

[3] Y. Yu, H. Hu, W. Zhang, X. Xu, Microstructure evolution and recrystallization after annealing of tungsten heavy alloy subjected to severe plastic deformation, J. Alloys Compd. 685 (2016) 971-977. https://doi.org/10.1016/j.jallcom.2016.07.004.

[4] Z. C. Cordero, R. R. Carpenter, C. A. Schuh, B. E. Schuster, Sub-scale ballistic testing of an ultrafine grained tungsten alloy into concrete targets, Int. J. Impact Eng. 91 (2016) 1-5. https://doi.org/10.1016/j.ijimpeng.2015.11.013.

[5] X. F. Liu, Z. L. Tian, X. F. Zhang, H. H. Chen, T. W. Liu, Y. Chen, Y. J. Wang, L. H. Dai, “Self-sharpening” tungsten high-entropy alloy, Acta Mater. 86 (2020) 257-266. https://doi.org/10.1016/j.actamat.2020.01.005.

[6] A. Kumari, M. Sankaranarayana, T. K. Nandy, On structure property correlation in high strength tungsten heavy alloys, Int. J. Refract. Met. Hard Mater. 67 (2017) 18-31. https://doi.org/10.1016/j.ijrmhm.2017.05.002.

[7] G. Prabhu, N. A. Kumar, M. Sankaranarayana, T. K. Nandy, Tensile and impact properties of microwave sintered tungsten heavy alloys, Mater. Sci. Eng. A. 607 (2014) 63-70. https://doi.org/10.1016/j.msea.2014.03.130.

[8] O. Dincer, M. K. Pehlivanoglu, N. K. Caliskan, I. Karakaya, A. Kalkanli, Processing and microstructural characterization of liquid phase sintered tungsten-nickel-cobalt heavy alloys, Int. J. Refract. Met. Hard Mater. 50 (2015) 106-112. https://doi.org/10.1016/j.ijrmhm.2014.12.009.

[9] J. L. Fan, L. Tao, H. C. Cao, D. L. Wang, Preparation of fine grain tungsten heavy alloy with high properties by mechanical alloying and yttrium oxide addition, J. Mater. Process. Tech. 208 (2008) 463-469. https://doi.org/10.1016/j.jmatprotec.2008.01.010.

[10] H. J. Ryu, S. H. Hong, Fabrication and properties of mechanically alloyed oxide-dispersed tungsten heavy alloys, Mater. Sci. Eng. A. 363 (2003) 179-184. https://doi.org/10.1016/S0921-5093(03)00641-5.

[11] Y. Yu, C. Ren, W. Zhang, Compressive behavior of liquid phase sintered 90 W-7Ni-3Fe heavy alloy at high temperature and low strain rate condition. Int. J. Refract. Met. Hard Mater. 76 (2018) 149-157. https://doi.org/10.1016/j.ijrmhm.2018.06.006.

[12] A. Xu, D. E. Armstrong, C. Beck, M. P. Moody, G. D. Smith, P. A. Bagot, S. G. Roberts, Ion-irradiation induced clustering in W-Re-Ta, W-Re and W-Ta alloys:

An atom probe tomography and nanoindentation study, Acta Mater. 124 (2017) 71-78. https://doi.org/10.1016/j.actamat.2016.10.050.

[13] S. Park, D. K. Kim, S. Lee, R. Hojin, H. S. Hyung, Dynamic deformation behavior of an oxide-dispersed tungsten heavy alloy fabricated by mechanical alloying, Metall. Mater. Trans. A. 32 (2001) 2011-2020. https://doi.org/10.1007/s11661-001-0013-1.

[14] J. W. Li, F. Fang, Z. Wang, G. S. Zhang, S. Z. Wei, L. J. Xu, K. M. Pan, Microstructure and properties characterization of W-25Cu composite materials liquid-liquid doped with La_2O_3, Int. J. Refract. Met. Hard Mater. 71 (2018) 115-121. https://doi.org/10.1016/j.ijrmhm.2017.10.019.

[15] W. Hu, Z. Dong, L. Yu, Z. Ma, Y. Liu, Synthesis of W-Y_2O_3 alloys by freeze-drying and subsequent low temperature sintering: microstructure refinement and second phase particles regulation, J. Mater. Process. Technol. 36 (2020) 84-90. https://doi.org/10.1016/j.jmst.2019.08.010.

[16] Z. Dong, N. Liu, W. Hu, Z. Ma, C. Li, C. Liu, Q. Y. G, Y. Liu, Controlled synthesis of high-quality W-Y_2O_3 composite powder precursor by ascertaining the synthesis mechanism behind the wet chemical method, J. Mater. Process. Technol. 36 (2020) 118-127. https://doi.org/10.1016/j.jmst.2019.05.067.

[17] L. Ding, D. P. Xiang, Y. Y. Li, Y. W. Zhao, J. B. Li, Phase, microstructure and properties evolution of fine-grained W-Mo-Ni-Fe alloy during spark plasma sintering, Mater. Des. 37 (2012) 8-12. https://doi.org/10.1016/j.matdes.2011.12.010.

[18] Y. Y. Li, K. Hu, X. Q. Li, X. Ai, S. G. Qu, Fine-grained 93W-5.6Ni-1.4Fe heavy alloys with enhanced performance prepared by spark plasma sintering, Mater. Sci. Eng. A. 573 (2013) 245-252. https://doi.org/10.1016/j.msea.2013.02.069.

[19] G. Prabhu, N. A. Kumar, M. Sankaranarayana, T. K. Nandy, Tensile and impact properties of microwave sintered tungsten heavy alloys, Mater. Sci. Eng. A. 607 (2014) 63-70. https://doi.org/10.1016/j.msea.2014.03.130.

[20] T. Sadat, G. Dirras, D. Tingaud, M. Ota, T. Chauveau, D. Faurie, S. Vajpai, K. Ameyama, Bulk Ni–W alloys with a composite-like microstructure processed by

spark plasma sintering: Microstructure and mechanical properties, Mater. Des. 89 (2016) 1181-1190. https://doi.org/10.1016/j.matdes.2015.10.083.

[21] L. Xu, Q. Yan, M. Xia, L. Zhu, Preparation of La_2O_3 doped ultra-fine W powders by hydrothermal-hydrogen reduction process, Int. J. Refract. Met. Hard Mater. 36 (2013) 238-242. https://doi.org/10.1016/j.ijrmhm.2012.09.005.

[22] Z. Dong, N. Liu, Z. Q. Ma, C. X. Liu, Q. Y. Guo, Y. Yusuke, H. R. Alamri, Z. A. Alothman, M. S. Hossain, Y. C. Liu, Synthesis of nanosized composite powders via a wet chemical process for sintering high performance W-Y_2O_3 alloy, Int. J. Refract. Met. Hard Mater. 69 (2017) 266-272. https://doi.org/10.1016/j.ijrmhm.2017.09.001.

[23] F. N. Xiao, Q. Miao, S. Z. Wei, K. Pan, J. W. Li, W. Liu, L. J. Xu, Hydrothermal synthesis of nanoplates assembled hierarchical h-WO_3 microspheres and phase evolution in preparing cubic Zr(Y)O_2-doped tungsten powders, Adv. Powder Technol. 29 (2018) 2633-2643. https://doi.org/10.1016/j.apt.2018.07.011.

[24] H. Zhang, W. Deng, Z. M. Xie, R. Liu, J. F. Yang, C. S. Liu, X. P. Wang, Q. F. Fan, Y. Xiong, Recent progresses on designing and manufacturing of bulk refractory alloys with high performances based on controlling interfaces, J. Mater. Process. Technol. (2020) In Press. https://doi.org/10.1016/j.jmst.2020.02.046.

[25] G. Liu, G. J. Zhang, F. Jiang, X. D. Ding, Y. J. Sun, J. Sun, E. Ma, Nanostructured high-strength molybdenum alloys with unprecedented tensile ductility, Nat. Mater. 12 (2013) 344-50. https://doi.org/10.1038/NMAT3544.

[26] J. L. Fan, X. Gong, B. Y. Huang, M. Song, T. Liu, M. G. Qi, J. M. Tian, S. K. Li, Dynamic failure and adiabatic shearbands in fine-grain 93W-4.9Ni-2.1Fe alloy with Y_2O_3 addition under lower high-strain-rate (HSR) compression, Mech. Mater. 42 (2010) 24-30. https://doi.org/10.1016/j.mechmat.2009.08.006.

[27] F. N. Xiao, T. Barriere, G. Cheng, S. Z. Wei, S. W. Zuo, L. J. Xu, Research on preparation process for the in situ nanosized Zr(Y)O_2 particles dispersion-strengthened tungsten alloy through synthesizing doped hexagonal $(NH_4)_{0.33}$·WO_3. J. Alloys Compd. 843 (2020) 156059. https://doi.org/10.1016/j.jallcom.2020.156059.

[28] U. R. Kiran, A. Panchal, M. Sankaranarayana, G. V. S. Nageswara, T. K. Nandy, Effect of alloying addition and microstructural parameters on mechanical properties of 93% tungsten heavy alloys, Mater. Sci. Eng. A. 640 (2015) 82-90. https://doi.org/10.1016/j.msea.2015.05.046.

[29] S. Cao, H. Chen, Nanorods assembled hierarchical urchin-like WO_3 nanostructures: Hydrothermal synthesis, characterization, and their gas sensing properties, J. Alloys Compd. 702 (2017) 644-648. https://doi.org/10.1016/j.jallcom.2017.01.232.

[30] L. Z. Li, J. Z. Zhao, Y. Wang, Y. L. Li, D. C. Ma, Y. Zhao, S. N. Hou, X. L. Hao, Oxalic acid mediated synthesis of WO_3-H_2O nanoplates and self-assembled nanoflowers under mild conditions, J. Solid. State. Chem. 184 (2011) 1661-1665. https://doi.org/10.1016/j.jssc.2011.05.008.

[31] M. Q. Xu, W. Zeng, F. Yang, L. Chen, Controllability of assemblage from WO_3-H_2O nanoplates to nanoflowers with the assistance of oxalic acid, J. Mater. Sci-Mater. El. 26 (2015) 6676-6682. https://doi.org/10.1016/j.jssc.2011.05.008.

[32] B. Miao, W. Zen, S. H. Hussain, Q. P. Mei, S. B. Xu, H. Zhang, Y. Q. Li, T. M. Li, Large scale hydrothermal synthesis of monodisperse hexagonal WO_3 Nanowire and the growth mechanism, Mater. Lett. 147 (2015) 12-15. https://doi.org/10.1016/j.matlet.2015.02.020.

[33] L. Zhang, X. C. Tang, Z. G. Lu, Z. M. Wang, Facile synthesis and photocatalytic activity of hierarchical WO3 core-shell microspheres, Appl. Surf. Sci. 258 (2011) 1719-1724. https://doi.org/10.1016/j.apsusc.2011.10.022.

[34] J. H. Ha, P. Muralidharan, D. K. Kim, Hydrothermal synthesis and characterization of self-assembled h-WO_3 nanowires/nanorods using EDTA salts, J. Alloys Compd. 475 (2009) 446-451. https://doi.org/10.1016/j.jallcom.2008.07.048.

[35] C. Wang, L. Zhang, S. Wei, K. M. Pan, M. Aindow, Y. P. Yang, Microstructure and preparation of an ultra-fine-grained W-Al_2O_3 composite via hydrothermal synthesis and spark plasma sintering, Int. J. Refract. Met. Hard Mater. 72 (2018) 149-156. https://doi.org/10.1016/j.ijrmhm.2017.12.022.

[36] C. J. Wang, L. Q. Zhang, S. Z. Wei, K. M. Pan, X. C. Wu, Q. K. Li, Effect of ZrO_2 content on microstructure and mechanical properties of W alloys fabricated by spark plasma sintering, Int. J. Refract. Met. Hard Mater. 79 (2019) 79-89. https://doi.org/10.1016/j.ijrmhm.2018.11.006.

[37] Z. Li, L. J. Xu, S. Z. Wei, C. Chen, F. N. Xiao, Fabrication and mechanical properties of tungsten alloys reinforced with c-ZrO_2 particles, J. Alloys Compd. 769 (2018) 694-705. https://doi.org/10.1016/j.ijrmhm.2018.11.006.

[38] Y. Shen, Z. Xu, K. Cui, J. Yu, Microstructure of a commercial W-1% La_2O_3 alloy, J. Nucl. Mater. 455 (2014) 234-241. https://doi.org/10.1016/j.jnucmat.2014.06.004.

[39] M. A. Yar, S. Wahlberg, H. Bergqvist, H. G. Salem, M. Johnsson, M. Muhammed, Chemically produced nanostructured ODS-lanthanum oxide-tungsten composites sintered by spark plasma, J. Nucl. Mater. 408 (2011) 129-135. https://doi.org/10.1016/j.jnucmat.2010.10.060.

[40] M. A. Yar, S. Wahlberg, H. Bergqvist, H. G. Salem, M. Johnsson, M. Muhammed, Spark plasma sintering of tungsten-yttrium oxide composites from chemically synthesised nanopowders and microstructural characterization, J. Nucl. Mater. 412 (2011) 227-232. https://doi.org/10.1016/j.jnucmat.2011.03.007.

[41] A. Muñoz, M. A. Monge, B. Savoini, M. E. Rabanal, G. Garces, R. Pareja, La_2O_3-reinforced W and W-V alloys produced by hot isostatic pressing, J. Nucl. Mater. 417 (2011) 508-511. https://doi.org/10.1016/j.jnucmat.2011.01.077.

[42] R. Liu, Z. M. Xie, T. Zhang, Q. F. Fang, X. P. Wang, T. Hao, C. S . Liu, Y. Dai, Mechanical properties and microstructures of W-1%Y_2O_3 microalloyed with Zr, Mater. Sci. Eng. A. 660 (2016) 19-23. https://doi.org/10.1016/j.msea.2016.02.072.

[43] Y. M. Ki, K. H. Lee, E. P. Kim, D. I. Cheong, S. H. Hong, Fabrication of high temperature oxides dispersion strengthened tungsten composites by spark plasma sintering process, Int. J. Refract. Met. Hard Mater. 27 (2009) 842-846. https://doi.org/10.1016/j.ijrmhm.2009.03.003.

[44] C. L. Chen, Sutrisna, The Effect of Mo and Dispersoids on Microstructure, Sintering Behavior, and Mechanical Properties of W-Mo-Ni-Fe-Co Heavy Tungsten Alloys, Metals. 9 (2019) 111. https://doi.org/10.3390/met9020111.

[45] O. Dinçer, M. K. Pehlivanoğlu, N. K. Çalişkan, I. Karakaya, A. Kalkanli, Processing and microstructural characterization of liquid phase sintered tungsten-nickel-cobalt heavy alloys, Int. J. Refract. Met. Hard Mater. 50 (2015) 106-112. https://doi.org/10.1016/j.ijrmhm.2014.12.009.

[46] G. Prabhu, N. A. Kumar, M. Sankaranarayana, T. K. Nandy, Tensile and impact properties of microwave sintered tungsten heavy alloys, Mater. Sci. Eng. A. 60 (2014) 63-70. https://doi.org/10.1016/j.msea.2014.03.130.

[47] L. J. Xu, F. N. Xiao, S. Z. Wei, Y. C. Zhou, K. M. Pan, X. Q. Li, W. Liu, Development of tungsten heavy alloy reinforced by cubic zirconia through liquid-liquid doping and mechanical alloying methods, Int. J. Refract. Met. Hard Mater. 78 (2019) 1-8. https://doi.org/10.1016/j.ijrmhm.2018.08.009.

[48] Z. S. Fan, D. P. Xiang, Y. L. Pan, H. Jiang, Effect of two-time spark plasma sintering on microstructure and mechanical properties of W-6Ni-4Mn alloy, Mater. Sci. Eng. A. 745 (2019) 300-306. https://doi.org/10.1016/j.msea.2018.12.109.

[49] G. Liu, G. J. Zhang, F. Jiang, X. D. Ding, Y. J. Sun, J. Sun, E. Ma, Nanostructured high-strength molybdenum alloys with unprecedented tensile ductility, Nat. Mater. 12 (2013) 344-50. https://doi.org/10.1038/NMAT3544.

[50] W. M. R. Daoush, A. H. A. Elsayed, O. A. G. E. Kady, O. A. G. Sayed, M. A. Dawood, Enhancement of physical and mechanical properties of oxide dispersion-strengthened tungsten heavy alloys, Mater. Sci. Eng. A. 47 (2016) 2387-2395. https://doi.org/10.1007/s11661-016-3360-7.

[51] K. H. Lee, S. I. Cha, H. J. Ryu, M. F. Dilmore, S. H. Hong, Effect of mechanical alloying process on microstructure and mechanical properties of ODS tungsten heavy alloys, J. Alloys Compd. 434 (2007) 433-436. https://doi.org/10.1016/j.jallcom.2006.08.284.

[52] K. Hu, X. Li, X. Ai, S. Qu, Y. Li, Fabrication, characterization, and mechanical properties of 93W-4.9Ni-2.1Fe/95W-2.8Ni-1.2Fe-1Al_2O_3 heavy alloy composites,

Mater. Sci. Eng. A. 636 (2015) 452-458. https://doi.org/10.1016/j.msea.2015.04.026.

[53] G. Lee, J. McKittrick, E. Ivanov, E. A. Olevsky, Densification mechanism and mechanical properties of tungsten powder consolidated by spark plasma sintering, Int. J. Refract. Met. Hard Mater. 61 (2016) 22-29. https://doi.org/10.1016/j.ijrmhm.2016.07.023.

[54] F. N. Xiao, L. J. Xu, Y. C. Zhou, K. M. Pan, J. W. Li, W. Liu, S. Z. Wei, A hybrid microstructure design strategy achieving W-ZrO_2(Y) alloy with high compressive strength and critical failure strain, J. Alloys Compd. 708 (2017) 202-212. https://doi.org/10.1016/j.jallcom.2017.02.277.

[55] Z. M. Xie, R. Liu, T. Zhang, Q. F. Fang, C. S. Liu, X. Liu, G. N. Luo, Achieving high strength/ductility in bulk W-Zr-Y_2O_3 alloy plate with hybrid microstructure, Mater. Des. 107 (2016) 144-52. https://doi.org/10.1016/j.matdes.2016.06.012.

[56] F. N. Xiao, Q. Miao, S. Z. Wei, T. Barriere, G. Cheng, S. W. Zuo, L. J. Xu, Uniform nanosized oxide particles dispersion strengthened tungsten alloy fabricated involving hydrothermal method and hot isostatic pressing, J. Alloys Compd. 824 (2020) 153894. https://doi.org/10.1016/j.jallcom.2020.153894.

[57] A. Bock, W. D. Schbert, B. Lux, Inhibition of grain growth on submicron cemented carbides, Int. Powder Metal. 24 (1992) 20. EDB-92-078461.

[58] S. J. L. Kang, W. A. Kaysser, G. Petzow, D. N. Yoon, Elimination of pores during liquid phase sintering of Mo-Ni, Int. Powder Metal. 27 (1984) 97-100. https://doi.org/10.1179/pom.1984.27.2.97.

[59] S. Annavarapu, R. D. Doherty, Inhibited coarsening of solid-liquid microstructures in spray casting at high volume fractions of solid, Acta. Metall. Sin. 43 (1995) 3207-3230. https://doi.org/10.1016/0956-7151(94)00448-Q.

[60] Z. Li, L. J. Xu, S. Z. Wei, C. Chen, F. N. Xiao, Fabrication and mechanical properties of tungsten alloys reinforced with c-ZrO_2 particles, J. Alloys Compd. 769 (2018) 694-705. https://doi.org/10.1016/j.jallcom.2018.07.342.

[61] H. Zhang, L. Ge, M. Shi, P. Ren, Densification behavior, mechanical properties and thermal shock resistance of tungsten alloys fabricated at low temperature, Mater. Des. 58 (2014) 290-297. https://doi.org/10.1016/j.matdes.2014.01.023.

[62] U. R. Kiran, S. Venkat, B. Rishikesh, Effect of tungsten content on microstructure and mechanical properties of swaged tungsten heavy alloys, Mater. Sci. Eng. A. 582 (2013) 389-396. https://doi.org/10.1016/j.msea.2013.06.041.

[63] U. R. Kiran, A. Panchal, M. Sankaranarayana, B. Iyer, V. K. Sankaranarayana, T. K. Nandy, Effect of alloying addition and microstructural parameters on mechanical properties of 93% tungsten heavy alloys, Mater. Sci. Eng. A. 640 (2015) 82-90. https://doi.org/10.1016/j.msea.2015.05.046.

[64] M. Scapin, Mechanical characterization and modeling of the heavy tungsten alloy IT180, Int. J. Refract. Met. Hard Mater. 50 (2015) 258-268. https://doi.org/10.1016/j.ijrmhm.2015.01.018.

[65] J. Das, G. A. Rao, S. K. Pabi, Microstructure and mechanical properties of tungsten heavy alloys, Mater. Sci. Eng. A. 527 (2010) 7841-7847. https://doi.org/10.1016/j.msea.2010.08.071.

[66] U. R. Kiran, M. P. Kumar, M. Sankaranarayana, K. Singh, T. K. Nandy, High energy milling on tungsten powders, Int. J. Refract. Met. Hard Mater. 48 (2015) 74-81. https://doi.org/10.1016/j.ijrmhm.2014.06.025.

[67] J. L. Fan, B. Y. Huang, X. Qu, Z. Q. Zou,Thermal stability, grain growth and structure changes of mechanically alloyed W-Ni-Fe composite during annealing, Int. J. Refract. Hard Mater. 19 (2001) 73-79. https://doi.org/10.1016/S0263-4368(00)00046-9.

[68] S. C. Zhou, L. Wang, Y. J. Liang, Y. C. Zhu, R. Z. Jian, B. P. Wang, L. Wang, Y. F. Xue, F. C. Wang, H. N. Cai, Y. Ren, A strategy to achieve high-strength WNiFe composite-like alloys with low W content by laser melting deposition, Mater. Des. 190 (2020) 108554. https://doi.org/10.1016/j.matdes.2020.108554.

[69] J. Kappacher, A. Leitner, D. Kiener, H. Clemens, V. M. Kiener, Thermally activated deformation mechanisms and solid solution softening in W-Re alloys

investigated via high temperature nanoindentation, Mater. Des. 189 (2020) 108499. https://doi.org/10.1016/j.matdes.2020.108499.

[70] L. Huang, L. Jiang, T. D. Topping, C. Dai, X. Wang, R. Carpenter, C. Haines, J. M. Schoenung, In situ oxide dispersion strengthened tungsten alloys with high compressive strength and high strain-to-failure, Acta Mater. 122 (2017) 19-31. https://doi.org/10.1016/j.actamat.2016.09.034.

[71] N. Senthilnathan, A. Annamalai, G. Venkatachalam, Microstructure and mechanical properties of spark plasma sintered tungsten heavy alloys, Mater. Sci. Eng. A. 710 (2018) 66-73. https://doi.org/10.1016/j.msea.2017.10.080.

[72] X. Gong, J. Fan, F. Ding, Tensile mechanical properties and fracture behavior of tungsten heavy alloys at 25-1100 C, Mater. Sci. Eng. A. 646 (2015) 315-321. https://doi.org/10.1016/j.msea.2015.08.079.

[73] J. Das, G. A. Rao, S. K. Pabi, M. Sankaranarayana, T. K. Nandy, Thermo-mechanical processing, microstructure and tensile properties of a tungsten heavy alloy, Mater. Sci. Eng. A. 613 (2014) 48-59. https://doi.org/10.1016/j.msea.2014.06.072.

[74] U. R. Kiran, J. Kumar, V. Kumar, M. Sankaranarayana, G. V. S. N. Rao, T. K. Nandy, Effect of cyclic heat treatment and swaging on mechanical properties of the tungsten heavy alloys, Mater. Sci. Eng. A. 656 (2016) 256-265. https://doi.org/10.1016/j.msea.2016.01.024.

[75] T. D. Wen, Z. S. Liang, Y. Liang, Research on the preparation and shielding properties of W-Ni-Fe alloy material by liquid phase sintering, Int. Powder Metall. 61 (2018) 28-35. https://doi.org/10.1080/00325899.2017.1376791.

[76] Y. Shao, F. Guo, Y. Huan, D. Q. Jiang, J. S. Zhang, Y. Ren, L. S. Cui, Fabrication, microstructure and mechanical properties of WNiTi composites, J. Alloys Compd. 695 (2017) 1976-1983. https://doi.org/10.1080/00325899.2017.1376791.

[77] N. Senthilnathan, A. R. Annamalai, G. Venkatachalam, Sintering of tungsten and tungsten heavy alloys of W-Ni-Fe and W-Ni-Cu: a review, T. India. I. Metals. 70 (2017) 1161-1176. https://doi.org/10.1007/s12666-016-0936-2.

[78] M. E. Alam, G. R. Odette, On the remarkable fracture toughness of 90 to 97W-NiFe alloys revealing powerful new ductile phase toughening mechanisms, Acta Mater. 186 (2020) 324-340. https://doi.org/10.1016/j.actamat.2020.01.012.

[79] C. Sun, S. Wang, W. Guo, W. Shen, C. Ge, Bonding interface of W–CuCrZr explosively welded composite plates for plasma facing components, J. Mater. Process. Technol. 12 (2014) 1230-1234. https://doi.org/10.1016/j.jmst.2014.11.014.

[80] F. Xiao, L. Xu, Y. Zhou, K. Pan, J. Li, W. Liu, S. Wei, Microstructure and mechanical properties of W-ZrO_2 alloys by different preparation techniques, J. Alloys Compd. 774 (2019) 210-221. https://doi.org/10.1016/j.jallcom.2018.09.321.

[81] K. Hu, X. Li, M. Guan, S. G. Qu, X. Y. Yang, J. X. Zhang, Dynamic deformation behavior of 93W-5.6 Ni-1.4 Fe heavy alloy prepared by spark plasma sintering, Int. J. Refract. Met. Hard Mater. 58 (2016) 117-124. https://doi.org/10.1016/j.ijrmhm.2016.04.010.

[82] Y. Yu, C. Ren, W. Zhang, Compressive behavior of liquid phase sintered 90W-7Ni-3Fe heavy alloy at high temperature and low strain rate condition, Int. J. Refract. Met. Hard Mater. 76 (2018) 149-157. https://doi.org/10.1016/j.ijrmhm.2018.06.006.

Graphical abstract

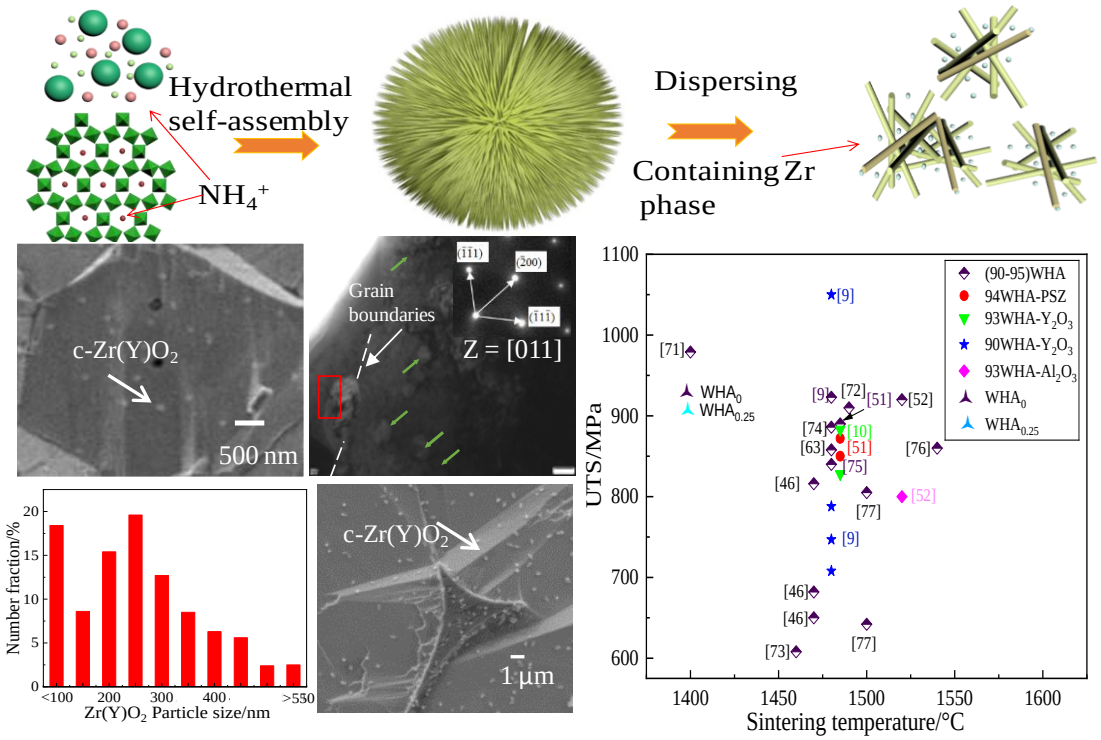

Highlights

1. Highly uniform nanosized $Zr(Y)O_2$ particles were fabricated by liquid doping.
2. W alloys were fabricated by a combined hydrothermal and mechanical alloying method.
3. $Zr(Y)O_2$ particles (< 200 nm), are much smaller than those reported in literature.
4. W alloys containing nanosized $Zr(Y)O_2$ exhibited excellent mechanical properties.

Author Contribution Statement

Fangnao Xiao and Qiang Miao: methodology, analysis and writing-original draft preparation;

Shizhong Wei, Liujie Xu and Shiwei Zuo: experiments and analysis;

Thierry Barriere and Gang Cheng: analysis and writing-editing.

Declaration of interests

The authors declare that they have no known competing financial interests or personal relationships that could have appeared to influence the work reported in this paper.

Extremely uniform nanosized oxide particles dispersion strengthened tungsten alloy with high tensile and compressive strengths fabricated involving liquid-liquid method

Fangnao Xiao [a, b], Thierry Barriere [b], Gang Cheng [c], Qiang Miao [a*], Shiwei Zuo [a], Shizhong Wei [d]*, Liujie Xu [d*]

[a] College of Material Science and Technology, Nanjing University of Aeronautics and Astronautics, 29 Yudao Street, Nanjing 210000, China

[b] Université Bourgogne Franche-Comté, FEMTO-ST Institute, CNRS/UFC/ENSMM/UTBM, Department of Applied Mechanics, 25000 Besançon, France

[c] INSA CVL, Université Tours, Université Orléans, LaMé, 3 rue de la Chocolaterie, BP 3410, 41034 Blois Cedex, France

[d] National Joint Engineering Research Center for abrasion control and molding of metal materials, Henan University of Science and Technology, Luoyang 471003, China

E-mail addresses of Corresponding author:

miaoqiang@nuaa.edu.cn (Qiang Miao)

wsz@haust.edu.cn (Shizhong Wei)

xlj@haust.edu.cn (Liujie Xu)

Full postal address:

FEMTO-ST Institute, Department of Applied Mechanics, 24 chemin de l'épitaphe, 25000, Besançon, France

Tel.: +33381666000

Abstract

In this study, tungsten heavy alloys reinforced with highly uniform and dispersed nanosized $Zr(Y)O_2$ particles were investigated. These alloys exhibited a high compressive strength and enhanced plasticity. To fabricate these alloys, we used a novel process involving molecular level liquid-liquid doping combined with hot isostatic pressing. The $Zr(Y)O_2$ particles thus produced were smaller than 200 nm in size and bonded well with tungsten grains. The size of $Zr(Y)O_2$ particles and tungsten grains are much smaller than those of the state-of-the-art review and the details of the grain refinement mechanisms were discussed. The effect of $Zr(Y)O_2$ particles and strain rate on the compressive properties of the alloys was investigated in detail and the corresponding compressive deformation mechanisms were elucidated. The highest ultimate tensile and compressive strengths of the fabricated alloys at room temperature (27°C) were 906 and 1445 MPa, respectively, which are higher than most of reported values in the literature. The ultimate tensile strength and fracture strain of WHAs decrease with the mass fraction of $Zr(Y)O_2$ (from 0 to 0.75%). The alloys exhibit the brittle material behaviour in tension, compared to the pure tungsten with ductile material behaviour. The tensile fracture surface consists of W - W cleavage patterns and ductile failure of the matrix. The results obtained in this research will act as basic guidelines for the fabrication of ODS-W alloys by liquid-liquid doping process.

Keywords: Tungsten heavy alloys; oxide particle strengthening; zirconia; liquid-liquid doping; compressive strength; hot isostatic pressing

Nomenclature

α-HATB	Hexagonal ammonium tungsten bronze $(NH_4)_{0.33}\cdot WO_3$
β-HATB	Hexagonal ammonium tungsten bronze $(NH_4)_{0.42}\cdot WO_3$
AMT	Ammonium metatungstate
APT	Ammonium paratungstate
DUAs	Depleted uranium alloys

EDS	Energy dispersive X-ray spectroscopy
HATB	Hexagonal ammonium tungsten bronze, $(NH_4)_x \cdot WO_3$
HIP	Hot isostatic pressing
HR-TEM	High-resolution transmission electron microscopy
HV	Vickers hardness
L-L	Liquid-liquid
L-S	Liquid-solid
MA	Mechanical alloying
ODS-W	Oxide particle dispersion-strengthened tungsten
ODS-WHAs	Oxide particle dispersion-strengthened tungsten heavy alloys
PSZ	Partially stabilised zirconia
RD	Relative densities
SAED	Selected area electron diffraction
SEM	Scanning electron microscopy
SPS	Spark plasma sintering
S-S	Solid-solid
UTS	Ultimate tensile strength
VD	Sintering process in the vertical direction
WHAs	Tungsten heavy alloys
WHA-Zr(Y)O_2	Zr(Y)O_2 particle dispersion-strengthened 93W-4.9Ni-2.1Fe alloy
W-M	Tungsten-matrix
W-W	Tungsten-tungsten
XRD	X-ray diffraction

1. Introduction

Tungsten heavy alloys (WHAs) are promising materials for kinetic energy penetrators, radiation shields, and rocket nozzles, owing to their moderate ductility, high density, and quasi-static strength [1-4]. In particular, WHAs are more suitable for use in kinetic energy penetrators than depleted uranium alloys (DUAs) as they pose no risk of radioactive contamination [5]. Furthermore, they exhibit a lower penetration performance (by ~20%) than DUAs at high strain rates [6,7].

Generally, the penetration capability of WHAs depends on their strength and toughness [8]. The existing WHAs obtained using conventional powder metallurgy are limited to anti-armour penetrators owing to the weak mechanical properties of coarse tungsten grains [9]. In recent years, a large number of researchers have focused on improving the mechanical performance of WHA penetrators by inducing microstructural changes [10-12] via changing the WHA composition by adding alloying elements or rare earth oxides (Y_2O_3, La_2O_3, ZrO_2, ThO_2, and CeO_2) [13-16] or by microstructural refinement [17-20].

Grain refinement in tungsten is known to significantly enhance its mechanical properties. However, the grain size of WHAs depends partially on the particle size of the initial powders. In the past few years, liquid-liquid (L-L) doping techniques have been developed for oxide particle-doped tungsten powders. Xu et al. fabricated La_2O_3-doped ultra-fine tungsten powders using $Na_2WO_4{\cdot}2H_2O$ and $La(NO_3)_3{\cdot}6H_2O$ as the raw materials [21]. Nanosized La_2O_3-doped tungsten powders with a particle size of ~700 nm were realised by hydrogen reduction. Dong et al. synthesised Y_2O_3-doped nanosized tungsten powders with an average particle size of 40–50 nm via a wet-chemical process [22]. Xiao et al. used the hydrothermal method coupled with hydrogen reduction to develop nanocrystal powders of W-Zr(Y)O_2 with an average particle size of 30 nm [23]; these oxides were used as nucleation cores in tungsten for particle refinement. Rare earth elements (such as Y, Zr and La) decrease the number of O and P impurities aggregating at the interface and thus improve the performance of WHA penetrators [24]. In addition, nanosized oxide particles can lead to dispersion strengthening and grain refinement, thus increasing the strength and

ductility of the alloys fabricated by L-L doping [25,26]. Therefore, L-L doping with nanosized oxide particles is considered to be an effective approach for improving the mechanical performance of WHAs.

In this study, a novel material based on dispersion-strengthened 93W-4.9Ni-2.1Fe alloys [WHA-Zr(Y)O_2] using nanosized Zr(Y)O_2 is proposed. WHA-Zr(Y)O_2 was prepared by a hydrothermal method combined with mechanical alloying (MA). Nanosized Zr(Y)O_2 dispersion-strengthened WHAs were fabricated by conventional solid-phase sintering and hot isostatic pressing (HIP). The uniaxial tensile and compressive properties of WHA-Zr(Y)O_2 were estimated and the effect of Zr(Y)O_2 on the microstructure and mechanical properties of the WHAs were investigated. These microstructural characteristics and mechanical properties (tensile and compressive) of the present WHA-Zr(Y)O_2 alloys under various solicitations were compared with those of the state-of-the-art WHA materials to demonstrate the effectiveness of the proposed method. It indicates that the fabricated alloys exhibit smaller size of tungsten grains and oxide particles, and higher ultimate tensile and compressive strengths.

This article is structured as follows. In Section 2, the sample preparation and characterisation processes are described in detail. In Section 3, our observations on powder morphology, WHA microstructure, and the mechanical properties of WHA-Zr(Y)O_2 alloys are described with reference to the relevant literature. Finally, our major conclusions are presented in Section 4.

2. Experimental procedure

2.1 Sample preparation

In the present work, four W-Zr(Y)O_2 powders were prepared using the process shown in Fig. 1. The composition of the alloy powders contained varying amounts of Zr(Y)O_2 (0, 0.25, 0.5, and 0.75 wt.% denoted as WHA_0, $WHA_{0.25}$, $WHA_{0.50}$ and $WHA_{0.75}$, respectively, as listed in Table 1). The commercial raw materials included zirconium oxychloride octahydrate ($ZrOCl_2 \cdot 8H_2O$; grade AR), yttrium nitrate [$Y(NO_3)_3 \cdot 6H_2O$; grade AR] and ammonium metatungstate [$(NH_4)_6H_2W_{12}O_{40} \cdot 5H_2O$;

grade AR; AMT]. The supplier of $ZrOCl_2 \cdot 8H_2O$ and $Y(NO_3)_3 \cdot 6H_2O$ powders was Shanghai Diyang Industrial Co., LTD. The AMT powder was provided by Wuhan Kabuda Chemical Co., LTD. The synthesis and reduction of W-Zr(Y)O_2 powders were carried out according to previously described protocols [27]. After hydrothermal treatment, the precursor consisted of hexagonal $(NH_4)_{0.33} \cdot WO_3 \cdot$(α-hexagonal ammonium tungsten bronze, α-HATB, PDF# 42-0452), as shown in Fig. 2a). The reduction process included the following stages – a first reduction step at 500 °C for 1.5 h resulting in hexagonal $(NH_4)_{0.42}WO_3$ (β-HATB, PDF#42-0451), which is expected to produce high-quality doped tungsten powders and alloys [27], and a second reduction reaction at 800 °C for 2 h to yield W-Zr(Y)O_2 powder. After hydrogen reduction, the $(NH_4)_{0.42}WO_3$ was transformed into α-W.

W-Zr(Y)O_2 alloys were fabricated by Hot isostatic pressing (HIP) at 2000 °C for 5 min at 30 MPa. MA was conducted to blend elemental Ni, Fe, and W-Zr(Y)O_2 powders at the appropriate proportions. A planetary ball mill was used at a milling speed of 250 rpm for 6 h. The milling media consisted of 3 mm diameter tungsten carbide balls with ball-to-powder ratio of 10:1. The milled powders were compacted into cylindrical rods by cold isostatic pressing at 250 MPa. Subsequently, the green compacts were sintered at 1250 °C for 1 h in a hydrogen atmosphere. These samples were later sintered by hot isostatic pressing at 1400 °C for 2 h at 180 MPa. Fig. 2b) shows the X-ray diffraction (XRD) pattern of $WHA_{0.75}$, which suggests the presence of W and γ(Fe, Ni) phases.

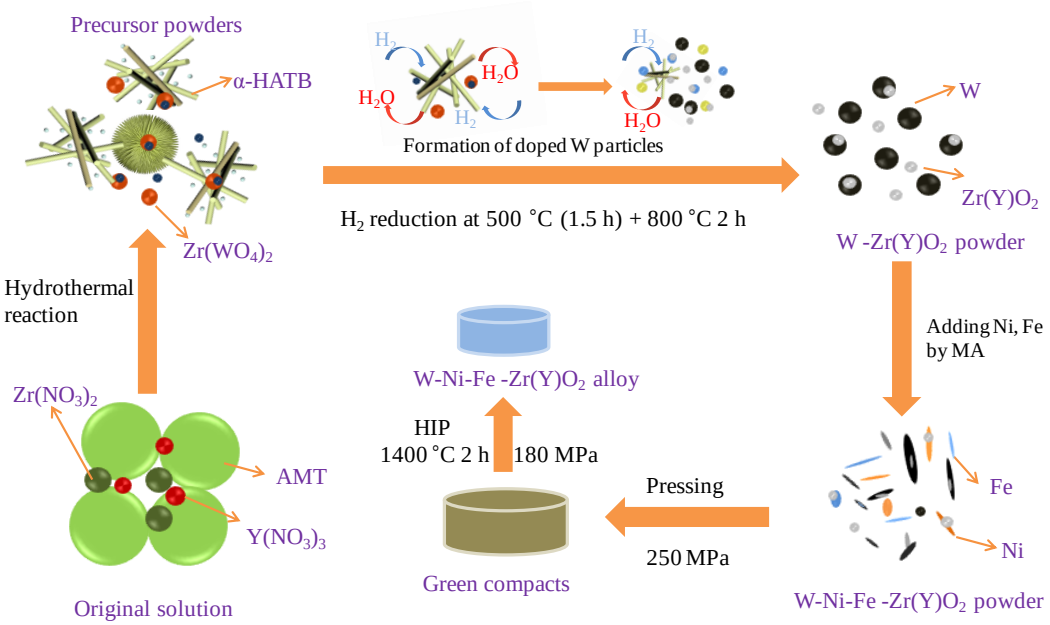

Fig. 1 Schematic diagram of the synthesis of WHAs

Table 1 Chemical composition of WHA-$Zr(Y)O_2$ alloys (wt.%)

Samples	W	Fe	Ni	ZrO_2	Y_2O_3
WHA_0	93.000	2.1	4.9	0.00	0.00
$WHA_{0.25}$	92.720	2.1	4.9	0.25	0.03
$WHA_{0.50}$	92.440	2.1	4.9	0.50	0.06
$WHA_{0.75}$	92.156	2.1	4.9	0.75	0.09

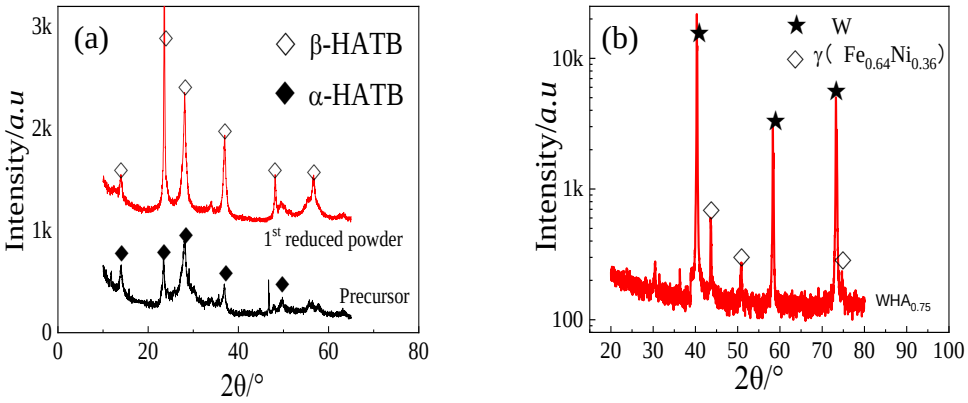

Fig. 2 XRD patterns of a) powder precursor and doped reduced powder and b) $WHA_{0.75}$

2.2 Measurement, experimental procedures, and analysis

The microstructure of the fabricated powders and alloys was evaluated by scanning electron microscopy (SEM), energy dispersive X-ray spectroscopy (EDS), and high-resolution transmission electron microscopy (HR-TEM). XRD analysis was conducted on the produced powders and alloys to identify their crystalline phases. The absolute densities of the alloys were determined using Archimedes' principle and theoretical densities were calculated based on the theoretical mass and volume. Relative density (RD) was calculated as the ratio of absolute and theoretical densities.

Vickers hardness (HV) testing was conducted with a 200 g indenting load and a dwell time of 20 s using the HVS-1000 digital micro Vickers hardness tester. The obtained value represented the average of values sourced from ten random positions on the alloy cross-section. Grain-size data was acquired using a line intercept method and at least 100 identifiable grains were considered for this measurement. Tungsten-tungsten (W-W) contiguity (C_{WW}), which is defined as the relative fraction of the W-W interfacial area, was estimated according to Eq. (1) [28],

$$C_{WW} = 2N_{WW}/(N_{WW} + N_{WM}) \quad (1)$$

where N_{WW} and N_{WM} indicate the number of W-W grain boundaries and tungsten-matrix (W-M) interfaces intercepted by an arbitrary straight line per unit length in the SEM images, respectively.

Tensile properties were measured on a universal testing machine (Instron-5967) at a constant loading rate of 0.3 mm/min at room temperature (27 °C). The average of three measured values is reported as the tensile strength of a given sample; specimen dimension is shown in Fig. 3.

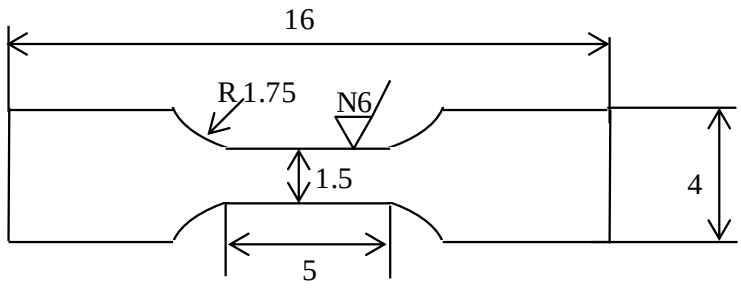

Fig. 3 Dimension of tensile testing specimens (all units are in mm)

The compressive properties of the samples were measured on a universal material machine (Shimadzu AG-I250kN) at strain rates of 10^{-3}, 10^{-2}, 10^{-1}, and 1 s^{-1}. Cylindrical samples with a diameter and length of 6 and 10 mm, respectively, were used for this purpose.

3. Results and discussions

3.1 Precursor morphology and $Zr(Y)O_2$ particle size and distribution

The morphology of the precursors synthesised using the hydrothermal method is illustrated in Fig. 4. The precursor consisted of nanoplates, with a diameter of less than 20 nm and length of ~100 nm, as shown in Fig. 4a). The lattice fringe image indicated a spacing of 0.384 nm, corresponding to the (002) plane of hexagonal $(NH_4)_{0.33}WO_3 \cdot H_2O$ and this indicates the growth of nanoplates along the *c* axis [29].

Primary crystals ($WO_3 \cdot nH_2O$) precipitated from the crystal cell were initially formed by the hydrothermal reaction (Eq. (2)) between $(H_2W_{12}O_{40})^{6-}$ and H^+ [23]. Tungsten atoms in $WO_3 \cdot nH_2O$ are bound to six oxygen atoms in a regular octahedral coordination pattern, as shown in Fig. 4d). Each oxygen atom is shared by two octahedrons, which are arranged in layers to form six-membered rings and then form numerous hexagonal and trigonal tunnels by sharing equatorial oxygen in the ab plane (001) [30-32]. These rings are usually stacked by sharing oxygen along the *c* axis [001] and form hexagonal prisms. At the same time, due to their high concentration, NH_4^+ ions in the hydrothermal system occupied the hexagonal tunnels [33,34], thus accelerating the growth of hexagonal-prism-like WO_3 in the [001] direction and the formation of hierarchical $(NH_4)_{0.33}WO_3 \cdot H_2O$ nanoplates. The presence of NH_4^+ and H^+ can contribute to the formation of urchin-like h-WO_3 microspheres, as shown in Fig. 4b). During the hydrothermal reaction, numerous tiny WO_3 crystals nucleate and grow into WO_3 nanoplates due to the orientation effect of NH_4^+; these crystals self-assemble to form microspheres to reduce surface energy. The high concentration of NH_4^+ around WO_3 microspheres accelerates the oriented growth of WO_3. Thus, numerous nanoplates grow epitaxially from the surface of a microsphere. This may be due to the addition of ions (Zr^{4+}, Y^{3+}, and Cl^-) to the hydrothermal system and

breakage of order between the positive and negative charges destroying the self-assembly process, which leads to the transformation of agglomerated microspheres into relatively disperse cotton-like precursors.

$$(NH_4)_6H_2W_{12}O_{40}\cdot xH_2O + 6HNO_3 = 6NH_4NO_3 + 12WO_3\cdot nH_2O + (8–x)H_2O \quad (2)$$

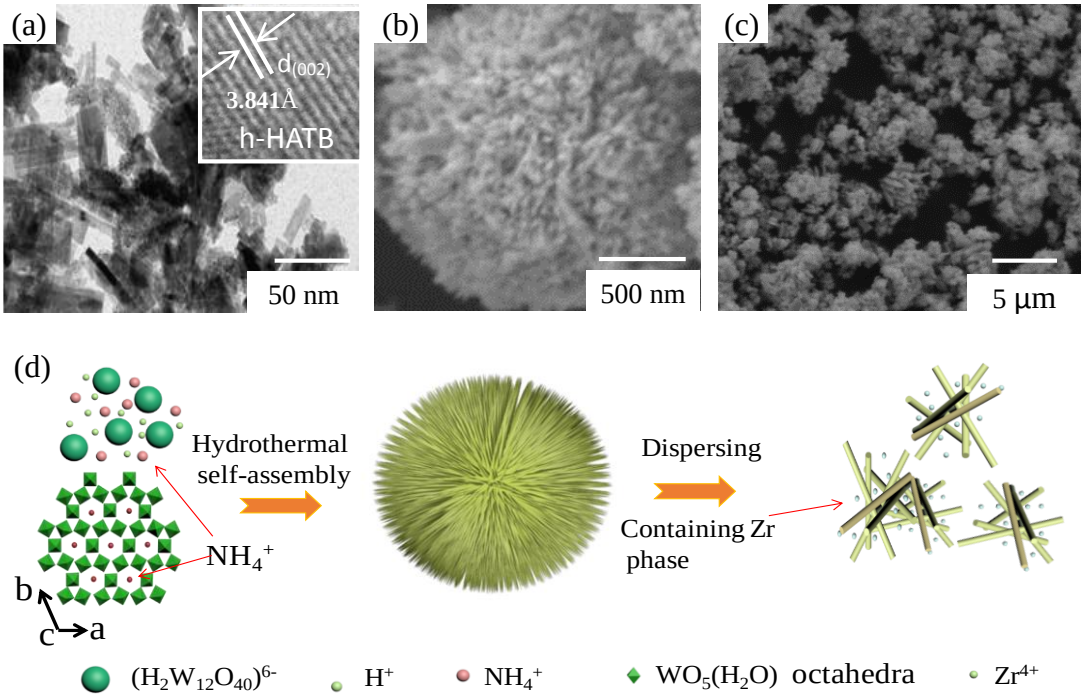

Fig. 4 Experimental observations and a schematic of α-HATB synthesis. a) TEM image of the undoped precursor, b) SEM image of the undoped precursor, c) SEM image of the doped precursor containing the (Zr, Y) phase, and d) illustration of morphology evolution in the $(NH_4)_{0.33}WO_3\cdot H_2O$ precursor

The size of oxide particles and their distribution in tungsten powders and alloys were studied (Fig. 5). A SEM image of the powder reduced at the optimised processing parameters is shown in Fig 5a). The powder particles exhibited small diameter and excellent dispersion, which is beneficial for increasing the uniformity and density of the microstructure during sintering. Further, nanoscale white particles, composed of $Zr(Y)O_2$, were scattered on the surfaces of tungsten particles, as shown

in Fig. 5a$_1$).

SPS was conducted to produce W-Zr(Y)O_2 alloys and investigate the effect of Zr(Y)O_2 particle size and distribution on the alloy microstructure, as shown in Fig. 5b). Oxide particle size was found to be uneven in the range of 100–500 nm. According to the magnified image of the selected area in Fig. 5b$_1$), a large number of white particles were found to be distributed within the grains, which helped in enhancing material properties. Moreover, a large number of nanoparticles (50 nm) were found to be distributed within the microstructure, as observed by TEM. A strong bonding was thus formed between the particles and tungsten phase even though there was no phase coherence between tungsten and the oxide, as shown in Fig. 5c$_1$).

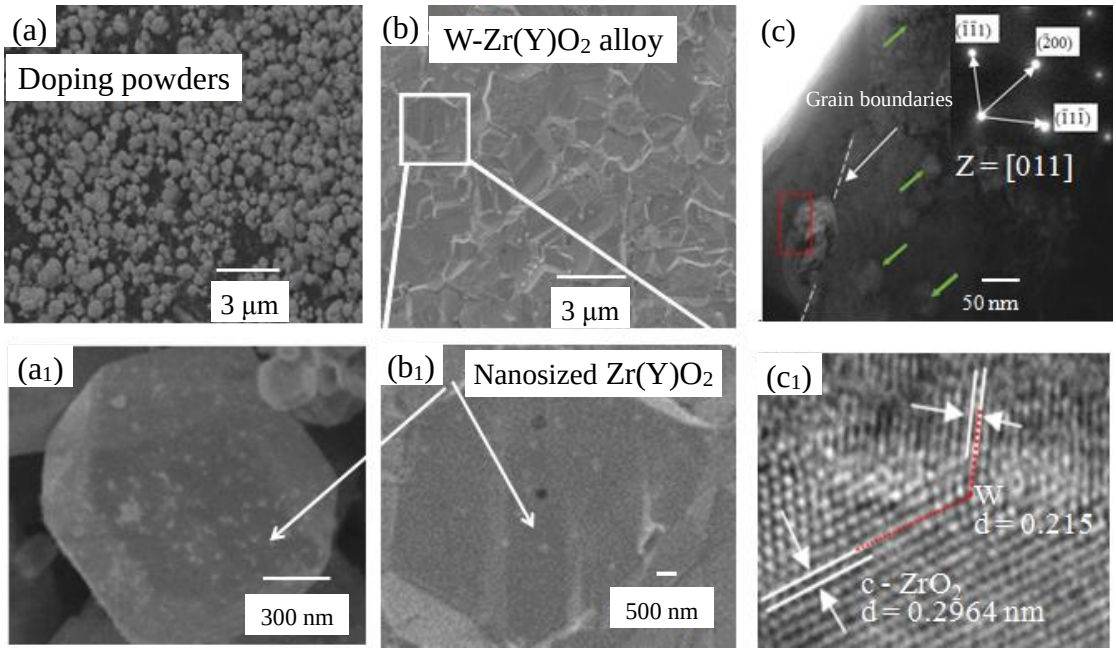

Fig. 5 Morphology and microstructure of W-Zr(Y)O_2 powders and alloys obtained using the proposed approach. a and a$_1$) SEM images of the morphology of the W-Zr(Y)O_2 powder. b and b$_1$) SEM images of the microstructure of the W-Zr(Y)O_2 alloy. c and c$_1$) TEM and HR-TEM images of the W-Zr(Y)O_2 alloy

The microstructure and mechanical properties of oxide particle dispersion-strengthened tungsten alloys (ODS-W) fabricated in this study were

compared with those reported earlier (alloys with the same or similar composition obtained by different processes as shown in Table 2). Fast sintering techniques, such as HIP, SPS, and sintering in vertical direction (VD), eliminate oxide particle growth. From Table 2, it may be inferred that L-L methods are better at yielding fine oxide particles in ODS-W alloys than L-S and S-S methods [35-37]. However, the size of these particles varied widely at 3.6, 1.5, and 2.5 μm. They were still much coarser than the oxide particles synthesised in tungsten alloys using the approach proposed in the current study. A similar observation could be made for ODS-W alloys fabricated by L-S methods. Yar et al. [40] prepared nanosized W-Y_2O_3 alloy by L-S doping. However, these Y_2O_3 particles were non-uniformly distributed in the tungsten matrix as the reaction occurred at the surfaces of the raw material alone (ammonium paratungstate, APT). Nanosized oxide particles were used as raw materials in S-S doping, but a large adsorption effect led to particle aggregation even after 30 h of ball milling [43]. In current research, the oxide particles obtained in tungsten alloys using the current approach were 0.8–10 times smaller when compared to those described in previous reports. This difference indicates that the proposed L-L doping process is appropriate to reduce particle size in tungsten alloys.

Table 2 Comparison of the microstructure and mechanical properties of ODS-W alloys

Doping process	**Sintering process**	**Alloy**	**W grain size (μm)**	**Oxide particle size (μm)**	**Density (g/cm^3)/Relative density (%)**	**Microhardness (HV)**	**Ref.**
L-L	SPS	W-6vol% Al_2O_3	3.64	>1.0	-/94.96	347.39	[35]
	SPS	W-2.5%ZrO_2	4.65	2.5	-/99.6	480	[36]
	VD	W-2.5%ZrO_2	40-80	1.5	-/98.7	-	[37]
L-S[a*]	VD	W-La_2O_3	50	3	-	-	[38]
	SPS	W-0.9wt.%La_2O_3	-	2	17.8/94	406	[39]
	SPS	W-1.0%Y_2O_3	2.3	Nanosize	17.5/92	423	[40]

				(Uneven)			
S-S	HIP	W-1%La_2O_3	-	>5	18.9/90.6	-	[41]
	SPS	W-0.5%Y_2O_3	2-5	>1.5	-	-	[42]
	SPS	W-5%HfO_2	11.6	>5	-/94.5	440	[43]
Current process	**SPS**	**W-0.5%Zr(Y)O_2**	**4.67 ± 0.5**	**0.25 ± 0.05**	**18.44/96.7 ± 0.2**	**472 ± 10**	**Present**

a* using APT as the tungsten source.

3.2 Microstructure of WHAs

The morphology of $WHA_{0.75}$ powder produced by MA of W-Zr(Y)O_2 powder with Ni and Fe powders is shown in Fig. 6a). It can be observed that the structure of the $WHA_{0.75}$ powder is much looser than that of W-Zr(Y)O_2 (Fig. 5a)). The microstructures of WHAs with different weight ratios of Zr(Y)O_2 are shown in Fig. 6(b–d). According to Fig. 6b), spherical tungsten grains are embedded in the matrix phase due to liquid-phase formation during sintering at 1400 °C [44]. It could be confirmed that the grain size of $WHA_{0.75}$ is smaller than that of WHA_0 after comparing the average size of 100 grains. W grains in alloys with and without Zr(Y)O_2 particles were uneven in size; the growth of W grains during liquid-phase sintering may be explained by Ostwald ripening [45]. In the current experimental conditions, smaller particles reprecipitated on larger tungsten grains during their dissolution in the matrix [46].

Moreover, grain contiguity reduced slightly as the grain size decreased, similar to previously reported results [47]. The reason for the decrease in W-W contiguity is that Zr(Y)O_2 particles induce the liquid phase $\gamma(Fe_{0.64}N_{0.36})$ to infiltrate W grain boundaries during sintering [48]. Thus, tungsten grains are gradually covered by the $\gamma(Fe_{0.64}N_{0.36})$ phase to enhance the mechanical properties of oxide particle dispersion-strengthened WHAs (ODS-WHAs).

A magnified image of the area enclosed in red in Fig. 6c) is presented in Fig. 6d) to understand the microstructure of $WHA_{0.75}$ in further detail. A large number of

white particles with similar particle size of less than 200 nm could be observed. These $Zr(Y)O_2$ particles were dispersed in W grains. Generally, large oxide particles induce stress/strain concentration for crack initiation and reduce the fracture toughness of an alloy [49]. Therefore, nanosized $Zr(Y)O_2$ particles (such as those in the present alloy) obtained by the proposed process are expected to enhance the mechanical properties of WHAs.

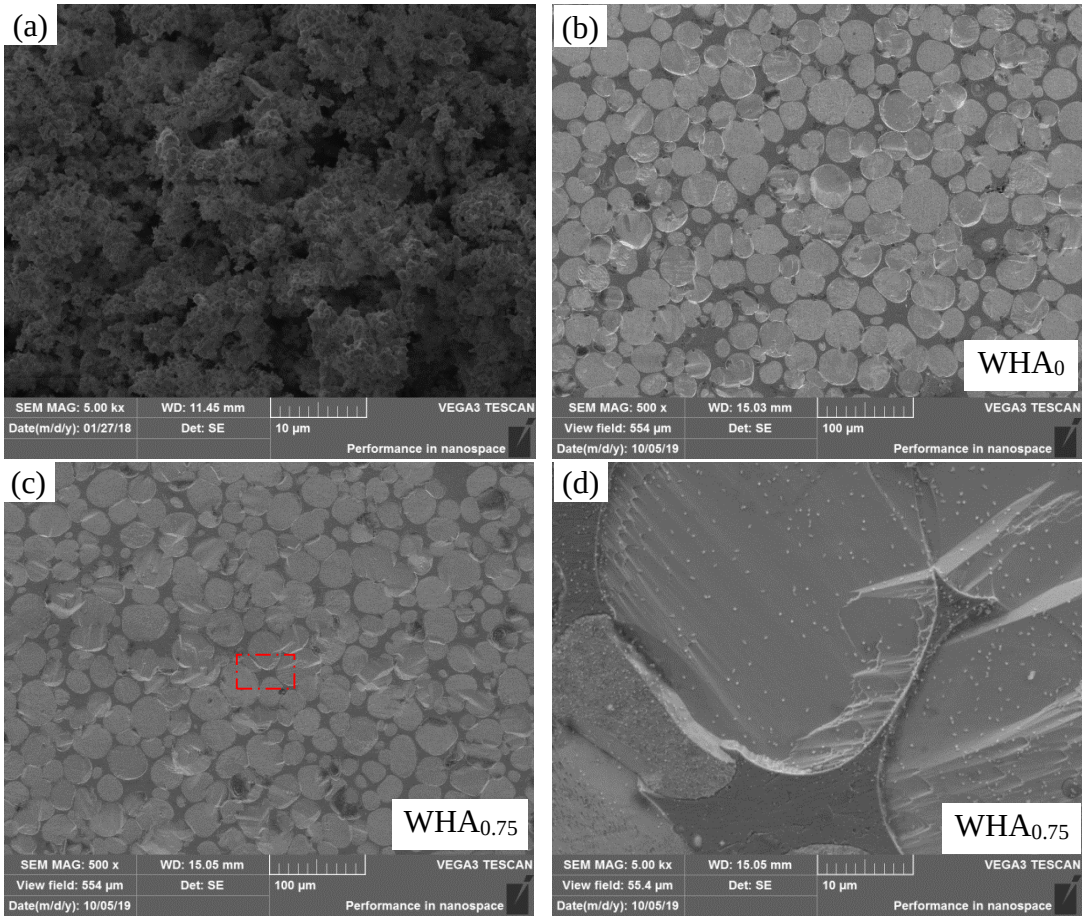

Fig. 6 SEM images of the microstructure of a) $WHA_{0.75}$, b) WHA_0, and c) and d) $WHA_{0.75}$ at 500x and 5000x, respectively

The microstructure of $WHA_{0.75}$ after quasi-static compressive loading at room temperature (27 °C) was characterized by TEM. As shown in Fig. 7a)–c), oxide nanoparticles with prismatic and subspherical structure exhibited different particle sizes. In Fig. 7a), it may be observed that the prismatic particles surrounded by a black phase were ~200 nm in size. In Fig. 7b) and c), it can be seen that subspherical particles smaller than 50 nm were embedded in shallow phases consisting of Ni, Fe,

and W, as described by EDS. White cubic nanocrystalline $Zr(Y)O_2$ particles were detected in the selected area electron diffraction (SAED) pattern in the inset of Fig. 7a). Dislocation substructures are marked by white arrows in the matrix phase, as shown in Fig. 7c). Meanwhile, Fig. 7d) illustrates a well-bonded interface between the tungsten phase and $Zr(Y)O_2$ even though there was no coherent relationship.

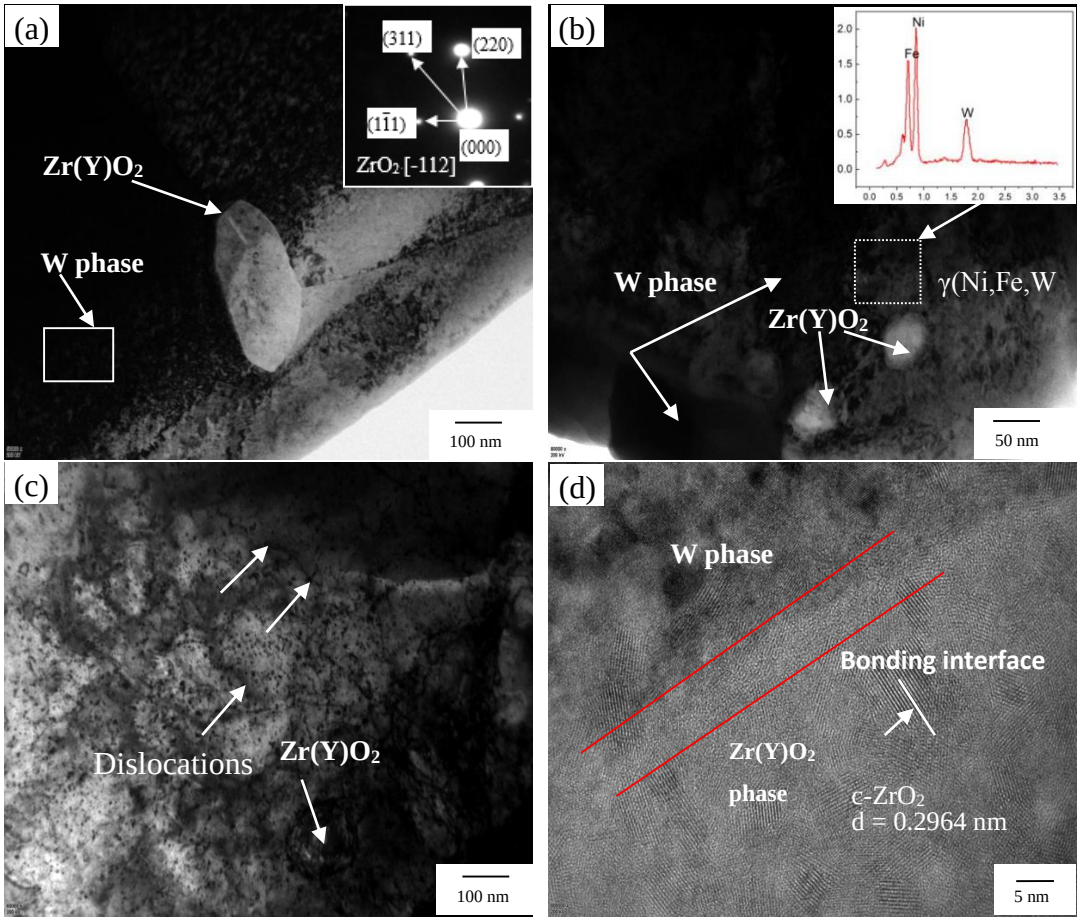

Fig. 7 a) and b) TEM images of $WHA_{0.75}$, c) TEM image of the matrix phase, and d) HRTEM image of the $Zr(Y)O_2$/W interface

The microstructures of several heavy tungsten alloys reinforced by ZrO_2 particles are shown in Fig. 8 and Table 3. Daoush et al. [49] fabricated W-Ni-ZrO_2 alloys by conventional sintering at 1500 °C for 1 h. The ZrO_2 particles in these alloys ranged from 0.5 to 3 μm in size, as shown in Fig. 8a), and they were almost at or close to the grain boundaries. Lee et al. [51] fabricated partially stabilised zirconia (PSZ) dispersion-strengthened WHAs by two-step MA to control the location of oxide

particles. However, the PSZ particles in the alloys still grew to be as large as 1.5 μm, as shown in Fig. 8b), and some adhesive oxide particles marked by red arrows could be observed. Xu et al. [47] studied $Zr(Y)O_2$ dispersion-strengthened 92.5W-4.9Ni-2.1Fe alloys using azeotropic distillation process. In these alloys, the $Zr(Y)O_2$ particles were 200–1000 nm large, as shown in Fig. 8c). Wang et al. [36] synthesised W-ZrO_2 alloys using a combination of the hydrothermal method and SPS. In this case, agglomerated precursors could be detected and the adhesive ZrO_2 particles grew to 3 μm, as shown in Fig. 8d). Larger oxide particles obtained by different powder preparation processes are observed in tungsten or heavy tungsten alloys, as summarised in Table 3. These oxide particles fabricated by the previous processes are larger than those through the developed process in the current research. Non-uniformly distributed coarse particles induce uneven stress and strain distribution around these reinforced particles, weakening the alloys. The proposed process is proved to be appropriate for the fabrication of the dispersion-strengthening tungsten alloys with ultrafine nanosized $Zr(Y)O_2$ particles.

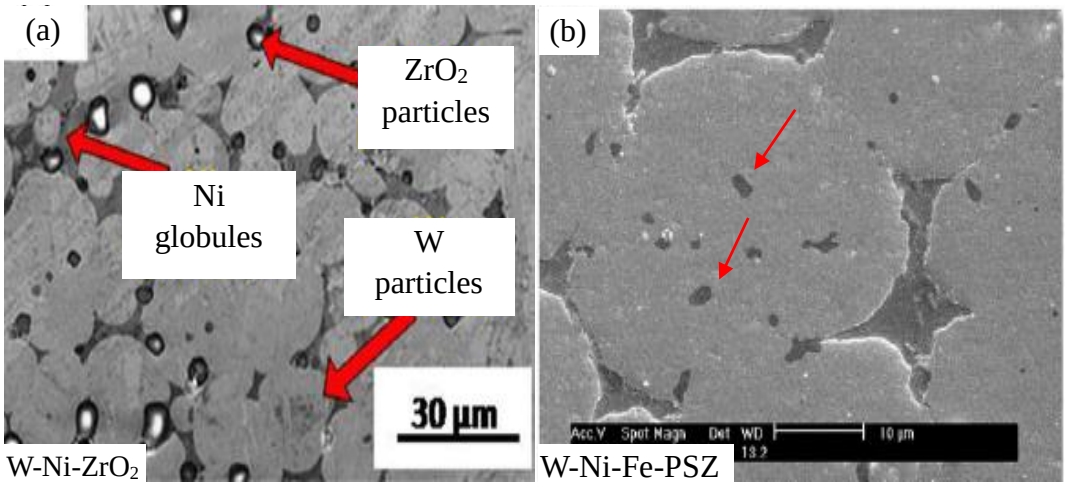

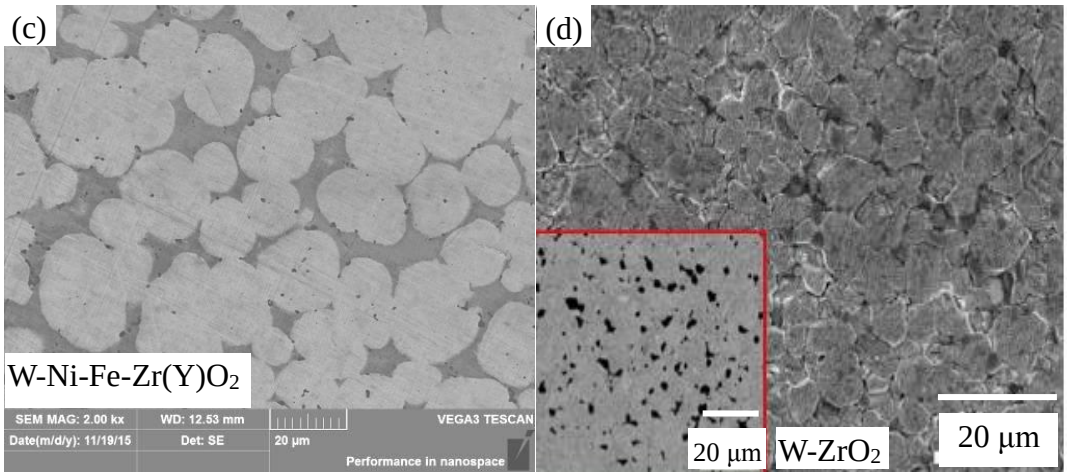

Fig. 8 Microstructures of WHAs reinforced by ZrO_2 particles. a) W-Ni-ZrO_2 [49], b) W-Ni-Fe-PSZ [51], c) W-Ni-Fe-ZrO_2 [47], and d) W-ZrO_2 [36]

Table 3 Microstructure and mechanical properties of ODS-WHA reported in the literature and in the current study

Heavy tungsten alloy	**Powder preparation process**	**Sintering process**	**RD (%)**	**Grain size (µm)**	**Particle size (µm)**	**Hardness (HV)**	**Ref.**
W-Ni-ZrO_2	MA	1500°C (1 h)	93.5	~25	3-5	333	[50]
W–Ni-Fe–0.3PSZ	MA	1480 °C (1 h)	-	18	0.8	-	[51]
93W-4.9Ni-2.1Fe-Zr(Y)O_2	L-L doping	1520 °C (2.5 h)	99.2	28	0.5-1	402	[47]
W-2.5%ZrO_2	L-L doping	1800 °C (5 min) by SPS	99.6	4.65	2.5	480	[36]
W-Ni-Fe-1Al_2O_3	Blending process	1480 °C (2 h)	98.3	36.8	7	-	[52]
W-Ni-Fe-xY_2O_3	MA	1850 °C (1 h)	99.1	19.5	0.6-1.3	-	[10]
W-Ni-Fe-Co-Y_2O_3	MA	1450 °C (1 h)	94.1	12	>0.6	425	[44]
94W-4.56Ni-1.14Fe-Y_2O_3	MA	1485 °C (1 h)	99.0	15	0.65	-	[53]
W-ODS alloys	- a*	SPS/HIP	<99.9	<10	1-5	406-480	[27]
$WHA_{0.75}$	**L-L doping**	**1400 °C (2.5 h)**	**99.5 ± 0.1**	**25 ± 2**	**0.25 ± 0.05**	**407 ± 10**	**Present**

a* These W-ODS powders were prepared by different doping processes, seeing Table 5 in references [27]

Intracrystalline heavy tungsten alloys reinforced with nanosized c-$Zr(Y)O_2$ particles were fabricated in this study; the consequent formation and distribution of c-$Zr(Y)O_2$ particles during L-L doping at the ionic level are shown in Fig. 9. The formation of nanosized yttria-stabilised cubic zirconia is attributed to the L-L incorporation of Zr^{4+} and Y^{3+} ions; $Y(NO_3)_3$ solution was added slowly to a $ZrOCl_2{\cdot}8H_2O$ solution while stirring to obtain a cluster solution [47]. Though $ZrOCl_2 \cdot 8H_2O$ dissolves in strong acid solutions, it undergoes hydrolysis in aqueous solutions and Cl^- ions in the outer sphere of the ionic complex are replaced by OH^- groups (Eq. (3)) [27]. Subsequently, $[Zr_4(OH)_8\ 16H_2O]^{8+}$ units react with the hydroxyl ions to form $Zr(OH)_4$ sols [27].

$$\{[Zr_4(OH)_8{\cdot}16H_2O]^{8+}8Cl^-\} + 4H_2O = \{[Zr_4(OH)_8{\cdot}16H_2O]^{8+}\ 8OH^-\} + 8HCl\uparrow \quad (3)$$

However, the generated $Zr(OH)_4$ easily decomposes in acidic conditions to yield Zr^{4+}. During the hydrothermal reaction, $W_{12}O_{40}^{8-}$ ions are introduced from the hydrolysis of AMT (Eq. (4)) [23] after which Zr^{4+} and Y^{3+} ions reacts with $W_{12}O_{40}^{8-}$ ions to produce $Zr(WO_4)_2$ and $Y_2(WO_4)_3$ (Eqs. (5) and (6)) [47,54]. Y_2O_3 penetrates oxygen vacancies in the zirconia lattice to form stabilized $Zr(Y)O_2$ during sintering [55].

$$(NH_4)_6H_2W_{12}O_{40} = 6NH_4^+ + 2H^+ + W_{12}O_{40}^{8-} \quad (4)$$

$$2Zr(OH)_4 + 8H^+ + W_{12}O_{40}^{8-} = 8WO_3\downarrow + 2Zr(WO_4)_2\downarrow + 8H_2O \quad (5)$$

$$2Y^{3+} + 2H^+ + W_{12}O_{40}^{8-} = 9WO_3\downarrow + Y_2(WO_4)_3\downarrow + H_2O \quad (6)$$

The refining effect of oxide particle size is limited to doping with nanosized particles due to the high adsorption capacity [44,56]. In the present investigation, WHA-$Zr(Y)O_2$ powders were prepared by the mechanically alloying of ultrafine W-$Zr(Y)O_2$ powders with Ni and Fe powders. In the alloys, nanosized $Zr(Y)O_2$ particles with size less than 200 nm were distributed on the surface of tungsten particles. Moreover, WHA-$Zr(Y)O_2$ exhibited a highly uniform nanoparticle distribution when compared to alloys produced by other powder processing methods. This indicates that L-L doping and MA, when combined together, are highly effective at reducing the particle size in strengthened tungsten alloys.

Conventionally, ODS-WHA powders are prepared by doping WHA powders with oxide particles, which often leads to oxide particle agglomeration and growth at the grain boundaries. In current research, during liquid sintering, Ni and Fe powder particles are transformed into a liquid phase, which allows the diffusion of only a small amount of tungsten. Meanwhile, some of the $Zr(Y)O_2$ particles at the grain boundaries of W powders are drawn into liquid phase and they are retained in the γ(Fe, Ni, and W) matrix. Eventually, most of the c-$Zr(Y)O_2$ particles are distributed in W grains and only a small number of c-$Zr(Y)O_2$ particles are distributed in the γ(Fe, Ni, and W) matrix.

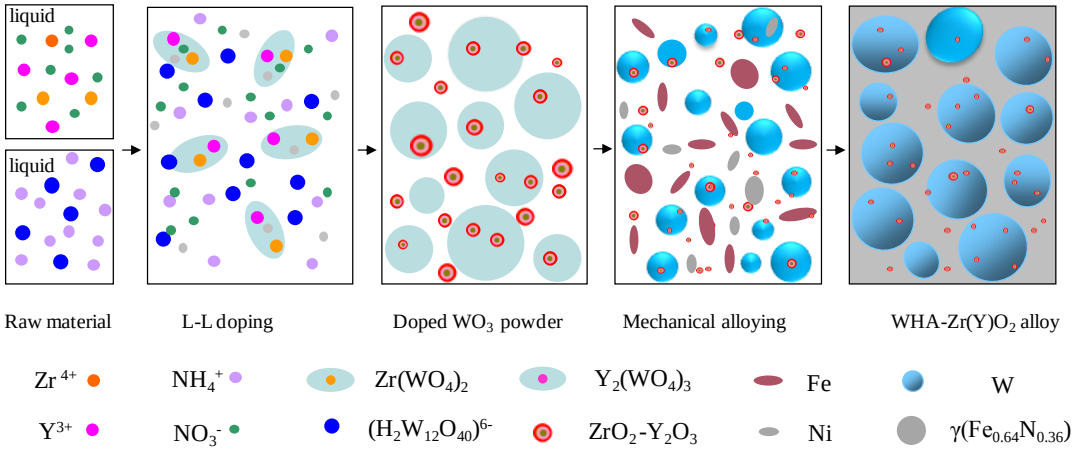

Fig. 9 Schematic of microstructural development during alloy fabrication

3.3 Mechanism of grain refinement in WHAs

Tungsten grain growth in ODS-WHAs is mainly dependent on oxide particle refinement during sintering [10,50]. However, grain refinement is complicated due to the retardation of grain growth and coarsening under different sintering conditions. Bock et al. [57] suggested that oxide particles inhibited grain growth to prevent grain coarsening. Kang et al. [58] indicated that secondary phase particles led to an increase in grain curvature. Annavarapu et al. [59] proposed that the diffusion distance of tungsten atoms increased in the presence of large secondary phase particles. Oxide particles at the tungsten-matrix (W-M) interface can block diffusion between tungsten and the matrix, which delays grain growth during WHA liquid phase sintering [52]. The doped secondary phase particles at grain boundaries affected tungsten grain size

by preventing migration along the grain boundaries and reducing the growth rate [60]. This relationship can be expressed as follows (7):

$$R = 4r/3\varphi \quad (7)$$

where R is the grain size of the tungsten phase, r is the radius of secondary phase particles, and φ is the volume fraction of the secondary phase particles.

According to Eq. (7), the grain size of tungsten particles depends on the size of oxide particles; in other words, tungsten grain size can be reduced if the size of the oxide particles located at the grain boundaries decreases.

The relationship between tungsten grain size and size of the oxide particles in ODS-WHAs observed in this study as well as in previous investigations is illustrated in Fig. 10. In general, W grain size was proportional to oxide particle size, except in the WHAs described in this study and those in Ref. [47]. These two WHAs with a large number of $Zr(Y)O_2$ particles uniformly dispersed in tungsten grains are shown in the same plot; in this case, the relationship between grain size and oxide particle size was not linear. This is because of the dispersion of $Zr(Y)O_2$ particles within tungsten grains, leading to a not obvious refinement of W grains. This observation further confirms the advantages of the L-L doping for preparing intragranular particle-strengthened tungsten alloys.

Table 4 Comparison of the microstructural parameters and sintering conditions of WHAs reported in the literature and current study

Heavy tungsten alloy	Sintering processing parameters [a]*	RD (%)	Grain size (μm)	Contiguity	Matrix volume fraction	Ref.
90W-7Ni-2Fe-1Co	1460 °C (2 h)	-	36	0.42	0.34	[62]
93W-4.9Ni-1.4Fe-0.7Co	1460 °C (2 h)	-	47	0.55	0.22	
95W-3.5Ni-1Fe-0.5Co	1460 °C (2 h)	-	59	0.73	0.16	
90W-7Ni-3Fe	1460 °C (2 h)	-	32	0.51 ± 0.2	14.3 ± 3.3	[46]
90W-6Ni-2Fe-Co	1470 °C (2 h)	-	47	0.62 ± 0.2	15.2 ± 2.1	
W-5.6Ni-1.4Fe	1485 °C (1 h)	99.9	34.5	-	-	[10]
W-Ni-Fe	1480 °C (2 h)		56	0.53 ± 0.05	0.14	[63]
W-Ni-Fe-Co		-	54	0.43 ± 0.01	0.17	
W-Ni-Fe-Re		-	49	0.48 ± 0.06	0.16	
93W-4.9Ni-2.1Fe	1520 °C (1.5h)	99.1	45.5	0.32 ± 0.04	-	[52]
95W-2.8Ni-1.2Fe-Al_2O_3		98.2	36.8	0.60 ± 0.06	-	
INERMET® IT180[b]*	-	-	100	-	-	[64]
95W-3.5Ni-1.5Cu	1510 °C (1.5 h)	98.4	60	0.60	-	[65]
96W-3Ni- 1Cu	1510 °C (1.5 h)	98.4	70	0.70	-	
90W-4xNi-xCo	1600 °C (1 h)	99.2	34	-	-	[45]
Conventional WHA[c]*	-	-	40 - 60	-	-	[9]
94W-4.56Ni-1.14Fe-Y_2O_3	1485 °C (1 h)	99	15	0.75	0.112	[53]
WHA_0	**1400 °C (2 h)**	**99.5 ± 0.1**	**41 ± 2**	**0.53 ± 0.03**	**0.37 ± 0.015**	**Current study**
$WHA_{0.75}$	**1400 °C (2 h)**	**99.3 ± 0.1**	**37 ± 2**	**0.47 ± 0.03**	**0.42 ± 0.023**	

a* Maximal sintering temperature and duration time

b* Heavy tungsten alloy reported in [64]

c* Microstructure and properties of the heavy tungsten alloy are not known.

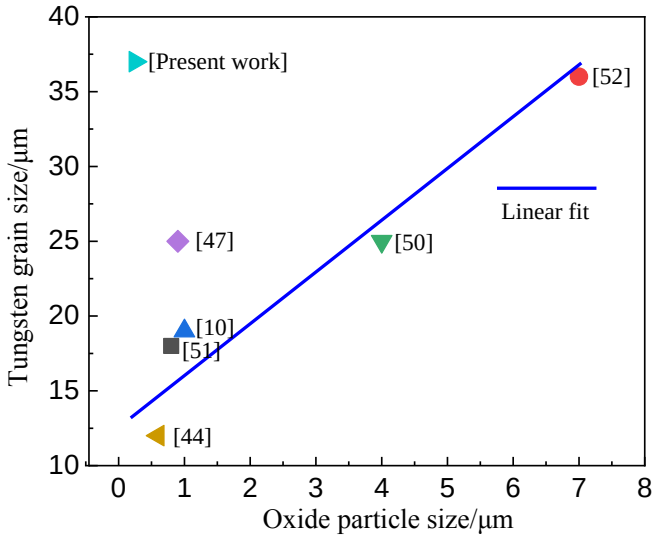

Fig. 10 Relationship between tungsten grain size and oxide particle size in ODS-WHAs reported in the current and past studies

The grain size of $Zr(Y)O_2$ particle-dispersion-strengthened WHAs described in this study was also compared with that in WHAs sintered using different methods (Table 4). The factors responsible for a fine original tungsten grain size (G_0) also contributed to grain refinement; the relationship between G_0 and refined grain size is as follows [61],

$$G^3 = G_0^3 + Kt \quad (8)$$

where G is the mean W grain size at time t, G_0 is the original average W grain size at the onset of coarsening, and K is the rate constant.

In this study, MA was conducted to produce small W particles. Internal defects caused by the significant strain on these particles due to the high impact forces generated during ball milling serve as additional nucleation sites for strain-free grains and homogenise the grain size [66]. Fan et al. [67] indicated that the powders obtained by MA affected the mechanism of sintering and contributed to fine tungsten grains in heavy alloys.

The alloys listed in Table 4 exhibited large and coarse grains as the sintering temperature increased (>1400 °C). As sintering is a diffusion-controlled process, alloys sintered at higher temperatures exhibit higher sintering and coarsening rates [68]. Moreover, high-temperature sintering results in a constant flow of the binder

phase through pores between W grains [48] and increases the final relative sintering density. The alloys described in this study exhibit a high RD comparable with the RD of alloys reported in the literature (Table 4). This is because the high pressure applied during sintering accelerates W atom diffusion [69,70]. In addition, the oxide particles also enhance the densifications process and decrease the porosity by capturing the oxygen in the matrix.

3.4 Mechanical properties of WHA-Zr(Y)O_2 alloys

Uniaxial tensile tests were conducted to measure the ultimate tensile strength (UTS) of WHA-Zr(Y)O_2 at room temperature (27 °C). The engineering stress–engineering strain curves of the fabricated WHAs in current research were shown in Fig. 11a). From Fig. 11a), as the mass fraction of Zr(Y)O_2 increases from 0 to 0.75%, the ultimate tensile strength and fracture strain of WHAs decrease linearly. The fracture strain of WHAs decreases from 0.221 to 0.039. WHA_0 possesses the highest ultimate tensile strength 937 MPa. When the mass fraction of Zr(Y)O_2 reaches to 0.25%, 0.50% and 0.75%, the ultimate tensile strengths of $WHA_{0.25}$, $WHA_{0.50}$ and $WHA_{0.75}$ were 906 MPa, 875 MPa and 782 MPa, respectively. The alloys exhibit the brittle material behaviour in tension, compared to the pure tungsten with ductile material behaviour. The comparison of the tensile mechanical properties of heavy tungsten alloys with different sintering processes is summarised in Table 5. The ultimate tensile strengths of WHA_0 and $WHA_{0.25}$ exhibit higher strengths compared to state of the art.

Fig. 11c)–f) show the fracture surfaces of the failed tensile samples of 90W-7Ni-3Fe (90WHA) [9], 90W-7Ni-3Fe-0.04Y_2O_3 (90WHA-0.04Y_2O_3) [9], WHA_0 and $WHA_{0.25}$, respectively. As shown in Fig. 11c) and d), W-W intergranular rupture is the dominant mode of fracture in 90WHA. However, a few W grain transgranular fractures and pore surfaces are still observed in 90WHA-0.04Y_2O_3. Although the strength of present WHA_0 and $WHA_{0.25}$ alloy is lower than that of the 90WHA-0.04Y_2O_3 alloy, WHA_0 and $WHA_{0.25}$ shows visual evidence of W-W cleavage patterns and the ductile failure behaviour of the matrix. This contradictory

situation would be researched in follow-up studies.

From these results, it may be inferred that oxide particles have a significant effect on the mechanical properties of the tested alloys. Too low or too high content of rare earth oxide additions would result in its different strengthening effect on tensile properties. Fan et al. [9] reported that WHAs with 0.4 wt.% oxide particles exhibited a tensile strength of 1124 MPa. In contrast, the additions of 0.1 wt.%, 0.8 wt.%Y_2O_3 into alloy decreased the maximal strength value of the alloy compared to WHA without Y_2O_3 (923 MPa). Lee et al. fabricated PSZ (0–0.3wt.%) dispersion-strengthened WHAs [51]; the ultimate tensile strengths of these alloys decreased with the addition of PSZ particles (as indicated by the red symbols in Fig. 11b)). A similar phenomenon occurred with the addition of 1% Al_2O_3 and 0.1% Y_2O_3 [10,52]. In these two alloys, the additions of oxide particles both decrease the strength values of WHAs. This indicates that a non-optimal oxide content deteriorates the tensile properties of alloys.

In addition to the oxide content, the mechanical properties of alloys depend on oxide particle distribution. In case oxide particles are agglomerated, fracture initiation might occur from these areas during tensile tests. Cracks are generated at these spots and later propagate, leading to fracture [78,79]. Moreover, rare earth oxide aggregates in the matrix or at the W-M interface restrain matrix deformation, which decreases the strength and elongation of WHAs.

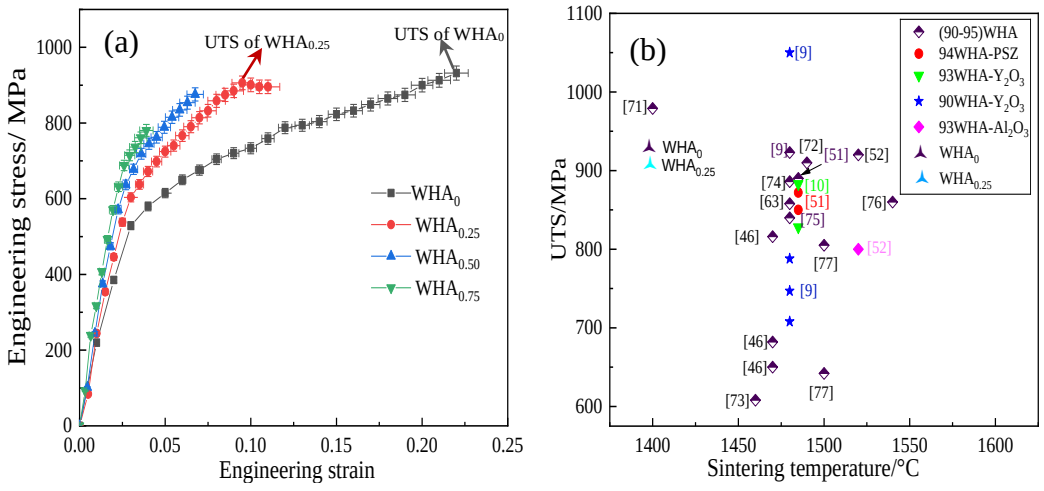

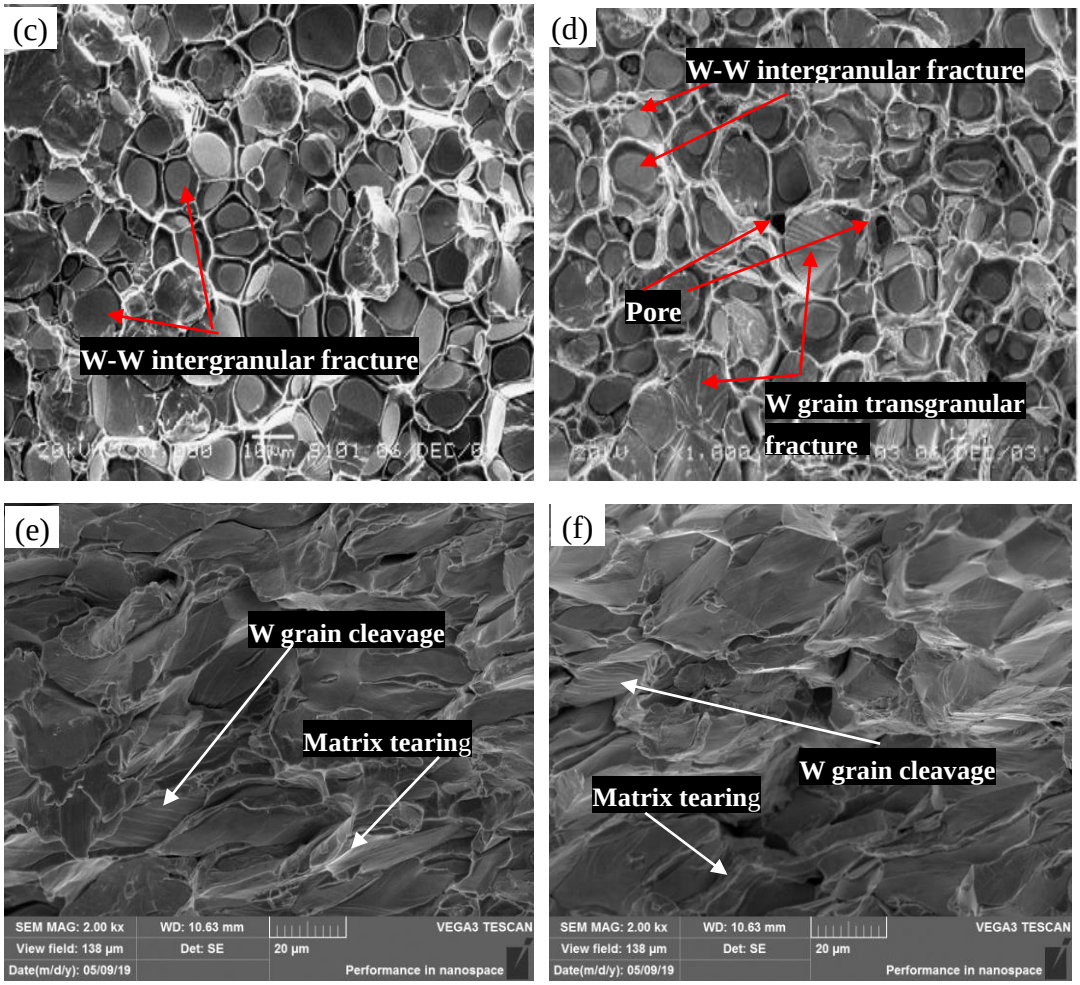

Fig. 11 Tensile properties and fracture surfaces of WHAs and ODS-WHAs described in the present work and literature. a) engineering stress–engineering strain curve of the fabricated WHAs in current research, b) ultimate tensile strengths of WHAs and ODS-WHAs vs. their sintering temperature, c) fracture surfaces of 90WHA [9], d) 90WHA-0.04Y_2O_3 [9], e) WHA_0 and f)$WHA_{0.25}$.

Table 5 An extensive literature review of the tensile mechanical properties of heavy tungsten alloys coupled with various sintering processes.

Alloys	Sintering process	UTS (MPa)	Elongation (%)	Ref.
92W-5.6Ni-2.4Fe	1400 °C (-)	975	12	[71]
90.5W–7.1Ni–1.65Fe–0.5Co–0.25Mo	1460 °C (1.5 h)	608	2.0	[73]
90W–7Ni–3Fe	1460 °C (2 h)	650	5	[46]
90W–6Ni–2Fe–2Co [a*]	1470 °C (2 h)	682	4	[46]
90W–6Ni–2Fe–2Co [b*]		816	0.7	
90W–7Ni–3Fe	1480 °C (0.5 h)	923	8.0	[9]

90W–7Ni–3Fe-0.02Y_2O_3		747	5.8	
90W–7Ni–3Fe-0.04Y_2O_3		1050	30.8	
90W–7Ni–3Fe-0.06Y_2O_3		788	2.6	
90W–7Ni–3Fe-0.08Y_2O_3		708	2.4	
93W–4.9Ni– 2.1Fe	1480 °C (2 h)	858	17	[63]
93W–4.9Ni–2.1Fe	1525 °C (1.5 h)	920	4.8	[52]
95W–2.8Ni–1.2Fe–1Al_2O_3		805	2.6	
92.5W–6.4Ni–1.1Fe [c*]	1500 °C (0.33 h)	642	-	[77]
92.5W–6.4Ni–1.1Fe [d*]		805	-	
92.6W–4.98Ni–2.4Co	1540 °C (-)	860	8	[76]
90W–6Ni–2Fe–0.5Co–1.5Mo	1480 °C (2 h)	886	24	[74]
93W–4.9Ni–2.1Fe	1490 °C (2 h)	910	20	[72]
90W–5Ni–5Fe	1480 °C (0.5 h)	840	-	[75]
93W–5.6Ni–1.4Fe-0.1Y_2O_3	1485 °C (1 h)	828	14.6	[10]
93W–5.6Ni–1.4Fe-0.1Y_2O_3	1485 °C (2 h)	883	18.4	
94W–5.9(Ni,Fe)-0.1PSZ	1485 °C (1 h)	890	-	[51]
94W–5.8(Ni,Fe)-0.2PSZ		872	-	
94W–5.7(Ni,Fe)-0.3PSZ		850	-	
WHA_0	**1400 °C (2 h)**	**937**	22.1	**Current study**
$WHA_{0.25}$		**906**	9.5	
$WHA_{0.5}$		**875**	6.7	
$WHA_{0.70}$		**782**	3.9	

a* The heating rate is 3 °C/min;

b* The heating rate is 20 °C/min;

c* Alloy was fabricated by conventional sintering;

d* Alloy was fabricated by microwave sintering.

The compressive properties of WHAs reinforced with different amounts of Zr(Y)O_2 particles were investigated and compared as shown in Fig. 12. The engineering stress-strain curves and the corresponding true stress-strain curves of WHA-Zr(Y)O_2 were plotted at room temperature (27 °C) (Fig. 12a) and b), respectively). During compressive testing, elastic deformation occurs initially with a linear relationship between stress and strain, followed by plastic deformation in the alloy. Beyond an engineering strain of 0.813, stress increased while the strain remained constant, as shown in Fig. 12a). This indicates the high plasticity of WHAs.

The matrix phase of WHAs is softer than the tungsten phase, which determines the plastic deformation capacity of the alloys during quasi-static compression. In the alloys described in the present study, the matrix phase containing a solid Zr(Y)O_2

phase exhibited good plasticity. This is due to the fact that some nanosized $Zr(Y)O_2$ particles were uniformly distributed in the matrix with a good interface. These ultrafine oxide particles reduced stress and strain concentration during compressive deformation [80].

Based on the true stress-strain curves in Fig. 12b), the WHA containing 0.5% $Zr(Y)O_2$ exhibited the best strengthening behaviour among all the tested alloys. The ultimate compressive strength of $WHA_{0.50}$ was 1445 MPa, which was higher than that of the other three alloys. Furthermore, we observed that the ultimate compressive strength obtained during plastic deformation is affected by the strain rate; to illustrate this phenomenon, we tested the alloy samples at strain rates of 10^{-3}, 10^{-2}, 10^{-1}, and 1 s^{-1}, as shown in Fig. 13.

Fig. 13a) indicates that WHA-$Zr(Y)O_2$ exhibited excellent plasticity at different strain rates. The ultimate stress increased with an increase in the strain rate, as shown in Fig. 13b). An ultimate stress of 1445 MPa was achieved at 10^{-3} s^{-1}. The compressive strength of $WHA_{0.50}$ was higher than that of several previously reported alloys, as shown in Fig. 13c). The comparison of the compressive strength value of heavy tungsten alloys with different sintering processes is summarised in Table 6. The ultimate compressive strength of $WHA_{0.50}$ was 1445 MPa, which exhibits higher strength compared to state of the art. This higher value of strength may be due to the proper amount of $Zr(Y)O_2$ particles and higher dispersed nanoparticles distribution. When the strain rate increases to 1 s^{-1}, the peak stress increases to 1560 MPa. On the one hand, a high strain rate enhances dislocation density and work hardening. On the other hand, the change of phase' deformation behaviors may be another main reason. The deformed microstructures produced at different strain rates are shown to illustrate the plastic deformation behaviour of WHA-$Zr(Y)O_2$ (Fig. 14a)–d)).

During compression, the matrix phase is the first to deform. When tests are conducted at low strain rates, the matrix phase has sufficient time to deform and flow between tungsten particles, as confirmed by the slightly elongated microstructure of tungsten grains in Fig. 14a). With the further increasing of plastic deformation, the matrix phase causes work hardening by plastic deformation, which induces a

simultaneous deformation in some tungsten particles. The deformation resistance of the matrix phase depends on the oxide particles used to reinforce it. When the strain rate during compression increases, there is not enough time for the matrix phase to flow between W particles, owing to which it gradually transmits stress to W grains, leading to their deformation. Beyond a critical strain rate, the deformation resistance of the alloy mainly depends on the tungsten phase. Therefore, W particles were seriously elongated at 1 s^{-1}, as shown in Fig. 14d).

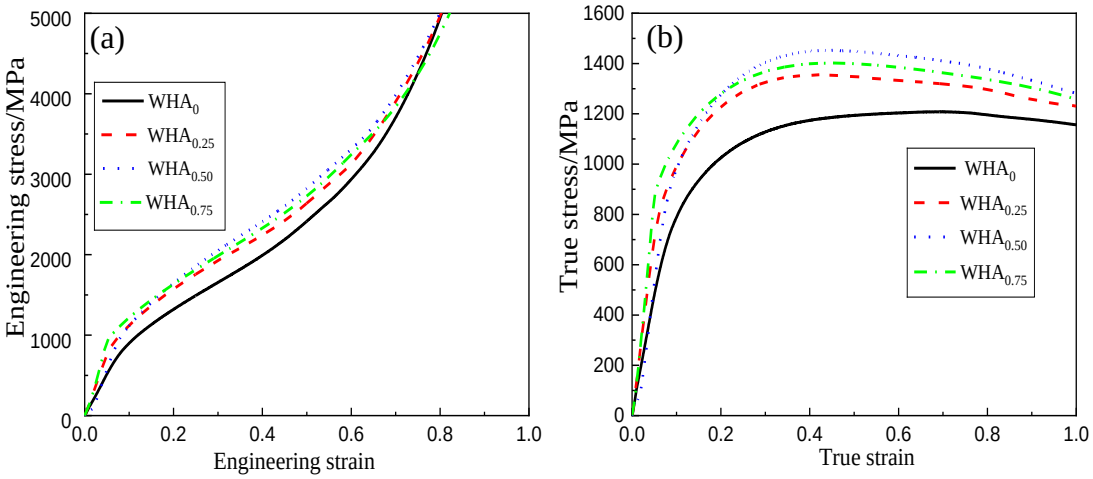

Fig. 12 a) Room temperature (27 °C) engineering stress-strain curves and b) true stress-strain curves of WHAs with different mass fractions of $Zr(Y)O_2$. Compression tests were conducted at a constant strain rate of 10^{-3} s^{-1}.

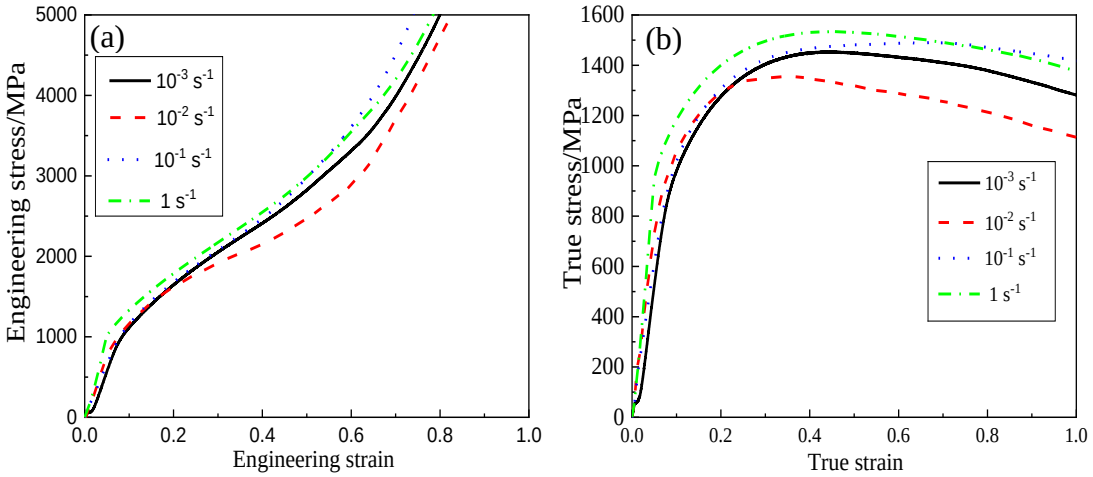

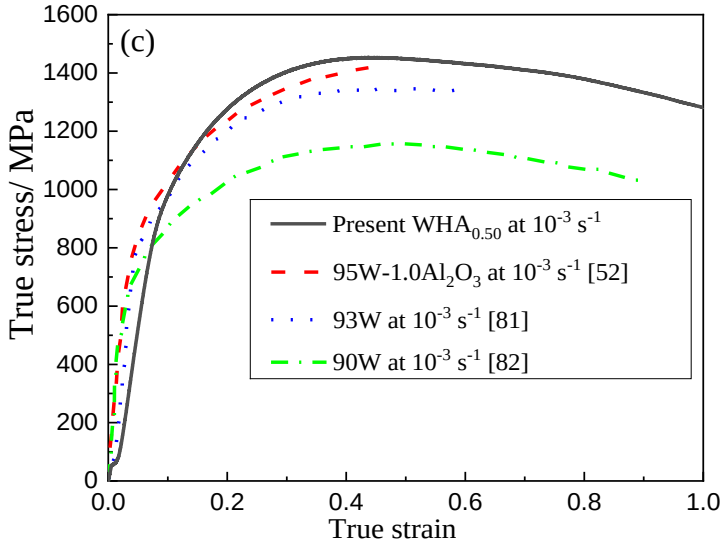

Fig. 13 a) Room temperature (27 °C) engineering stress-strain curves and b) true stress-strain curves of $WHA_{0.50}$ generated during compression tests at different strain rates. c) Comparison of the compressive true stress-strain curve of $WHA_{0.50}$ with those of previously reported alloys

Table 6 An extensive literature review of the compressive strength value of heavy tungsten alloys coupled with various sintering processes.

Alloys	**Sintering process**	**Compressive strength (MPa)**	**Ref.**
95W–2.8Ni–1.2Fe–1Al_2O_3	1525 °C (1.5 h)	1400	[52]
93W-5.6 Ni-1.4 Fe	1410 °C (-)	1380	[81]
90 W-7Ni-3Fe	1490 °C (1 h)	1150	[82]
$WHA_{0.5}$	**1400 °C (2 h)**	**1445**	**Current research**

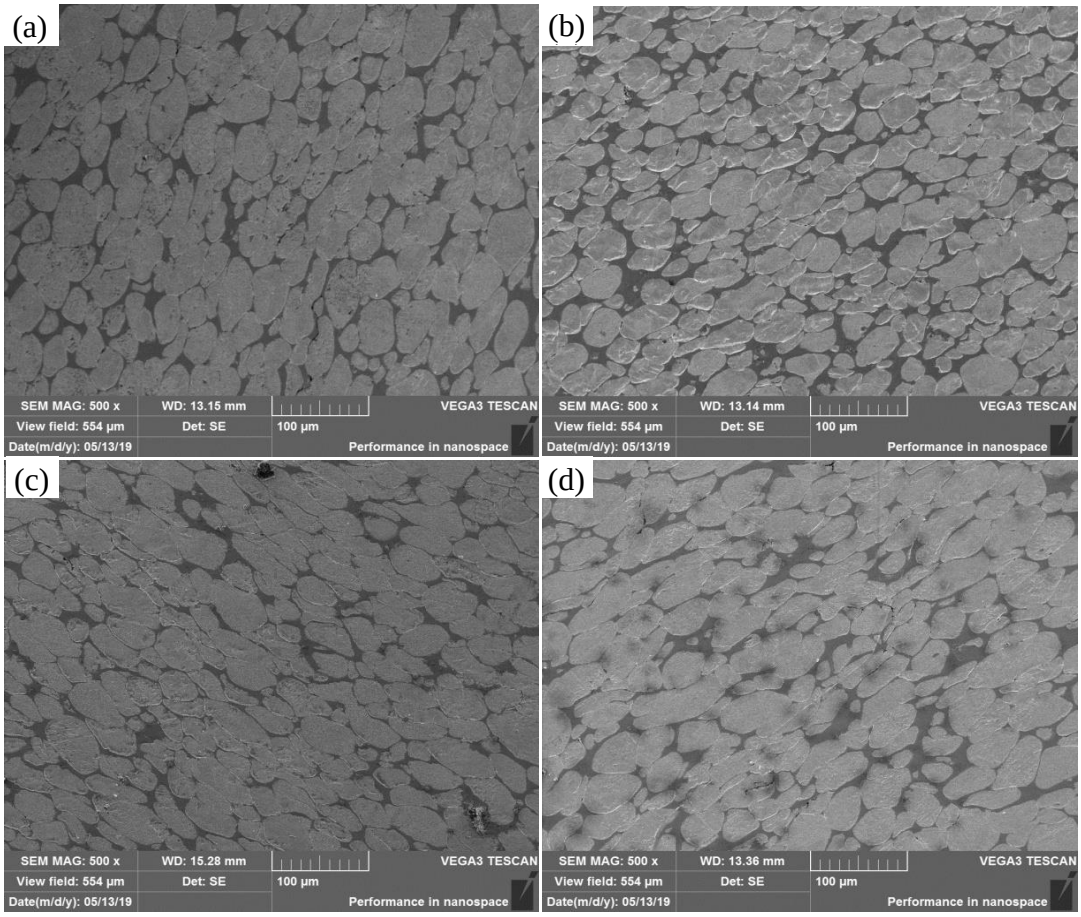

Fig. 14 Microstructure of $WHA_{0.75}$ after compression tests at room temperature (27 °C) at strain rates of a) 10^{-3}, b) 10^{-2}, c) 10^{-1}, and d) 1 s^{-1}

4. Conclusion

(1) WHAs strengthened by highly uniform nanosized $Zr(Y)O_2$ particles were fabricated by hydrothermal processing followed by MA and hot isostatic pressing.

(2) $Zr(Y)O_2$ particles bonded well with the tungsten phase; they were smaller than 200 nm in size and were distributed uniformly in tungsten grains and the matrix. TEM analysis indicated the presence of a large number of nanosized oxide particles smaller than 50 nm in the alloy microstructure.

(3) The size of $Zr(Y)O_2$ particles synthesised using combined hydrothermal and MA methods is much smaller than that in alloys previously reported; this small size also helped in tungsten grain refinement.

(4) The ultimate tensile and maximal compressive strengths of the fabricated alloys under quasi-static deformation at room temperature (27 °C) were 906 and 1445 MPa, respectively, which are much higher than the values reported in literature. The ultimate tensile strength and fracture strain of WHAs decrease with the mass fraction of $Zr(Y)O_2$ (from 0 to 0.75%). The alloys exhibit the brittle material behaviour in tension, compared to the pure tungsten with ductile material behaviour. The effect of $Zr(Y)O_2$ particles and strain rate on the compressive properties of the alloys were investigated in detail and the corresponding compressive deformation mechanisms were discussed.

Declaration of interest

There are no conflicts to declare.

Acknowledgments

National Natural Science Foundation of China [No. U2004180, No. 51874185] and Graduate Research and Innovation & Practice Projects in Jiangsu Province, China [No. KYCX19_0182]. The EIPHI Graduate School (contract ANR-17-EURE-0002), also has supported this work.

References

[1] R. Cury, F. Issartel, J. M. Joubert, H. Couque, Evolution of cobalt-free tungsten heavy alloys for kinetic energy penetrators, Powder Metall. 56 (2013) 347-350. https://doi.org/10.1179/0032589913Z.000000000137.

[2] D. W. Guo, T. K. Chi, A corrosion study on W-Cu alloys in sodium chloride solution at different pH, J. Mater. Process. Technol. (2020) In Press. https://doi.org/10.1016/j.jmst.2020.03.031.

[3] Y. Yu, H. Hu, W. Zhang, X. Xu, Microstructure evolution and recrystallization after annealing of tungsten heavy alloy subjected to severe plastic deformation, J.

Alloys Compd. 685 (2016) 971-977. https://doi.org/10.1016/j.jallcom.2016.07.004.

[4] Z. C. Cordero, R. R. Carpenter, C. A. Schuh, B. E. Schuster, Sub-scale ballistic testing of an ultrafine grained tungsten alloy into concrete targets, Int. J. Impact Eng. 91 (2016) 1-5. https://doi.org/10.1016/j.ijimpeng.2015.11.013.

[5] X. F. Liu, Z. L. Tian, X. F. Zhang, H. H. Chen, T. W. Liu, Y. Chen, Y. J. Wang, L. H. Dai, “Self-sharpening” tungsten high-entropy alloy, Acta Mater. 86 (2020) 257-266. https://doi.org/10.1016/j.actamat.2020.01.005.

[6] A. Kumari, M. Sankaranarayana, T. K. Nandy, On structure property correlation in high strength tungsten heavy alloys, Int. J. Refract. Met. Hard Mater. 67 (2017) 18-31. https://doi.org/10.1016/j.ijrmhm.2017.05.002.

[7] G. Prabhu, N. A. Kumar, M. Sankaranarayana, T. K. Nandy, Tensile and impact properties of microwave sintered tungsten heavy alloys, Mater. Sci. Eng. A. 607 (2014) 63-70. https://doi.org/10.1016/j.msea.2014.03.130.

[8] O. Dincer, M. K. Pehlivanoglu, N. K. Caliskan, I. Karakaya, A. Kalkanli, Processing and microstructural characterization of liquid phase sintered tungsten-nickel-cobalt heavy alloys, Int. J. Refract. Met. Hard Mater. 50 (2015) 106-112. https://doi.org/10.1016/j.ijrmhm.2014.12.009.

[9] J. L. Fan, L. Tao, H. C. Cao, D. L. Wang, Preparation of fine grain tungsten heavy alloy with high properties by mechanical alloying and yttrium oxide addition, J. Mater. Process. Tech. 208 (2008) 463-469. https://doi.org/10.1016/j.jmatprotec.2008.01.010.

[10] H. J. Ryu, S. H. Hong, Fabrication and properties of mechanically alloyed oxide-dispersed tungsten heavy alloys, Mater. Sci. Eng. A. 363 (2003) 179-184. https://doi.org/10.1016/S0921-5093(03)00641-5.

[11] Y. Yu, C. Ren, W. Zhang, Compressive behavior of liquid phase sintered 90 W-7Ni-3Fe heavy alloy at high temperature and low strain rate condition. Int. J. Refract. Met. Hard Mater. 76 (2018) 149-157. https://doi.org/10.1016/j.ijrmhm.2018.06.006.

[12] A. Xu, D. E. Armstrong, C. Beck, M. P. Moody, G. D. Smith, P. A. Bagot, S. G. Roberts, Ion-irradiation induced clustering in W-Re-Ta, W-Re and W-Ta alloys: An atom probe tomography and nanoindentation study, Acta Mater. 124 (2017) 71-78. https://doi.org/10.1016/j.actamat.2016.10.050.

[13] S. Park, D. K. Kim, S. Lee, R. Hojin, H. S. Hyung, Dynamic deformation behavior of an oxide-dispersed tungsten heavy alloy fabricated by mechanical alloying, Metall. Mater. Trans. A. 32 (2001) 2011-2020. https://doi.org/10.1007/s11661-001-0013-1.

[14] J. W. Li, F. Fang, Z. Wang, G. S. Zhang, S. Z. Wei, L. J. Xu, K. M. Pan, Microstructure and properties characterization of W-25Cu composite materials liquid-liquid doped with La_2O_3, Int. J. Refract. Met. Hard Mater. 71 (2018) 115-121. https://doi.org/10.1016/j.ijrmhm.2017.10.019.

[15] W. Hu, Z. Dong, L. Yu, Z. Ma, Y. Liu, Synthesis of W-Y_2O_3 alloys by freeze-drying and subsequent low temperature sintering: microstructure refinement and second phase particles regulation, J. Mater. Process. Technol. 36 (2020) 84-90. https://doi.org/10.1016/j.jmst.2019.08.010.

[16] Z. Dong, N. Liu, W. Hu, Z. Ma, C. Li, C. Liu, Q. Y. G, Y. Liu, Controlled synthesis of high-quality W-Y_2O_3 composite powder precursor by ascertaining the synthesis mechanism behind the wet chemical method, J. Mater. Process. Technol. 36 (2020) 118-127. https://doi.org/10.1016/j.jmst.2019.05.067.

[17] L. Ding, D. P. Xiang, Y. Y. Li, Y. W. Zhao, J. B. Li, Phase, microstructure and properties evolution of fine-grained W-Mo-Ni-Fe alloy during spark plasma sintering, Mater. Des. 37 (2012) 8-12. https://doi.org/10.1016/j.matdes.2011.12.010.

[18] Y. Y. Li, K. Hu, X. Q. Li, X. Ai, S. G. Qu, Fine-grained 93W-5.6Ni-1.4Fe heavy alloys with enhanced performance prepared by spark plasma sintering, Mater. Sci. Eng. A. 573 (2013) 245-252. https://doi.org/10.1016/j.msea.2013.02.069.

[19] G. Prabhu, N. A. Kumar, M. Sankaranarayana, T. K. Nandy, Tensile and impact properties of microwave sintered tungsten heavy alloys, Mater. Sci. Eng. A. 607 (2014) 63-70. https://doi.org/10.1016/j.msea.2014.03.130.

[20] T. Sadat, G. Dirras, D. Tingaud, M. Ota, T. Chauveau, D. Faurie, S. Vajpai, K. Ameyama, Bulk Ni–W alloys with a composite-like microstructure processed by spark plasma sintering: Microstructure and mechanical properties, Mater. Des. 89 (2016) 1181-1190. https://doi.org/10.1016/j.matdes.2015.10.083.

[21] L. Xu, Q. Yan, M. Xia, L. Zhu, Preparation of La_2O_3 doped ultra-fine W powders by hydrothermal-hydrogen reduction process, Int. J. Refract. Met. Hard Mater. 36 (2013) 238-242. https://doi.org/10.1016/j.ijrmhm.2012.09.005.

[22] Z. Dong, N. Liu, Z. Q. Ma, C. X. Liu, Q. Y. Guo, Y. Yusuke, H. R. Alamri, Z. A. Alothman, M. S. Hossain, Y. C. Liu, Synthesis of nanosized composite powders via a wet chemical process for sintering high performance W-Y_2O_3 alloy, Int. J. Refract. Met. Hard Mater. 69 (2017) 266-272. https://doi.org/10.1016/j.ijrmhm.2017.09.001.

[23] F. N. Xiao, Q. Miao, S. Z. Wei, K. Pan, J. W. Li, W. Liu, L. J. Xu, Hydrothermal synthesis of nanoplates assembled hierarchical h-WO_3 microspheres and phase evolution in preparing cubic Zr(Y)O_2-doped tungsten powders, Adv. Powder Technol. 29 (2018) 2633-2643. https://doi.org/10.1016/j.apt.2018.07.011.

[24] H. Zhang, W. Deng, Z. M. Xie, R. Liu, J. F. Yang, C. S. Liu, X. P. Wang, Q. F. Fan, Y. Xiong, Recent progresses on designing and manufacturing of bulk refractory alloys with high performances based on controlling interfaces, J. Mater. Process. Technol. (2020) In Press. https://doi.org/10.1016/j.jmst.2020.02.046.

[25] G. Liu, G. J. Zhang, F. Jiang, X. D. Ding, Y. J. Sun, J. Sun, E. Ma, Nanostructured high-strength molybdenum alloys with unprecedented tensile ductility, Nat. Mater. 12 (2013) 344-50. https://doi.org/10.1038/NMAT3544.

[26] J. L. Fan, X. Gong, B. Y. Huang, M. Song, T. Liu, M. G. Qi, J. M. Tian, S. K. Li, Dynamic failure and adiabatic shearbands in fine-grain 93W-4.9Ni-2.1Fe alloy with Y_2O_3 addition under lower high-strain-rate (HSR) compression, Mech. Mater. 42 (2010) 24-30. https://doi.org/10.1016/j.mechmat.2009.08.006.

[27] F. N. Xiao, T. Barriere, G. Cheng, S. Z. Wei, S. W. Zuo, L. J. Xu, Research on preparation process for the in situ nanosized Zr(Y)O_2 particles dispersion-strengthened tungsten alloy through synthesizing doped hexagonal

$(NH_4)_{0.33}·WO_3$. J. Alloys Compd. 843 (2020) 156059. https://doi.org/10.1016/j.jallcom.2020.156059.

[28] U. R. Kiran, A. Panchal, M. Sankaranarayana, G. V. S. Nageswara, T. K. Nandy, Effect of alloying addition and microstructural parameters on mechanical properties of 93% tungsten heavy alloys, Mater. Sci. Eng. A. 640 (2015) 82-90. https://doi.org/10.1016/j.msea.2015.05.046.

[29] S. Cao, H. Chen, Nanorods assembled hierarchical urchin-like WO_3 nanostructures: Hydrothermal synthesis, characterization, and their gas sensing properties, J. Alloys Compd. 702 (2017) 644-648. https://doi.org/10.1016/j.jallcom.2017.01.232.

[30] L. Z. Li, J. Z. Zhao, Y. Wang, Y. L. Li, D. C. Ma, Y. Zhao, S. N. Hou, X. L. Hao, Oxalic acid mediated synthesis of WO_3-H_2O nanoplates and self-assembled nanoflowers under mild conditions, J. Solid. State. Chem. 184 (2011) 1661-1665. https://doi.org/10.1016/j.jssc.2011.05.008.

[31] M. Q. Xu, W. Zeng, F. Yang, L. Chen, Controllability of assemblage from WO_3-H_2O nanoplates to nanoflowers with the assistance of oxalic acid, J. Mater. Sci-Mater. El. 26 (2015) 6676-6682. https://doi.org/10.1016/j.jssc.2011.05.008.

[32] B. Miao, W. Zen, S. H. Hussain, Q. P. Mei, S. B. Xu, H. Zhang, Y. Q. Li, T. M. Li, Large scale hydrothermal synthesis of monodisperse hexagonal WO_3 Nanowire and the growth mechanism, Mater. Lett. 147 (2015) 12-15. https://doi.org/10.1016/j.matlet.2015.02.020.

[33] L. Zhang, X. C. Tang, Z. G. Lu, Z. M. Wang, Facile synthesis and photocatalytic activity of hierarchical WO3 core-shell microspheres, Appl. Surf. Sci. 258 (2011) 1719-1724. https://doi.org/10.1016/j.apsusc.2011.10.022.

[34] J. H. Ha, P. Muralidharan, D. K. Kim, Hydrothermal synthesis and characterization of self-assembled h-WO_3 nanowires/nanorods using EDTA salts, J. Alloys Compd. 475 (2009) 446-451. https://doi.org/10.1016/j.jallcom.2008.07.048.

[35] C. Wang, L. Zhang, S. Wei, K. M. Pan, M. Aindow, Y. P. Yang, Microstructure and preparation of an ultra-fine-grained W-Al_2O_3 composite via hydrothermal

synthesis and spark plasma sintering, Int. J. Refract. Met. Hard Mater. 72 (2018) 149-156. https://doi.org/10.1016/j.ijrmhm.2017.12.022.

[36] C. J. Wang, L. Q. Zhang, S. Z. Wei, K. M. Pan, X. C. Wu, Q. K. Li, Effect of ZrO_2 content on microstructure and mechanical properties of W alloys fabricated by spark plasma sintering, Int. J. Refract. Met. Hard Mater. 79 (2019) 79-89. https://doi.org/10.1016/j.ijrmhm.2018.11.006.

[37] Z. Li, L. J. Xu, S. Z. Wei, C. Chen, F. N. Xiao, Fabrication and mechanical properties of tungsten alloys reinforced with c-ZrO_2 particles, J. Alloys Compd. 769 (2018) 694-705. https://doi.org/10.1016/j.ijrmhm.2018.11.006.

[38] Y. Shen, Z. Xu, K. Cui, J. Yu, Microstructure of a commercial W-1% La_2O_3 alloy, J. Nucl. Mater. 455 (2014) 234-241. https://doi.org/10.1016/j.jnucmat.2014.06.004.

[39] M. A. Yar, S. Wahlberg, H. Bergqvist, H. G. Salem, M. Johnsson, M. Muhammed, Chemically produced nanostructured ODS-lanthanum oxide-tungsten composites sintered by spark plasma, J. Nucl. Mater. 408 (2011) 129-135. https://doi.org/10.1016/j.jnucmat.2010.10.060.

[40] M. A. Yar, S. Wahlberg, H. Bergqvist, H. G. Salem, M. Johnsson, M. Muhammed, Spark plasma sintering of tungsten-yttrium oxide composites from chemically synthesised nanopowders and microstructural characterization, J. Nucl. Mater. 412 (2011) 227-232. https://doi.org/10.1016/j.jnucmat.2011.03.007.

[41] A. Muñoz, M. A. Monge, B. Savoini, M. E. Rabanal, G. Garces, R. Pareja, La_2O_3-reinforced W and W-V alloys produced by hot isostatic pressing, J. Nucl. Mater. 417 (2011) 508-511. https://doi.org/10.1016/j.jnucmat.2011.01.077.

[42] R. Liu, Z. M. Xie, T. Zhang, Q. F. Fang, X. P. Wang, T. Hao, C. S . Liu, Y. Dai, Mechanical properties and microstructures of W-1%Y_2O_3 microalloyed with Zr, Mater. Sci. Eng. A. 660 (2016) 19-23. https://doi.org/10.1016/j.msea.2016.02.072.

[43] Y. M. Ki, K. H. Lee, E. P. Kim, D. I. Cheong, S. H. Hong, Fabrication of high temperature oxides dispersion strengthened tungsten composites by spark plasma

sintering process, Int. J. Refract. Met. Hard Mater. 27 (2009) 842-846. https://doi.org/10.1016/j.ijrmhm.2009.03.003.

[44] C. L. Chen, Sutrisna, The Effect of Mo and Dispersoids on Microstructure, Sintering Behavior, and Mechanical Properties of W-Mo-Ni-Fe-Co Heavy Tungsten Alloys, Metals. 9 (2019) 111. https://doi.org/10.3390/met9020111.

[45] O. Dinçer, M. K. Pehlivanoğlu, N. K. Çalişkan, I. Karakaya, A. Kalkanli, Processing and microstructural characterization of liquid phase sintered tungsten-nickel-cobalt heavy alloys, Int. J. Refract. Met. Hard Mater. 50 (2015) 106-112. https://doi.org/10.1016/j.ijrmhm.2014.12.009.

[46] G. Prabhu, N. A. Kumar, M. Sankaranarayana, T. K. Nandy, Tensile and impact properties of microwave sintered tungsten heavy alloys, Mater. Sci. Eng. A. 60 (2014) 63-70. https://doi.org/10.1016/j.msea.2014.03.130.

[47] L. J. Xu, F. N. Xiao, S. Z. Wei, Y. C. Zhou, K. M. Pan, X. Q. Li, W. Liu, Development of tungsten heavy alloy reinforced by cubic zirconia through liquid-liquid doping and mechanical alloying methods, Int. J. Refract. Met. Hard Mater. 78 (2019) 1-8. https://doi.org/10.1016/j.ijrmhm.2018.08.009.

[48] Z. S. Fan, D. P. Xiang, Y. L. Pan, H. Jiang, Effect of two-time spark plasma sintering on microstructure and mechanical properties of W-6Ni-4Mn alloy, Mater. Sci. Eng. A. 745 (2019) 300-306. https://doi.org/10.1016/j.msea.2018.12.109.

[49] G. Liu, G. J. Zhang, F. Jiang, X. D. Ding, Y. J. Sun, J. Sun, E. Ma, Nanostructured high-strength molybdenum alloys with unprecedented tensile ductility, Nat. Mater. 12 (2013) 344-50. https://doi.org/10.1038/NMAT3544.

[50] W. M. R. Daoush, A. H. A. Elsayed, O. A. G. E. Kady, O. A. G. Sayed, M. A. Dawood, Enhancement of physical and mechanical properties of oxide dispersion-strengthened tungsten heavy alloys, Mater. Sci. Eng. A. 47 (2016) 2387-2395. https://doi.org/10.1007/s11661-016-3360-7.

[51] K. H. Lee, S. I. Cha, H. J. Ryu, M. F. Dilmore, S. H. Hong, Effect of mechanical alloying process on microstructure and mechanical properties of ODS tungsten heavy alloys, J. Alloys Compd. 434 (2007) 433-436. https://doi.org/10.1016/j.jallcom.2006.08.284.

[52] K. Hu, X. Li, X. Ai, S. Qu, Y. Li, Fabrication, characterization, and mechanical properties of 93W-4.9Ni-2.1Fe/95W-2.8Ni-1.2Fe-1Al_2O_3 heavy alloy composites, Mater. Sci. Eng. A. 636 (2015) 452-458. https://doi.org/10.1016/j.msea.2015.04.026.

[53] K. H. Lee, S. I. Cha, H. J. Ryu, S. H. Hong, Effect of two-stage sintering process on microstructure and mechanical properties of ODS tungsten heavy alloy, Mater. Sci. Eng. A, 458 (2007) 323–329.

[54] F. N. Xiao, L. J. Xu, Y. C. Zhou, K. M. Pan, J. W. Li, W. Liu, S. Z. Wei, A hybrid microstructure design strategy achieving W-ZrO_2(Y) alloy with high compressive strength and critical failure strain, J. Alloys Compd. 708 (2017) 202-212. https://doi.org/10.1016/j.jallcom.2017.02.277.

[55] Z. M. Xie, R. Liu, T. Zhang, Q. F. Fang, C. S. Liu, X. Liu, G. N. Luo, Achieving high strength/ductility in bulk W-Zr-Y_2O_3 alloy plate with hybrid microstructure, Mater. Des. 107 (2016) 144-52. https://doi.org/10.1016/j.matdes.2016.06.012.

[56] F. N. Xiao, Q. Miao, S. Z. Wei, T. Barriere, G. Cheng, S. W. Zuo, L. J. Xu, Uniform nanosized oxide particles dispersion strengthened tungsten alloy fabricated involving hydrothermal method and hot isostatic pressing, J. Alloys Compd. 824 (2020) 153894. https://doi.org/10.1016/j.jallcom.2020.153894.

[57] A. Bock, W. D. Schbert, B. Lux, Inhibition of grain growth on submicron cemented carbides, Int. Powder Metal. 24 (1992) 20. EDB-92-078461.

[58] S. J. L. Kang, W. A. Kaysser, G. Petzow, D. N. Yoon, Elimination of pores during liquid phase sintering of Mo-Ni, Int. Powder Metal. 27 (1984) 97-100. https://doi.org/10.1179/pom.1984.27.2.97.

[59] S. Annavarapu, R. D. Doherty, Inhibited coarsening of solid-liquid microstructures in spray casting at high volume fractions of solid, Acta. Metall. Sin. 43 (1995) 3207-3230. https://doi.org/10.1016/0956-7151(94)00448-Q.

[60] Z. Li, L. J. Xu, S. Z. Wei, C. Chen, F. N. Xiao, Fabrication and mechanical properties of tungsten alloys reinforced with c-ZrO_2 particles, J. Alloys Compd. 769 (2018) 694-705. https://doi.org/10.1016/j.jallcom.2018.07.342.

[61] H. Zhang, L. Ge, M. Shi, P. Ren, Densification behavior, mechanical properties and thermal shock resistance of tungsten alloys fabricated at low temperature, Mater. Des. 58 (2014) 290-297. https://doi.org/10.1016/j.matdes.2014.01.023.

[62] U. R. Kiran, S. Venkat, B. Rishikesh, Effect of tungsten content on microstructure and mechanical properties of swaged tungsten heavy alloys, Mater. Sci. Eng. A. 582 (2013) 389-396. https://doi.org/10.1016/j.msea.2013.06.041.

[63] U. R. Kiran, A. Panchal, M. Sankaranarayana, B. Iyer, V. K. Sankaranarayana, T. K. Nandy, Effect of alloying addition and microstructural parameters on mechanical properties of 93% tungsten heavy alloys, Mater. Sci. Eng. A. 640 (2015) 82-90. https://doi.org/10.1016/j.msea.2015.05.046.

[64] M. Scapin, Mechanical characterization and modeling of the heavy tungsten alloy IT180, Int. J. Refract. Met. Hard Mater. 50 (2015) 258-268. https://doi.org/10.1016/j.ijrmhm.2015.01.018.

[65] J. Das, G. A. Rao, S. K. Pabi, Microstructure and mechanical properties of tungsten heavy alloys, Mater. Sci. Eng. A. 527 (2010) 7841-7847. https://doi.org/10.1016/j.msea.2010.08.071.

[66] U. R. Kiran, M. P. Kumar, M. Sankaranarayana, K. Singh, T. K. Nandy, High energy milling on tungsten powders, Int. J. Refract. Met. Hard Mater. 48 (2015) 74-81. https://doi.org/10.1016/j.ijrmhm.2014.06.025.

[67] J. L. Fan, B. Y. Huang, X. Qu, Z. Q. Zou,Thermal stability, grain growth and structure changes of mechanically alloyed W-Ni-Fe composite during annealing, Int. J. Refract. Hard Mater. 19 (2001) 73-79. https://doi.org/10.1016/S0263-4368(00)00046-9.

[68] S. C. Zhou, L. Wang, Y. J. Liang, Y. C. Zhu, R. Z. Jian, B. P. Wang, L. Wang, Y. F. Xue, F. C. Wang, H. N. Cai, Y. Ren, A strategy to achieve high-strength WNiFe composite-like alloys with low W content by laser melting deposition, Mater. Des. 190 (2020) 108554. https://doi.org/10.1016/j.matdes.2020.108554.

[69] J. Kappacher, A. Leitner, D. Kiener, H. Clemens, V. M. Kiener, Thermally activated deformation mechanisms and solid solution softening in W-Re alloys

investigated via high temperature nanoindentation, Mater. Des. 189 (2020) 108499. https://doi.org/10.1016/j.matdes.2020.108499.

[70] L. Huang, L. Jiang, T. D. Topping, C. Dai, X. Wang, R. Carpenter, C. Haines, J. M. Schoenung, In situ oxide dispersion strengthened tungsten alloys with high compressive strength and high strain-to-failure, Acta Mater. 122 (2017) 19-31. https://doi.org/10.1016/j.actamat.2016.09.034.

[71] N. Senthilnathan, A. Annamalai, G. Venkatachalam, Microstructure and mechanical properties of spark plasma sintered tungsten heavy alloys, Mater. Sci. Eng. A. 710 (2018) 66-73. https://doi.org/10.1016/j.msea.2017.10.080.

[72] X. Gong, J. Fan, F. Ding, Tensile mechanical properties and fracture behavior of tungsten heavy alloys at 25-1100 C, Mater. Sci. Eng. A. 646 (2015) 315-321. https://doi.org/10.1016/j.msea.2015.08.079.

[73] J. Das, G. A. Rao, S. K. Pabi, M. Sankaranarayana, T. K. Nandy, Thermo-mechanical processing, microstructure and tensile properties of a tungsten heavy alloy, Mater. Sci. Eng. A. 613 (2014) 48-59. https://doi.org/10.1016/j.msea.2014.06.072.

[74] U. R. Kiran, J. Kumar, V. Kumar, M. Sankaranarayana, G. V. S. N. Rao, T. K. Nandy, Effect of cyclic heat treatment and swaging on mechanical properties of the tungsten heavy alloys, Mater. Sci. Eng. A. 656 (2016) 256-265. https://doi.org/10.1016/j.msea.2016.01.024.

[75] T. D. Wen, Z. S. Liang, Y. Liang, Research on the preparation and shielding properties of W-Ni-Fe alloy material by liquid phase sintering, Int. Powder Metall. 61 (2018) 28-35. https://doi.org/10.1080/00325899.2017.1376791.

[76] Y. Shao, F. Guo, Y. Huan, D. Q. Jiang, J. S. Zhang, Y. Ren, L. S. Cui, Fabrication, microstructure and mechanical properties of WNiTi composites, J. Alloys Compd. 695 (2017) 1976-1983. https://doi.org/10.1080/00325899.2017.1376791.

[77] N. Senthilnathan, A. R. Annamalai, G. Venkatachalam, Sintering of tungsten and tungsten heavy alloys of W-Ni-Fe and W-Ni-Cu: a review, T. India. I. Metals. 70 (2017) 1161-1176. https://doi.org/10.1007/s12666-016-0936-2.

[78] M. E. Alam, G. R. Odette, On the remarkable fracture toughness of 90 to 97W-NiFe alloys revealing powerful new ductile phase toughening mechanisms, Acta Mater. 186 (2020) 324-340. https://doi.org/10.1016/j.actamat.2020.01.012.

[79] C. Sun, S. Wang, W. Guo, W. Shen, C. Ge, Bonding interface of W–CuCrZr explosively welded composite plates for plasma facing components, J. Mater. Process. Technol. 12 (2014) 1230-1234. https://doi.org/10.1016/j.jmst.2014.11.014.

[80] F. Xiao, L. Xu, Y. Zhou, K. Pan, J. Li, W. Liu, S. Wei, Microstructure and mechanical properties of W-ZrO_2 alloys by different preparation techniques, J. Alloys Compd. 774 (2019) 210-221. https://doi.org/10.1016/j.jallcom.2018.09.321.

[81] K. Hu, X. Li, M. Guan, S. G. Qu, X. Y. Yang, J. X. Zhang, Dynamic deformation behavior of 93W-5.6 Ni-1.4 Fe heavy alloy prepared by spark plasma sintering, Int. J. Refract. Met. Hard Mater. 58 (2016) 117-124. https://doi.org/10.1016/j.ijrmhm.2016.04.010.

[82] Y. Yu, C. Ren, W. Zhang, Compressive behavior of liquid phase sintered 90W-7Ni-3Fe heavy alloy at high temperature and low strain rate condition, Int. J. Refract. Met. Hard Mater. 76 (2018) 149-157. https://doi.org/10.1016/j.ijrmhm.2018.06.006.